

ABSTRACT

CHIU, CHI-KAI. Polymer-Silica Nanocomposites: a Versatile Platform for Multifunctional Materials. (Under the direction of Tzy-Jiun M. Luo).

Solution sol-gel synthesis is a versatile approach to create polymer-silica nanocomposite materials. The solution-to-solid transformation results in a solid consisting of interconnected nanoporous structure in 3D space, making it the ideal material for filtration, encapsulation, optics, electronics, drug release, and biomaterials, etc. Although the pore between nano and meso size may be tunable using different reaction conditions, the intrinsic properties such as limited diffusion within pore structure, complicated interfacial interactions at the pore surfaces, shrinkage and stress-induced cracking and brittleness have limited the applications of this material. To overcome these problems, diffusion, pore size, shrinkage and stress-induced defects need further investigation. Thus, the presented thesis will address these important questions such as whether these limitations can be utilized as the novel method to create new materials and lead to new applications.

First, the behaviors of polymers such as poly(ethylene glycol) inside the silica pores are examined by studying the nucleation and growth of AgCl at the surface of the porous matrix. The pore structure and the pressure induced by the shrinkage affect have been found to induce the growth of AgCl nanocrystals. When the same process is carried out at 160 °C, silver metallization is possible. Due to the shrinkage-induced stresses, the polymer tends to move into open crack spaces and exterior surfaces, forming interconnected silver structure. This interconnected silver structure is very unique because its density is not related to the size scale of nanopore structures. These findings suggest that it is possible to utilize defect

surface of silica material as the template to create interconnected silver structure. When the scale is small, polymer may no longer be needed if the diffusion length of Ag is more than the size of silica particles. To validate our assumption, monoliths of sol-gel sample containing AgNO_3 was ground into two different sizes of powder followed by powder pressing, heat-treating and etching. A new robust porous silver foam was then successfully made. By combining the results from room temperature and high temperature processes, we further study the patterned silver nanoparticles arrays in order to examine how mobility of silver can be controlled on a quantifiable scale. Furthermore, we have identified a thiol-containing sol-gel precursor to control the affinity between silver and silica matrix. Lastly, the effects of interfacial interactions between sol-gel silica and other nanocomposite components and the effect of thickness of the sol-gel layer on mechanical properties were investigated. These studies were applied to the biomimetic hydroxyapatite-gelatin system. We have found that by limiting the thickness while maintaining interfacial interactions of the sol-gel layer, a unique moldable property and short hardening time from these nanocomposites can be achieved without compromising its biocompatibility. Their biocompatibility has been proven based on the *in vitro* and *in vivo* testing of these materials.

In conclusion, the present study has demonstrated that polymer-silica nanocomposite is a versatile platform to carry out applications in nanocrystal growth, nanoporous metals, metal-ceramic composites, nano-imprint thin film, and bone grafts. These important findings not only provide new insights into nanocomposites but also give new meanings to the previously functional-limited sol-gel materials.

Polymer-Silica Nanocomposites: a Versatile Platform for Multifunctional Materials

by
Chi-Kai Chiu

A dissertation submitted to the Graduate Faculty of
North Carolina State University
in partial fulfillment of the
requirements for the degree of
Doctor of Philosophy

Materials Science and Engineering

Raleigh, North Carolina

2012

APPROVED BY:

Tzy-Jiun M. Luo
Chair of Advisory Committee

Donald Brenner

Anatoli Melechko

Ching-Chang Ko

DEDICATION

To my parents and sister, who are the reason for everything.

BIOGRAPHY

Chi-Kai Chiu was born on January 23rd, 1979 in Kaohsiung, Taiwan. He attended National Tsing Hua University and earned his Bachelor of Science in Materials Science and Engineering department in 2001. Then, he studied optical properties of anti-reflection coating and earned his Master of Science in 2003. After graduation, he concentrated on developing metal/metal-air fuel cells for electric car applications in the company. In pursuit of higher education, he started his doctoral program in Materials Science and Engineering department at North Carolina State University in 2008. His studies focused on material synthesis, structure characterization and potential applications of polymer-silica nanocomposites.

ACKNOWLEDGMENTS

I would first like to express my sincere gratitude to my advisor Dr. Tzy-Jiun Mark Luo for his continuous support during my Ph.D. program. He taught me how to look at research problem at different angles and various ways to approach and solve the problem. He was always there to meet and discuss about my ideas, to think and clear out my confusions, to proofread and make up my papers. Without his constant guidance and encouragement, I could not have finished the degree. I am especially thankful to Dr. Ching-Chang Ko for his consistent support on developing my knowledge in biomaterials. I have learned how to summarize and analyze problem from his brainstorming style that is greatly beneficial to my researches. I am also thankful to my committee members, Dr. Donald Brenner and Dr. Anatoli Melechko, for their valuable time, constructive opinions and valuable advices. I would also like to thank Dr. Douglas Irving and Dr. Lew Reynolds for helping me enjoy the TA's life in NCSU.

I would like to thank my group members, Yong-Jae, Natalie, Errol, Zach and Han-Hui for their help, support and encouragement. I am so happy with their accompaniments and enjoyed their friendship. I also like to thank my group member in UNC-Chapel Hill, John, DJ, Joao and Li for their valuable helps and cares. Thank all of my group members and you are like my family. I am greatly thankful to Edna, Roger and Toby for all their supports in MSE department. I also thank Wallace and Amar in CHANL for their helps in instruments.

I would like to thank my friends, Bowen, Chia-Lin, Chung-Wei, Ethan, Fiona, Hsi-Chuan, Hsiao-Yi, Hui-Jie, Ivy, Jim, Mac, Mason, Monkey, Ruiwei, Samuel, Wei-Ting and Yafen for making my life colorful and joyful. Thanks for sharing your happiness and wonderfulness with me.

Finally, I would like to dedicate this thesis to my parents and my sister. You are the reason for everything.

TABLE OF CONTENTS

LIST OF TABLES.....	ix
LIST OF FIGURES.....	x
Chapter 1. Introduction.....	1
1.1 Introduction and motivation.....	2
1.2 References.....	9
Chapter 2. Formation of AgCl Cubic Crystals Induced by Shrinkage of Sol-Gel Silica Substrate.....	16
2.1 Introduction.....	17
2.2 Experimental procedures	18
2.2.1 Preparation of PEG-sol	18
2.2.2 Preparation of sol-gel thin film	19
2.2.3 SEM, TEM, and AFM observation.....	20
2.3 Results and discussion	20
2.4 Conclusion	26
2.5 References.....	26
Chapter 3. Controlling Interconnected Silver Network Structure in Sol-Gel Nanocomposite.....	33
3.1 Introduction.....	34
3.2 Experimental procedures	35
3.2.1 Nanocomposite synthesis.....	35
3.2.2 Micro-hardness, fragment size analysis, bulk resistivity and cross-section analysis.....	36
3.2.3 Determination of silver network density.....	37
3.3 Results and discussion	37
3.4 Conclusion	44
3.5 References.....	44
Chapter 4. Synthesis of Porous Silver Metals by Ceramic Processing of Sol-Gel Particles ..	50
4.1 Introduction.....	51
4.2 Experimental procedures	52
4.3 Results and discussion	53
4.4 Conclusion	58

4.5 References.....	59
Chapter 5. Self-Assembled Silver Nanoparticle Pattern Using Silane Treated Sol-gel Nanocomposites.....	66
5.1 Introduction.....	67
5.2 Materials and Methods.....	69
5.2.1 Preparation of stock solutions.....	69
5.2.2 Synthesis of patterned nanoparticle arrays	69
5.2.3 Characterization methods.....	71
5.3 Results and discussion	71
5.4 Conclusion	77
5.5 References.....	78
Chapter 6. Direct Scaffolding of Biomimetic Hydroxyapatite-gelatin Nanocomposites using Aminosilane Cross-linker for Bone Regeneration.....	89
6.1 Introduction.....	90
6.2 Materials and Methods.....	93
6.2.1 Materials	93
6.2.2 Sample preparation and conditions.....	94
6.2.3 Mechanical testing	95
6.2.4 Contact angle testing.....	95
6.2.5 Thermogravimetric analyzer (TGA) testing	96
6.2.6 Transmission electron microscopy (TEM)	96
6.2.7 Cell culture testing.....	97
6.2.8 Bone regeneration in rat calvarium defects	99
6.3 Results.....	99
6.4 Discussion.....	102
6.5 Conclusion	109
6.6 Acknowledgement	109
6.7 References.....	109
Chapter 7. In-situ Hybridization of Calcium Silicate and Hydroxyapatite-Gelatin Nanocomposite Enhances Physical Properties and <i>In Vitro</i> Osteogenesis.....	124
7.1 Introduction.....	125
7.2 Materials and Methods.....	129
7.2.1 Materials	129
7.2.2 Synthesis of GEMOSIL-CS samples.....	129

7.2.3 Compressive testing	130
7.2.4 Thermogravimetric analyzer (TGA) testing	130
7.2.5 Fourier transform infrared spectroscopy (FTIR)	131
7.2.6 Proliferation Assay.....	131
7.2.7 Picrosirious Staining	132
7.2.8 Alizarin Red Staining.....	132
7.2.9 Scanning and Transmission Electron Microscopy (SEM and TEM).....	133
7.3 Results.....	134
7.3.1 Physical properties and characterizations	134
7.3.2 <i>In vitro</i> osteogenic properties.....	137
7.4 Discussion	139
7.4.1 Physical properties and characterizations	139
7.4.2 <i>In vitro</i> osteogenic properties.....	144
7.5 Conclusion	146
7.6 References.....	147
Chapter 8. Conclusions and Future Work.....	164
8.1 Conclusions.....	165
8.2 Future work.....	166

LIST OF TABLES

Table 5.1 Particles distribution of different surfactant at various spots of the film.	88
Table 6.1 Composition of GEMOSIL nanocomposites.....	123
Table 7.1 Composition of GEMOSIL, GEMOSIL-CS and HAp-CS nanocomposites.....	163

LIST OF FIGURES

Figure 2.1 Formation of silver chloride cubic crystals is facilitated by the shrinking of sol-gel nanocomposite film.....	29
Figure 2.2 SEM images of silver chloride cubic crystals grown on the nanocomposite film at the room temperature.	29
Figure 2.3 TEM image of AgCl cubes and their electron beam diffraction pattern.	30
Figure 2.4 SEM images of AgCl crystals grown from the films of (a) 70, (b) 300, (c) 650, (d) 920 nm thick.	30
Figure 2.5 Geometry and average dimension of AgCl crystals are critically dependent on the thickness of nanocomposite film.	31
Figure 2.6 Time-lapse AFM images of a nanocomposite film after (a) 30, (b) 40, (c) 50, and (d) 60 minutes of drying in the air at the room temperature.....	32
Figure 3.1 (a) A stepwise procedure for producing interconnected silver network (b) A proposed mechanism explains the development of silver network	46
Figure 3.2 Evolution of the sample dimension during each treatment stage.....	46
Figure 3.3 The density of silver network was evaluated by measuring the size of individual fragments after breaking the annealed samples by force.....	47
Figure 3.4 (a) Hardness of the dried gels on Vickers scale after respectively drying the samples (b) Bulk electric resistivity of the annealed gels.....	48
Figure 3.5 SEM images of cross-sectional area of the annealed gel, which has been oven-dried at 80 °C for 4 hrs followed by annealing at 160 °C.....	49
Figure 4.1 The step-by-step procedure for producing bulk porous silver from a dry sol-gel silica containing AgNO ₃	61
Figure 4.2 A uniform porous structure can be seen on the silver solid sample produced using 70 µm size powder.....	62
Figure 4.3 (a) SEM images of the silver metal made from powder of 2 µm in diameter (b) High resolution image at 8,000x reveals the grain-like silver struts arranging in anisotropic order due to the packing of powder particles.	63
Figure 4.4 SEM images of three porous silver samples that were prepared respectively under (a) 100 MPa, (b) 200 MPa, and (c) 400 MPa, show that the size or pore struts decreases with the pressing pressure.....	64
Figure 4.5 (a) The size of pore struts in silver sponge decreases with the pressing pressure. (b) The interconnectivity of silver network increases with the pressing pressure.....	65
Figure 4.6 (a) Effect of silver on the stress-strain behavior of the annealed samples (b) The ultimate strength of annealed samples with the presence of silver network is 64% higher than that of silica only.....	65

Figure 5.1 Two different processes of producing patterned silver nanoparticles.....	83
Figure 5.2 AFM images of patterned surface containing silver nanoparticles created from different surfactant solutions.....	84
Figure 5.3 SEM images of patterned silver nanoparticles after heat-treating 3-MTS contained films at 160 °C are shown at (a) 2,500x and (b) 9,000x magnifications.	85
Figure 5.4 SEM images of patterned silver nanoparticles created by heat-treating 3-MTS contained film for 3 hours at 160 °C in 1 M AgNO ₃ solution. The images are shown at (1) 9,000x and (2) 40,000x.	85
Figure 5.5 SEM images of patterned silver nanoparticles created by heat-treating 3-MTS contained film for 2 hours at (a) 400 °C and (b) 600 °C.	86
Figure 5.6 SEM images of patterned silver nanoparticles that were prepared from patterned samples of mixing PEG-sol and ammonia water (a) with and (b) without 3-MTS followed by 20 hours of room temperature treatment in 1 M AgNO ₃ solution....	86
Figure 5.7 (a) EDX spectrum of Ag nanoparticles (b) UV-Vis spectrum of patterned silver nanoparticles created by treating PEG-sol sample containing either ammonia water (solid line) or nitric acid (dashed line) in 1 M AgNO ₃ solution at 25 °C. ..	87
Figure 6.1 GEMOSIL paste for direct scaffolding. Formable GEMOSIL paste can be molded into a (a) cube by hand and injected to form a (b) porous scaffold.	117
Figure 6.2 The compressive strength of GEMOSIL nanocomposites. The optimal compressive strengths of GEMOSIL nanocomposites are observed when enTMOS percentage is between 11 wt% and 19 wt%.....	117
Figure 6.3 Vickers hardness (HV) of GEMOSIL nanocomposites. HV increases with the amount of enTMOS ($p < 0.01$) and the aging time. HV reaches the maximum when sample contains 26.3 wt% of enTMOS.....	118
Figure 6.4 TGA analysis of GEMOSIL nanocomposites. Distinct weight drop patterns are attributed to the elimination of water, gelatin, and alkyl side groups.....	118
Figure 6.5 Theoretical predictions and experimentally measured weight percentages of aminosilica in GEMOSIL samples..	119
Figure 6.6 TEM images of (a) GEMOSIL-11 at 100 kx (inset at 200 kx) and (b) GEMOSIL-19 at 100 kx (inset at 200 kx) samples taken from the mixing step.....	119
Figure 6.7 Contact angles measurements show no obvious difference between HAp-Gel-PBS and GEMOSIL samples..	120
Figure 6.8 The growth curve of preosteoblasts, MC3T3-E1, was measured by formazan absorbance using CellTiter kits (Promega, Madison).....	120
Figure 6.9 Alizarin red stain for MC3T3-E1 at the differentiation day 14 shows mineral nodules.	121

Figure 6.10 The rat calvarium defect study shows the new bone formation 8 weeks after implantation of the (a) GEMOSIL-19 and (b) GEMOSIL-19-P25.	122
Figure 6.11 Setting mechanism for the GEMOSIL scaffold.	122
Figure 7.1 Compressive strength of GEMOSIL nanocomposites aging in 37 °C oven for 48 hours after mixing.	154
Figure 7.2 Compressive strength of GEMOSIL nanocomposites soaking in 37 °C PBS for 2 hours after mixing.	154
Figure 7.3 TGA results showed the weight loss versus temperature.	155
Figure 7.4 Theoretically calculated and experimentally measured weight remained of GEMOSIL samples after TGA 800 °C treatment.	155
Figure 7.5 FTIR spectrum of GEMOSIL nanocomposites. (a) GEMOSIL (b) GEMOSIL-CS1 (c) GEMOSIL-CS2.	156
Figure 7.6 XRD measurements of GEMOSIL composites after drying at 37 °C for 48 hours.	157
Figure 7.7 Growth characteristics of MC3T3 cells were assessed on both GEMOSIL and GEMOSIL-CS2.	157
Figure 7.8 Micrographs of Picrosirius stained MC3T3-E1 cells cultured on GEMOSIL and GEMOSIL-CS2 coated glass after 1, 4 and 7 days.	158
Figure 7.9 Mineralized nodule formation from MC3T3-E1 cells. Calcium deposition from MC3T3 cells cultured on both GEMOSIL and GEMOSIL-CS2 coated dishes were observed by Alizarin Red staining at 1, 4, 7, 14 and 21 days in culture.	159
Figure 7.10 Quantification results of mineralization characteristics of control, GEMOSIL and GEMOSIL-CS2 at 1, 4, 7, 14 and 21 days derived from color differences (δ) by CIELAB method.	160
Figure 7.11 SEM micrograph showed the cell proliferation potential on (a) GEMOSIL and (b) GEMOSIL-CS2 after (I) 4 and (II) 7 days in culture.	161
Figure 7.12 SEM and TEM images of GEMOSIL-CS2 nanocomposite samples after 7 days in culture	162

Chapter 1

Introduction

1.1 Introduction and motivation

To meet the increasing demands for multifunctional materials, rapid and versatile solutions to create such materials have been constantly sought. One of the feasible approaches is via hybridization of organic and inorganic components with one of the domains ranging from angstroms to several nanometers.¹⁻³ The resulting products can be broadly defined as nanocomposites. These hybrid materials, sometimes known as advanced materials, promise new applications in many fields such as optics,^{4, 5} electronics,^{6, 7} mechanics^{8, 9} and biology.^{10, 11} To realize the hybridization concept, efforts have been focused on using the sol-gel process to synthesize nanocomposites. In addition to its mild synthetic conditions at near ambient temperature,^{12, 13} the sol-gel process may utilize high purity of metallo-organic precursors in various organic solvents to produce high yields of highly processable colloidal products.^{14, 15} Although sol-gel approaches are versatile in these regards, several inherent properties limit their industrial applications. First, the interconnected 3-D network by the simultaneous hydrolysis and polycondensation consists of nanoporous (pore size < 5 nm) structures.¹⁴ These nanopores, though exhibiting high surface area, often limit the diffusion of gas and liquid within the nanocomposites.¹⁶ Second, chemical and physical interactions at the inner interfaces are considered critical in determining the overall properties. Although strong interfacial bonding between the intimate phases enhances the mechanical integrity,^{2, 13} it may suppress the fluid-like properties of polymer phases, reducing the permeability and diffusivity within nanopores, and often lead to uneven distribution of secondary fillers. Third, sol-gel materials tend to shrink when solvent

evaporates during drying. The internal stress accumulates during shrinking eventually causes crack and fragmentation.¹⁷ Though the sample fragmentation could be avoided by careful treatments, the side effects such as prolong processing time, deterioration, and uneven shrinkage cannot be avoided.

To overcome these problems, diffusion, pore size, shrinkage and stress-induced defects need further investigation. Thus, the research presented in this thesis will address these important questions such as whether these limitations can be utilized as a novel method to create new materials and new applications. The entire work presented by this thesis devotes to synthesis, evolution, mechanism of nanostructures and their potential applications in nanocrystal growth, nanoporous metals, metal-ceramic composites, nano-imprint thin film, and biomaterials particularly those in orthopedic applications. The studies focus on examination and utilization of inherent properties including nanoporous structure, interfacial bindings, shrinkage, and stress induced cracks to develop unique structures for multifunctional applications. The synthesized structures are studied by SEM, TEM, AFM, XRD and FTIR at various scales. Then, the properties of nanocomposites such as electrical, optical, mechanical and biocompatible properties are characterized. Furthermore, the formation mechanisms behind the synthesized structures will be extensively discussed and examined.

Part of the work presented in this thesis originates from close collaboration with the research group of Dr. Ching-Chang Ko (UNC-Chapel Hill, School of Dentistry, North Carolina, US), where the Hydroxyapatite-Gelatin (HAp-Gel) materials have been provided. They also provide the professional *in vitro* and *in vivo* testing on biomimetic nanocomposite scaffolds. The collaboration will be further described in detail in the following chapters.

We first explore the behaviors of polymers such as poly(ethylene glycol) (PEG) inside the silica pores by examining the nucleation and growth of AgCl at the surface of the porous matrix at room temperature. Recently, PEG-silica nanocomposites have been studied and applied for drug delivery devices.^{18, 19} The weak hydrogen bonding between matrix and polymer contributed to the mobility for controlled release of encapsulation biomolecules. Poly(ethylene glycol) is one of the most widely used polymer materials in chemical and medical sciences due to its excellent properties such as hydrophilicity, flexibility, lack of toxicity, and non-immunogenicity.²⁰ Based on the silica chemistry, PEG polymers with the ether oxygen atoms (hydrogen-bonding acceptor) can have a high affinity to silanol groups (hydrogen-bonding donor) of silica species via hydrogen-bonding interactions in the solution at room temperature.^{21, 22} Consequently, PEG polymers have been widely used as flocculants and structure-directing agents to prepare xerogels and nanoporous silica spheres.^{23, 24} Because of the hydrogen-bonding interactions between PEG and silica, the mobility of PEG upon immersion of PEG-silica in water solution can be modulated. As of today, the mobility of polymer phases within nanocomposites has been rarely studied for nanocrystal growth.

Thus, we propose that the mobile polymer phase may serve as a nuclei carrier for crystal growth under a controlled environment. It is also important to determine how pore structure and the pressure induced by the shrinkage affect the nucleation and growth of AgCl nanocrystals. Chapter 2 examines the feasibility of utilization of PEG-silica nanocomposites to self-assemble AgCl nanocrystals on the nanocomposites surface, where the self-growth of nanocrystal on the nanocomposites has been investigated by AFM measurements. Because of the weak hydrogen bonding between PEG and silica, the mobility of PEG facilitates crystal growth at open areas under the shrinkage induced stress. It was demonstrated that the shape and size of nanocrystals can be controlled by the thickness and composition of nanocomposite films. The study suggests a new method to control nanocrystal growth at mild reaction.

When the same process is carried out at 160 °C, silver metallization is possible. Chapter 3 describes the mobility of polymer phase within PEG-silica nanocomposites may be utilized to grow interconnected silver nanostructure. When stress was induced by the inherent shrinkage during sol-gel drying process, the polymer tends to fill into open spaces including surface and crack within nanocomposite monolith. Upon heat treatment, the polymer facilitates metal reduction and forms interconnected metal structure. These findings lead us to conclude that in order to enhance the connectivity of silver structure it is possible to utilize crack surfaces as the template. When the scale is small, polymer may no longer be needed if the diffusion length of Ag is more than the size of powder as polymer is sometimes not

favorable in several processes. Chapter 4 utilizes ground powder to validate our assumption that artificially produced cracks could serve as templates for silver nucleation and growth. A new robust porous structure of silver was successfully made. Parameters such as powder size and press pressure could be utilized to control the pore structures and sizes of porous metal foam. Metal foams have potential applications in mechanics, sound proof, electrode and catalyst due to their attractive properties such as light weight, porous structures, and high surface areas. Different synthesis methods have been demonstrated using powder metallurgy,^{25, 26} melt filling^{26, 27} and templating^{28, 29} etc. Although various structures with different pore sizes, pore structures, compositions and surface treatments can be derived,³⁰⁻³² several limitations such as lack of uniform, tunable, reproducible and robust properties still limit their industry applications. The simple and effective process proposed here could provide an alternate method to solve these problems.

By combining the results from room temperature and high temperature processes, chapter 5 introduces a simple method to self-assemble patterned silver nanoparticle arrays in order to examine how mobility of silver can be controlled on a quantifiable scale. In general, nanoparticles are characterized by their nanoscale size and high surface area. Therefore, extensive studies have been carried out to realize their applications in optical, electrical, mechanical and biomedical fields. In order to exploit their function and to apply them to the devices, the current major goal is to find an accurate, fast, and low-cost method to control the location of nanoparticles on substrates. However, synthesis of patterned nanoparticles

arrays have received limited success and only few methods have been proposed. Both top-down^{33, 34} and bottom-up^{35, 36} methods have been proposed but each shows its own limitations. Here, an alternative approach is demonstrated to self-assemble silver nanoparticles array on the patterned areas of thin films composed of polymer-silica nanocomposites. The present method utilizes the affiliation between thiol group and metals to control the metal ions mobility for selective deposition of silver nanoparticles. The silver nanoparticle arrays exhibit well-defined pattern, highly selective nanoparticle deposition and tunable nanoparticle sizes regardless the thin residual layers inherent from microcontact imprint methods.

Lastly, the present thesis focuses on investigating the effects of interactions between sol-gel silica and other nanocomposite components and the thickness of the sol-gel layer on mechanical properties. These studies were applied to the biomimetic hydroxyapatite-gelatin (HAp-Gel) system. Tissue engineering is a promising approach for tissue regeneration of bones, skins and organs.^{37, 38} The scaffolding structure is one of the most important factors to fulfill the criteria for clinical successes other than its biocompatibility, porous structures, biodegradability, and mechanical strength.³⁹ In order to achieve most of these requirements, several scaffolds were made by polymer materials that have 6 - 10 times inferior strength than bones.⁴⁰⁻⁴² Thus, new materials are required to fulfill the clinical usage of scaffolds. Composites have been considered to be the ideal materials, which could be synthesized to resemble the real bone. Thus, biomimetic materials such as hydroxyapatite-gelatin (HAp-

Gel)^{43, 44} and hydroxyapatite-collagen (HAp-Col)^{45, 46} has been studied extensively for bone regeneration. Various attempts have been made to cross-link HAp-Gel particles after dehydration and solidification^{47, 48} but limited success was found due to toxic cross-linkers, long setting time and insufficient mechanical strength. The question is raised that whether strong interaction between polymeric gelatin and silica at molecular scale within nanocomposites can fulfill these requirements. Chapter 6 introduces a new HAp-Gelatin modified siloxane (GEMOSIL) nanocomposites for bone regeneration applications.^{49, 50} The hydrogen bond induced by inherent protein structures of gelatin provides the formable and injectable properties of GEMOSIL paste. After setting, interfacial bondings between gelatin, hydroxyapatite and silica within nanocomposites have been found to enhance the mechanical properties. The formation of physical cross-linkage within nanocomposites eliminates the usage of toxic formaldehyde cross-linker and provides a potential scaffold application. However, slow setting and relative low mechanical properties of GEMOSIL materials still cannot satisfy the clinical needs. The utilization of strong bonding such as covalent bonding is required to further enhance its mechanical strength. The in-situ formation of biocompatible calcium silicate (CS) between silica and calcium hydroxide provides a new opportunity as presented by Chapter 7. The formation of strong interfacial covalent bonding greatly enhances mechanical integrity and strength. The leaching of calcium ions from calcium hydroxide also facilitates the formation of extracellular matrix and mineralization for bone regeneration. In addition to gelatin, the degradation of calcium hydroxide further enhances the biodegradability of bone grafts. Thus, GEMOSIL-CS nanocomposite scaffolds provide

high potentials for clinical tissue engineering applications. Finally, Chapter 8 will summarize relevant conclusions and address important future work.

1.2 References

1. Loy, D. A.; Shea, K. J., Bridged Polysilsesquioxanes - Highly Porous Hybrid Organic-Inorganic Materials. *Chemical Reviews* **1995**, 95, (5), 1431-1442.
2. Judeinstein, P.; Sanchez, C., Hybrid organic-inorganic materials: A land of multi-disciplinarity. *Journal of Materials Chemistry* **1996**, 6, (4), 511-525.
3. Shea, K. J.; Loy, D. A., Bridged polysilsesquioxanes. Molecular-engineered hybrid organic-inorganic materials. *Chemistry of Materials* **2001**, 13, (10), 3306-3319.
4. Costacurta, S.; Malfatti, L.; Falcaro, P.; Innocenzi, P., Photocurable silica hybrid organic-inorganic films for photonic applications. *Journal of Sol-Gel Science and Technology* **2007**, 44, (1), 59-64.
5. Kim, H. K.; Kang, S. J.; Choi, S. K.; Min, Y. H.; Yoon, C. S., Highly efficient organic/inorganic hybrid nonlinear optic materials via sol-gel process: Synthesis, optical properties, and photobleaching for channel waveguides. *Chemistry of Materials* **1999**, 11, (3), 779-788.
6. Guo, Y.; Mylonakis, A.; Zhang, Z. T.; Yang, G. L.; Lelkes, P. I.; Che, S. N.; Lu, Q. H.; Wei, Y., Templated synthesis of electroactive periodic mesoporous organosilica bridged with oligoaniline. *Chemistry-a European Journal* **2008**, 14, (9), 2909-2917.

7. Gun, J.; Lev, O., Sol-gel derived, ferrocenyl-modified silicate-graphite composite electrode: Wiring of glucose oxidase. *Analytica Chimica Acta* **1996**, 336, (1-3), 95-106.
8. Li, G. Z.; Wang, L. C.; Toghiani, H.; Daulton, T. L.; Koyama, K.; Pittman, C. U., Viscoelastic and mechanical properties of epoxy/multifunctional polyhedral oligomeric silsesquioxane nanocomposites and epoxy/ladderlike polyphenylsilsesquioxane blends. *Macromolecules* **2001**, 34, (25), 8686-8693.
9. Choi, J.; Yee, A. F.; Laine, R. M., Organic/inorganic hybrid composites from cubic silsesquioxanes. Epoxy resins of octa(dimethylsiloxyethylcyclohexylepoxide) silsesquioxane. *Macromolecules* **2003**, 36, (15), 5666-5682.
10. Darder, M.; Aranda, P.; Ruiz-Hitzky, E., Bionanocomposites: A new concept of ecological, bioinspired, and functional hybrid materials. *Advanced Materials* **2007**, 19, (10), 1309-1319.
11. Tan, X. C.; Tian, Y. X.; Cai, P. X.; Zou, X. Y., Glucose biosensor based on glucose oxidase immobilized in sol-gel chitosan/silica hybrid composite film on Prussian blue modified glass carbon electrode. *Analytical and Bioanalytical Chemistry* **2005**, 381, (2), 500-507.
12. Sanchez, C.; Ribot, F., Design of Hybrid Organic-Inorganic Materials Synthesized Via Sol-Gel Chemistry. *New Journal of Chemistry* **1994**, 18, (10), 1007-1047.
13. Schubert, U.; Husing, N.; Lorenz, A., Hybrid Inorganic-Organic Materials by Sol-Gel Processing of Organofunctional Metal Alkoxides. *Chemistry of Materials* **1995**, 7, (11), 2010-2027.

14. Hench, L. L.; West, J. K., The Sol-Gel Process. *Chemical Reviews* **1990**, 90, (1), 33-72.
15. Wen, J. Y.; Wilkes, G. L., Organic/inorganic hybrid network materials by the sol-gel approach. *Chemistry of Materials* **1996**, 8, (8), 1667-1681.
16. Hosticka, B.; Norris, P. M.; Brenizer, J. S.; Daitch, C. E., Gas flow through aerogels. *Journal of Non-Crystalline Solids* **1998**, 225, (1), 293-297.
17. Jeffrey C. Brinker, G. W. S., *Sol-gel science : the physics and chemistry of sol-gel processing*. Academic Press: Boston, 1990.
18. Yague, C.; Moros, M.; Grazu, V.; Arruebo, M.; Santamaria, J., Synthesis and stealthing study of bare and PEGylated silica micro- and nanoparticles as potential drug-delivery vectors. *Chemical Engineering Journal* **2008**, 137, (1), 45-53.
19. Chen, F. H.; Zhang, L. M.; Chen, Q. T.; Zhang, Y.; Zhang, Z. J., Synthesis of a novel magnetic drug delivery system composed of doxorubicin-conjugated Fe₃O₄ nanoparticle cores and a PEG-functionalized porous silica shell. *Chemical Communications* 46, (45), 8633-8635.
20. Martin, J.; Hosticka, B.; Lattimer, C.; Norris, P. M., Mechanical and acoustical properties as a function of PEG concentration in macroporous silica gels. *Journal of Non-Crystalline Solids* **2001**, 285, (1-3), 222-229.
21. Rodrigues, D. E.; Brennan, A. B.; Betrabet, C.; Wang, B.; Wilkes, G. L., Structural Features of Sol-Gel Derived Hybrid Inorganic Organic Network Ceramer Materials by Small-Angle X-Ray-Scattering. *Chemistry of Materials* **1992**, 4, (6), 1437-1446.

22. VanAlstine, J. M.; Malmsten, M., Poly(ethylene glycol) amphiphiles: Surface behavior of biotechnical significance. *Langmuir* **1997**, 13, (15), 4044-4053.
23. Oh, C.; Lee, Y. G.; Choi, T. S.; Jon, C. U.; Oh, S. G., Facile synthesis of PEG-silica hybrid particles using one-step sol-gel reaction in aqueous solution. *Colloids and Surfaces a-Physicochemical and Engineering Aspects* **2009**, 349, (1-3), 145-150.
24. Sun, Q. Y.; Beelen, T. P. M.; van Santen, R. A.; Hazelaar, S.; Vrieling, E. G.; Gieskes, W. W. C., PEG-mediated silica pore formation monitored in situ by USAXS and SAXS: Systems with properties resembling diatomaceous silica. *Journal of Physical Chemistry B* **2002**, 106, (44), 11539-11548.
25. Yu, C. J.; Eifert, H. H.; Banhart, J.; Baumeister, J., Metal foaming by a powder metallurgy method: Production, properties and applications. *Materials Research Innovations* **1998**, 2, (3), 181-188.
26. Dunand, D. C., Processing of titanium foams. *Advanced Engineering Materials* **2004**, 6, (6), 369-376.
27. Durian, D. J., Bubble-scale model of foam mechanics: Melting, nonlinear behavior, and avalanches. *Physical Review E* **1997**, 55, (2), 1739-1751.
28. Davies, G. J.; Zhen, S., Metallic Foams - Their Production, Properties and Applications. *Journal of Materials Science* **1983**, 18, (7), 1899-1911.
29. Warren, S. C.; Messina, L. C.; Slaughter, L. S.; Kamperman, M.; Zhou, Q.; Gruner, S. M.; DiSalvo, F. J.; Wiesner, U., Ordered mesoporous materials from metal nanoparticle-block copolymer self-assembly. *Science* **2008**, 320, (5884), 1748-1752.

30. Wang, J. G.; Xiao, Q.; Zhou, H. J.; Sun, P. C.; Yuan, Z. Y.; Li, B. H.; Ding, D. T.; Shi, A. C.; Chen, T. H., Budded, mesoporous silica hollow spheres: Hierarchical structure controlled by kinetic self-assembly. *Advanced Materials* **2006**, 18, (24), 3284-+.
31. Kresge, C. T.; Leonowicz, M. E.; Roth, W. J.; Vartuli, J. C.; Beck, J. S., Ordered Mesoporous Molecular-Sieves Synthesized by a Liquid-Crystal Template Mechanism. *Nature* **1992**, 359, (6397), 710-712.
32. Tanev, P. T.; Pinnavaia, T. J., A Neutral Templating Route to Mesoporous Molecular-Sieves. *Science* **1995**, 267, (5199), 865-867.
33. Hamann, H. F.; Woods, S. I.; Sun, S. H., Direct thermal Patterning of self-assembled nanoparticles. *Nano Letters* **2003**, 3, (12), 1643-1645.
34. Corbierre, M. K.; Beerens, J.; Beauvais, J.; Lennox, R. B., Uniform one-dimensional arrays of tunable gold nanoparticles with tunable interparticle distances. *Chemistry of Materials* **2006**, 18, (11), 2628-2631.
35. Fernandes, R.; Li, M.; Dujardin, E.; Mann, S.; Kanaras, A. G., Ligand-mediated self-assembly of polymer-enveloped gold nanoparticle chains and networks. *Chemical Communications* 46, (40), 7602-7604.
36. Korth, B. D.; Keng, P.; Shim, I.; Bowles, S. E.; Tang, C.; Kowalewski, T.; Nebesny, K. W.; Pyun, J., Polymer-coated ferromagnetic colloids from well-defined macromolecular surfactants and assembly into nanoparticle chains. *Journal of the American Chemical Society* **2006**, 128, (20), 6562-6563.
37. Langer, R.; Vacanti, J. P., Tissue Engineering. *Science* **1993**, 260, (5110), 920-926.

38. Griffith, L. G.; Naughton, G., Tissue engineering - Current challenges and expanding opportunities. *Science* **2002**, 295, (5557), 1009-+.
39. Hutmacher, D. W., Scaffolds in tissue engineering bone and cartilage. *Biomaterials* **2000**, 21, (24), 2529-2543.
40. Seal, B. L.; Otero, T. C.; Panitch, A., Polymeric biomaterials for tissue and organ regeneration. *Materials Science & Engineering R-Reports* **2001**, 34, (4-5), 147-230.
41. Hubbell, J. A., Synthetic biodegradable polymers for tissue engineering and drug delivery. *Current Opinion in Solid State & Materials Science* **1998**, 3, (3), 246-251.
42. Zioupos, P.; Currey, J. D., Changes in the stiffness, strength, and toughness of human cortical bone with age. *Bone* **1998**, 22, (1), 57-66.
43. Chang, M. C.; Ko, C. C.; Douglas, W. H., Preparation of hydroxyapatite-gelatin nanocomposite. *Biomaterials* **2003**, 24, (17), 2853-2862.
44. Kim, H. W.; Kim, H. E.; Salih, V., Stimulation of osteoblast responses to biomimetic nanocomposites of gelatin-hydroxyapatite for tissue engineering scaffolds. *Biomaterials* **2005**, 26, (25), 5221-5230.
45. Du, C.; Cui, F. Z.; Zhu, X. D.; de Groot, K., Three-dimensional nano-HAp/collagen matrix loading with osteogenic cells in organ culture. *Journal of Biomedical Materials Research* **1999**, 44, (4), 407-415.
46. Itoh, S.; Kikuchi, M.; Takakuda, K.; Nagaoka, K.; Koyama, Y.; Tanaka, J.; Shinomiya, K., Implantation study of a novel hydroxyapatite/collagen (HAp/Col) composite into

- weight-bearing sites of dogs. *Journal of Biomedical Materials Research* **2002**, 63, (5), 507-515.
47. Chang, M. C.; Douglas, W. H., Cross-linkage of hydroxyapatite/gelatin nanocomposite using imide-based zero-length cross-linker. *Journal of Materials Science-Materials in Medicine* **2007**, 18, (10), 2045-2051.
48. Chang, M. C.; Ko, C. C.; Douglas, W. H., Modification of hydroxyapatite/gelatin composite by polyvinylalcohol. *Journal of Materials Science* **2005**, 40, (2), 505-509.
49. Luo, T. J. M.; Ko, C. C.; Chiu, C. K.; Llyod, J.; Huh, U., Aminosilane as an effective binder for hydroxyapatite-gelatin nanocomposites. *Journal of Sol-Gel Science and Technology* **2010**, 53, (2), 459-465.
50. Chiu C. C., F. J., Luo T. J. M., Geng H., Lin F. C., Ko, C. C., Direct scaffolding of biomimetic hydroxyapatite-gelatin nanocomposites using aminosilane cross-linker for bone regeneration. *Journal of Materials Science: Materials in Medicine* **2012**, DOI: 10.1007/s10856-012-4691-6.

Chapter 2

Formation of AgCl Cubic Crystals Induced by Shrinkage of Sol-Gel Silica Substrate

Chi-Kai Chiu, Yong-Jae Choi, Tzy-Jiun M. Luo

Department of Materials Science and Engineering
North Carolina State University, Raleigh, NC 27606

Abstract

Nucleation and growth of AgCl cubic crystals at the surface of sol-gel synthesized silica films containing AgCl nuclei and poly(ethylene glycol)/ethylene glycol as diffusion-controlled media has been successfully demonstrated. Cubic shaped crystals were observed when the film shrank after it was exposed to air at the room temperature, and both shape and size of the crystals were found to be dependent on the film thickness. When the film thickness was in the range of 70 ~ 250 nm, cubic shaped crystals with size between 120 ~ 250 nm were produced. Elliptical crystals with size and height between 200 ~ 400 nm were found when film thickness was in the range of 200 ~ 400 nm. These cubes exhibited predominant {200} facets as indicated by the electron beam diffraction patterns. The ability to use nanoporous film as the nanoparticle source to grow crystals with desired orientation, shape, and dimensions may open new ways to pattern and fabricate well-defined nanocrystals on solid surfaces.

2.1 Introduction

Crystal growth based on orientated aggregation of nano-scale crystals of low solubility compounds such as semiconductors,¹⁻³ metal oxides,⁴⁻⁶ metal oxyhydroxides,^{7,8} and metals^{9,10} has been an interesting topic. This growth mechanism explains why crystals of well-defined morphology can be prepared under diffusion-limited condition from solutions containing nanoparticle or nanocrystals suspension. This assembly process begins with collision of nanocrystals driven by Brownian motion, followed by rotation of two adjacent crystals until the 2D crystal planes at the particle-particle interface are coherent, which results in a new attachment of crystalline particles.^{11,12} Such growth has also been found to be unaffected by the adhering organic molecules and could lead to not only single crystals but twins, stacking faults, and intergrowths as well.¹³ In addition, by knowing how to control the growth mechanism, it is possible to produce crystals of desired size and geometry.^{5,6,14} However, pre-aggregated nanocrystals without chemical stabilizers in general are unstable and difficult to control due to that nanocrystals could quickly combine together and form larger crystals in solution.¹⁵ Although it is possible to capture pre-aggregated crystals in nanoporous media, their mobility is often limited by the pore size, making this technique inadequate for microscopic or surface patterning application. In addition to diffusion control, other approaches include nonaqueous gel to overcome slow diffusion problem.¹⁶

Here we demonstrate that meta-stable AgCl nuclei when immobilized within a sol-gel thin film containing poly(ethylene glycol) (PEG) and ethylene glycol as the mobile phase are

able to migrate to the surface of the film and grow into larger crystals of same orientation when the nanoporous film shrinks during the drying of the film (Figure 2.1). Silica films synthesized by sol-gel method generally contain interconnected nanopores where diffusion of liquid and ions is able to take place,¹⁷ and therefore sol-gel materials have been used to regulate ion diffusion for crystal growth.^{18, 19} We have chosen silver chloride as our model compound because of its low solubility in aqueous environment ($K_{sp} = 1.77 \times 10^{-10}$). The polymer mobile phase under the influence of physical shrinkage of sol-gel material is able to carry AgCl nuclei to the surface where the morphology and dimensions of the resulting AgCl crystals are controlled by film thickness. The ability to use sol-gel thin films as the nanoparticle reservoir to grow crystals of desired shape and dimensions may open a new opportunity for creating patterned nanostructures on the substrates.

2.2 Experimental procedures

2.2.1 Preparation of PEG-sol

TMOS-sol was prepared by mixing 3.6 mL of deionized water and 15.2 mL of tetramethyl orthosilicate (TMOS). Upon adding 80 μ L of 0.5 N HCl, the mixture was immediately placed in an ice bath and vigorously stirred for 2 min until the solution became clear and uniform. Then, the mixture was sonicated in sonicator bath at room temperature for 20 min. The resulting solution (TMOS-sol) should be colorless and particle free. PEG-sol was prepared by adding 3.6 mL of deionized water and 7.2 mL of poly(ethylene glycol) (PEG, M.W. = 300 g/mol) into the TMOS-sol. Later, methanol was removed from the

mixture by rotary evaporation under 200 mbar reduced pressure at 45 °C for 35 minutes. The final solution was a clear and viscous liquid (PEG-sol).

2.2.2 Preparation of sol-gel thin film

The silicon substrates were prepared by cutting silicon wafer into each 12x12 mm size and then sonicated in isopropyl alcohol and methanol for 10 min. After drying by purging air, the silicon substrates were O₂ plasma-treated for another 2 min. A mixture containing PEG-sol, AgNO₃ and ethylene glycol was prepared as follows. A solution containing 200 µL of PEG-sol and 150 µL of 0.3 M silver nitrate solution was sonicated for 5 min in the ice bath. Then, 50 µL of 16 M nitric acid and 112.5 µL of ethylene glycol were added into the mixture, and the solution was sonicated for another 2 min in the ice bath. Each 10 µL of mixture was quickly transferred onto the silicon substrate and then covered with a piece of flat polycarbonate plate. Here polycarbonate plate served as the template to produce a flat and smooth surface after the liquid solidified. Films of different thickness have been created either by varying the amount of mixture solution or by applying different weight on top of the polymer template. The typical gelation time was about 3 min when nitric acid was used. After 2 hours of aging, the polycarbonate plate was removed and allowed to dry in the air. The film was initially clear then gradually its surface turned whitish. After drying for 24 hours, the samples were observed using SEM and TEM. Thickness of crystals and film were measured on AFM. To prepare sol-gel samples containing poly(vinylpyrrolidone) (PVP), an ethylene glycol solution containing 0.6 M PVP was used instead of pure ethylene glycol.

2.2.3 SEM, TEM, and AFM observation

Scanning electron microscope (SEM) observation was carried out on a field emission microscope (JEOL JSM-6400) under an acceleration voltage of 5 kV. The silicon substrates containing the sol-gel films were placed into SEM chamber without prior to depositing metal conductive layer. Transmission electron micrograph (TEM) was taken on JEOL 2000FX microscope under an accelerated voltage of 200 kV for both images and electron diffraction. To prepare the samples suitable for TEM experiment, formvar/carbon-coated TEM grids were first immersed into the mixture solution, and dried at room temperature. Thickness of the crystals on the samples was measured using Veeco Caliber AFM. The tapping mode scanning method and a silicon AFM cantilever were utilized to image the surface of nanocomposite film in order to reduce the chance of surface alternation by the movement of the AFM tips. To perform time-lapse AFM measurement, sample was placed inside AFM immediately after the polycarbonate template was removed. All images were taken in the air at the designated time under tapping mode.

2.3 Results and discussion

Volume shrinkage of sol-gel produced silica materials is a common phenomenon and it is typically accompanied by solvent evaporation inside the material. The shrinking is due to the collapse of nanoporous structures under the influence of capillary force of the solvent during solvent evaporation. Sol-gel silica matrix typically exhibits 30~50% of volume reduction during drying. In general, the shrinkage rate is independent of drying time but is

highly affected by the pore size.²⁰ The amount of shrinkage drops to ~10% when poly(ethylene glycol) (PEG) is present. Here PEG has been found to maintain the porosity and pore size of sol-gel material while remains mobile in the pore structures due to weak interactions between PEG and silica matrix,^{21,22} and therefore it helps to maintain a constant shrinkage rate by slowly diffusing out of silica matrix.

Figure 2.2a and 2.2b are SEM micrograms of silver chloride cubic crystals grown on the film surface after the film has been exposed to air for 24 hours. All corners on the cubes appear to be truncated and the size of cubes was in the range of 130-180 nm. If PVP was present in the film, silver chloride cubes of sharper corners were produced (Figure 2.2c~d). It is known that the oxygen atoms of PVP preferentially bind to {100} crystallographic planes of FCC silver and therefore they reduce the growth rate on {100} facets. Because silver atoms on the {100} faces of both silver and silver chloride have similar periodicity as it has been shown that a layer of AgCl (100) lattice could grow on Ag (100) face,²³ PVP is able to inhibit AgCl {100} faces, reducing the area of {111} faces. This morphology-modifying effect^{24,25} also explains why AgCl nuclei dissolve and grow into perfect cubic shape on the film surface. Individual cubes were further examined using TEM microscope, where metallic silver reduced by electron beam was observed (the dark area on Figure 2.3a), which is similar to the previous study.²⁶ The electron diffraction pattern of the cubic shaped crystal confirms that each cube is single crystal and its diffraction pattern corresponds to

(200), which presents the largest face on the AgCl crystal (Figure 2.3b). The weak diffraction pattern of (111) face indicates the presence of truncated facet at each corner of the cubes.

In these experiments, the silver chloride nuclei were carried away by PEG/EG mixture and grow at the surface of silica matrix. The solution for preparing the silica films contains trace amount of Cl^- , estimated to be 2.7 mM, which should produce $\sim 2.7 \times 10^{-3}$ M of AgCl crystals. Cl^- ion was initially introduced to the TMOS-sol solution by HCl solution as it was used as the acid catalyst for sol-gel reaction. On the contrary, when we replaced HCl solution with a HNO_3 solution and performed the same experiment, no crystals were observed on the film surface. Because the size of cubes is significantly larger than the pore size of sol-gel matrix, which has been estimated to be 10~12 nm,^{27,28} it shows that the formation of nanocube can be explained using Ostwald ripening of meta-stable AgCl nuclei at the surface of the film substrate. Because the sol-gel solution has been mixed with nitric acid to induce rapid gelation, we expect the average pore size should be even smaller than 10 nm. In addition, we found that the size of cubic crystals is related to the film thickness (Figure 2.4a~d), which proves that the assembly of AgCl cubes is affected by the number of nuclei. On the films with thickness of 70, 300, 650, and 920 nm, the size of the crystal increases with film thickness while the area density of cubes decreases. SEM images also show that morphology of silver crystals becomes elliptical shaped when the film is thicker than 400 nm. The detail correlation between the crystal dimensions and film thickness is further summarized in Figure 2.5, where both morphology and dimensions of crystals are plotted.

Dimensions of crystals are proportional to the film thickness. When the film is 70 ~ 250 nm thick, cubic shaped crystals of 120 ~ 250 nm size are produced. While in this range, height of crystals determined by AFM was found to be equal to the edge length, which confirms that the crystals are cubic shaped. When film thickness is 250 ~ 400 nm, spherical shaped crystals with size and height between 250 ~ 400 nm are observed (Figure 2.4). On the film of more than 400 nm thick, elliptical shaped particles with the maximum height up to 400 nm were formed. Compared with the crystals on the film of no PVP, we observed PVP does not significantly change the dimensions of crystals except that their sizes are slightly smaller. These results indicate the growth mechanism in the vertical direction is limited while in the lateral direction is not.

Time-lapse AFM images of a freshly prepared film prove that nuclei appear and grow at the surface of the film (Figure 2.6). Each image of the sol-gel film was respectively scanned at 30, 40, 50, and 60 min after the polycarbonate template was removed. Initially nuclei appeared to be small particles on the surface, and then both size and height of the particles increased with time while the location of particles remained unchanged. In addition, the surface of the film did not exhibit topographic change and no apparent liquid phase was observed on the surface of nanocomposite film by the AFM either. It indicates the formation of crystal occurred directly on the substrate without involving large amount of polymer liquid on the surface. The height of crystal at the center of the AFM image increased from 10 nm (after 30 mins) to 20 nm (after 60 mins) with an estimated growth rate of ~10 nm/hr. This

value is also consistent with the results in Figure 2.4 where the height of crystals after 24 hours is between 100 nm and 400 nm. We postulate that nuclei were pushed to the surface of films due to the shrinking of the films and assembled at the bottom and side faces of each crystal at the film surface where the assembly also helped to lift the crystals and contribute to the increase of the crystal size and height. Other study has shown that the major facets of AgCl nanocrystals that nucleate directly inside a porous matrix are {200} and {111}.²⁹ This explains why we have observed {200} facet to be the major faces of crystals. The capillary action of polymer liquid at each side of cubic crystals is responsible for the lateral growth of the crystals. When the dimensions of crystals are beyond ~200 nm, edges become dull and develop into spherical shape, which also contributes to the overall height of crystal to 400 nm. It is possible that the limit of capillary action of liquid and the mass of crystals prevent the height of crystals from growing beyond 400 nm while continuously contributing to the elliptical shape of crystals.

The K_{sp} value of AgCl in water is 1.77×10^{-10} and the concentration of free Cl^- ion in the solution is estimated to be 5.95×10^{-10} M. This value is 7 orders of magnitude smaller than the existing AgCl concentration at 2.7×10^{-3} M, which is expected to be even lower when AgCl is dissolved in polymer and methanol solutions. Therefore the concentration of free ion is too low to grow new crystals observable under AFM. We postulate that the existing AgCl nuclei are preserved inside the pore structures of silica matrix after gelation. In general, the critical radius of AgCl nuclei estimated by Klein et al., is just a few Ångstroms, and its size grows to

40 nm after 60~100 seconds of mixing using turbidity measurement.³⁰ The sol-gel prepared film in our study typically solidifies in 3 minutes after mixing with nitric acid solutions. The colloidal solution of TMOS-sol is considered viscous and it should reduce the mobility of AgCl nuclei. We consider 3 minutes of gelation window is too short for AgCl nuclei to develop into larger size. Hence, the size of meta-stable nuclei inside the nanoporous films was preserved until they migrated to the surface. On the other hand, when sol-gel solution was prepared without adding nitric acid, gelation did not occur until 6 hours later, and we found that the resulting composite films did not grow AgCl crystals on the surface after the template was removed. In addition, we observed that sol-gel solution became cloudy when the solution remained in liquid state for more than 2 hours, indicating that the large size AgCl particles formed in the solution. Poly(ethylene glycol) (PEG, M.W. = 300) and ethylene glycol together were used as the mobile phase and the previous studies show that PEG does not bind strongly to the silica matrix and could diffuse to the surface of silica matrix during aging. We have also observed significantly lower numbers of AgCl crystals on the films containing no PEG and ethylene glycol. When the film contained only PEG, crystals took much longer to appear possibly due to high viscosity, whereas the films containing only ethylene glycol seemed to shrink too quickly and prevented AgCl from migrating to the surface. Shrinking of sol-gel material is in general an irreversible process and occurs rapidly when solvent evaporates. Overall, our results show that AgCl nuclei preserved inside the nanoporous structures of sol-gel matrix remain to be meta-stable and are able to grow into larger crystals when transported to the surface.

2.4 Conclusion

We have successfully utilized gelation and shrinking of sol-gel thin film that contains meta-stable AgCl nuclei to create cubic crystals and demonstrated their dimensions and morphology are controlled by the film thickness. Both the edge length and the height of crystals increase with film thickness with the maximum height to be 400 nm. This demonstration represents a new possibility of using sol-gel thin film as a versatile reservoir to preserve unstable nanoparticles at higher concentration for creating crystals with controllable orientation and dimension.

2.5 References

1. Pacholski, C.; Kornowski, A.; Weller, H. *Angew. Chem.-Int. Edit.* 2002, *41*, 1188-1191.
2. Cho, K. S.; Talapin, D. V.; Gaschler, W.; Murray, C. B. *Journal of the American Chemical Society* 2005, *127*, 7140-7147.
3. Tang, Z. Y.; Kotov, N. A.; Giersig, M. *Science* 2002, *297*, 237-240.
4. Oskam, G.; Hu, Z. S.; Penn, R. L.; Pesika, N.; Searson, P. C. *Phys. Rev. E* 2002, *66*, 4.
5. He, T.; Chen, D. R.; Jiao, X. L. *Chem. Mat.* 2004, *16*, 737-743.
6. Gehrke, N.; Colfen, H.; Pinna, N.; Antonietti, M.; Nassif, N. *Cryst. Growth Des.* 2005, *5*, 1317-1319.
7. Banfield, J. F.; Welch, S. A.; Zhang, H. Z.; Ebert, T. T.; Penn, R. L. *Science* 2000, *289*, 751-754.
8. Alivisatos, A. P. *Science* 2000, *289*, 736-737.

9. Lu, L.; Kobayashi, A.; Kikkawa, Y.; Tawa, K.; Ozaki, Y. *J. Phys. Chem. B* 2006, *110*, 23234-23241.
10. Giersig, M.; Pastoriza-Santos, I.; Liz-Marzan, L. M. *Journal of Materials Chemistry* 2004, *14*, 607-610.
11. Penn, R. L.; Oskam, G.; Strathmann, T. J.; Searson, P. C.; Stone, A. T.; Veblen, D. R. *J. Phys. Chem. B* 2001, *105*, 2177-2182.
12. Huang, F.; Zhang, H. Z.; Banfield, J. F. *Nano Lett.* 2003, *3*, 373-378.
13. Penn, R. L.; Banfield, J. F. *American Mineralogist* 1998, *83*, 1077-1082.
14. Penn, R. L. *J. Phys. Chem. B* 2004, *108*, 12707-12712.
15. Gurlo, A.; Barsan, N.; Weimar, U.; Ivanovskaya, M.; Taurino, A.; Siciliano, P. *Chem. Mat.* 2003, *15*, 4377-4383.
16. Doxsee, K. M.; Chang, R. C.; Chen, E.; Myerson, A. S.; Huang, D. P. *Journal of the American Chemical Society* 1998, *120*, 585-586.
17. Koone, N.; Shao, Y.; Zerda, T. W. *Journal of Physical Chemistry* 1995, *99*, 16976-16981.
18. Fernandez-Diaz, L.; Astilleros, J. M.; Pina, C. M. *Chemical Geology* 2006, *225*, 314-321.
19. Zayat, M.; Einot, D.; Reisfeld, R. *Journal of Sol-Gel Science and Technology* 1997, *10*, 67-74.
20. Hench, L. L.; Wilson, M. J. R. *Journal of Non-Crystalline Solids* 1990, *121*, 234-243.
21. Higuchi, T.; Kurumada, K.; Nagamine, S.; Lothongkum, A. W.; Tanigaki, M. *Journal of Materials Science* 2000, *35*, 3237-3243.

22. Baker, G. A.; Jordan, J. D.; Bright, F. V. *Journal of Sol-Gel Science and Technology* 1998, *11*, 43-54.
23. Kitson, M.; Lambert, R. M. *Surface Science* 1980, *100*, 368-380.
24. Taubert, A.; Glasser, G.; Palms, D. *Langmuir* 2002, *18*, 4488-4494.
25. Deng, Y.; Nan, C. W.; Guo, L. *Chem. Phys. Lett.* 2004, *383*, 572-576.
26. Yan, Z. J.; Compagnini, G.; Chrisey, D. B. *Journal of Physical Chemistry C* 2011, *115*, 5058-5062.
27. Nguyen, D. T.; Smit, M.; Dunn, B.; Zink, J. I. *Chem. Mat.* 2002, *14*, 4300-4306.
28. Bhatia, R. B.; Brinker, C. J.; Gupta, A. K.; Singh, A. K. *Chem. Mat.* 2000, *12*, 2434-2441.
29. Trofimchuk, E. S.; Nikonorova, N. I.; Chagarovskii, A. O.; Volynskii, A. L.; Bakeev, N. *F. J. Phys. Chem. B* 2005, *109*, 16278-16283.
30. Berry, C. R.; Skillman, D. C. *Journal of Physical Chemistry* 1964, *68*, 1138-1143.

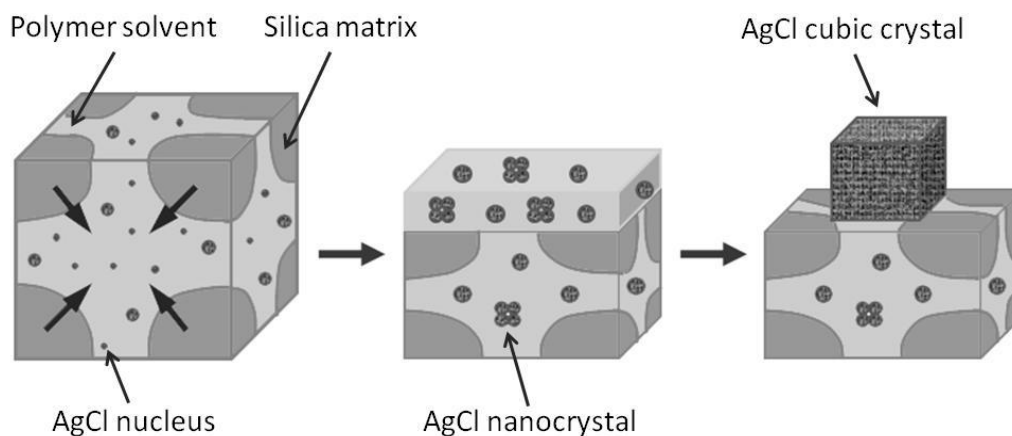


Figure 2.1 Formation of silver chloride cubic crystals is facilitated by the shrinking of sol-gel nanocomposite film, during which the film reduces its thickness and pushes silver chloride nuclei to the surface where they dissolve and grow on cubic shaped crystals via Ostwald Ripening mechanism.

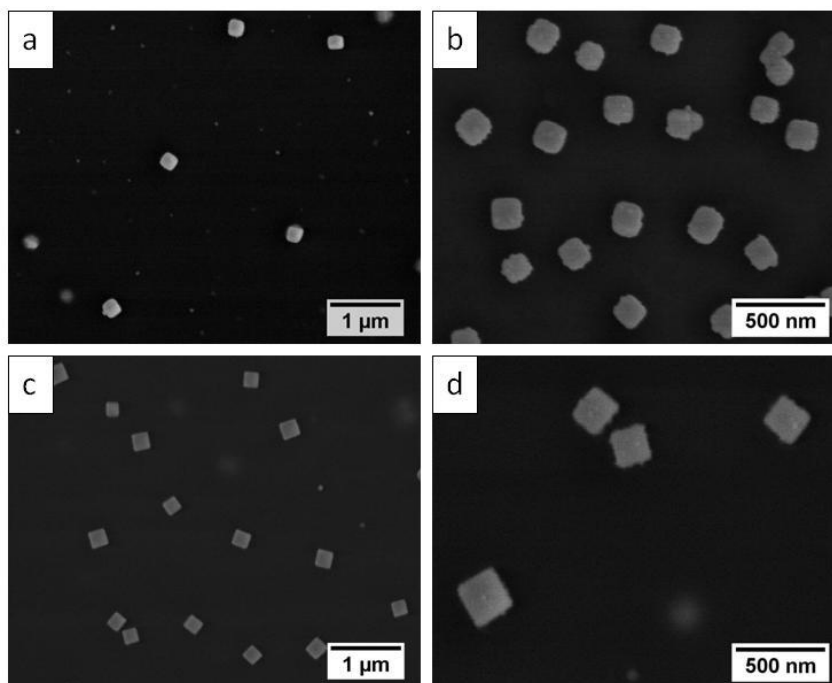


Figure 2.2 SEM images of silver chloride cubic crystals grown on the nanocomposite film at the room temperature. Truncated cubes shown in (a) low and (b) high magnification are observed on the film containing no polyvinylpyrrolidone (PVP) in the matrix. Cubes with sharper corners at (c) low and (d) high magnification are found when the film contains PVP.

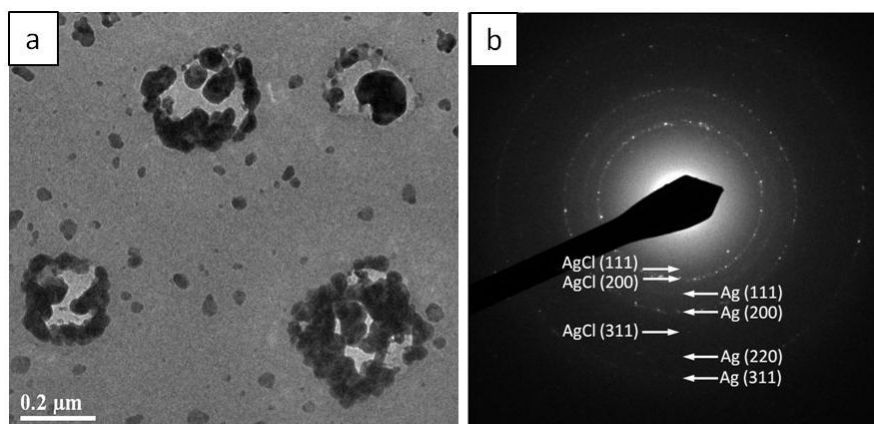


Figure 2.3 TEM image of AgCl cubes and their electron beam diffraction pattern. (a) The dark area on the AgCl crystals is the result of metallic silver being reduced from AgCl during the imaging. (b) Electron beam diffraction pattern indicates that the AgCl cubes are single crystal with a predominant (200) facet.

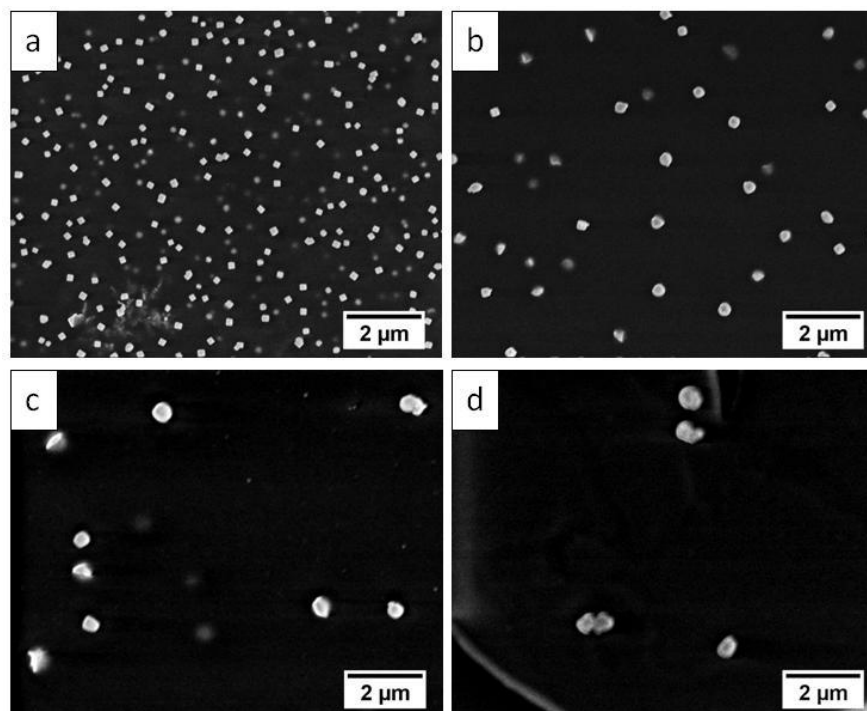


Figure 2.4 SEM images of AgCl crystals grown from the films of (a) 70, (b) 300, (c) 650, (d) 920 nm thick. Size of the crystals increases with film thickness while the density of particles decreases with the thickness. Please note that crystals on the film of 70 nm thick (a) are cubic shape.

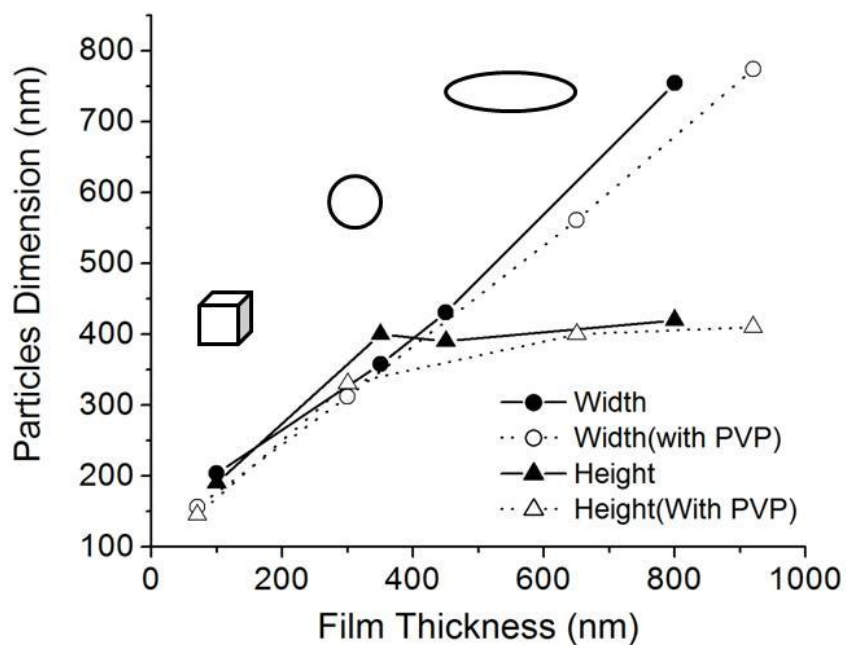


Figure 2.5 Geometry and average dimension of AgCl crystals are critically dependent on the thickness of nanocomposite film. Cubic shape crystals are observed when the film thickness is under 200 nm, while crystals of spherical and elliptical shape are respectively observed when the thickness is 250~400 nm and > 400 nm range. Dimensions of crystals are proportional to the film thickness but the height of crystals only reaches a maximum value of 400 nm. The presence of PVP shows no effect on the dimensions.

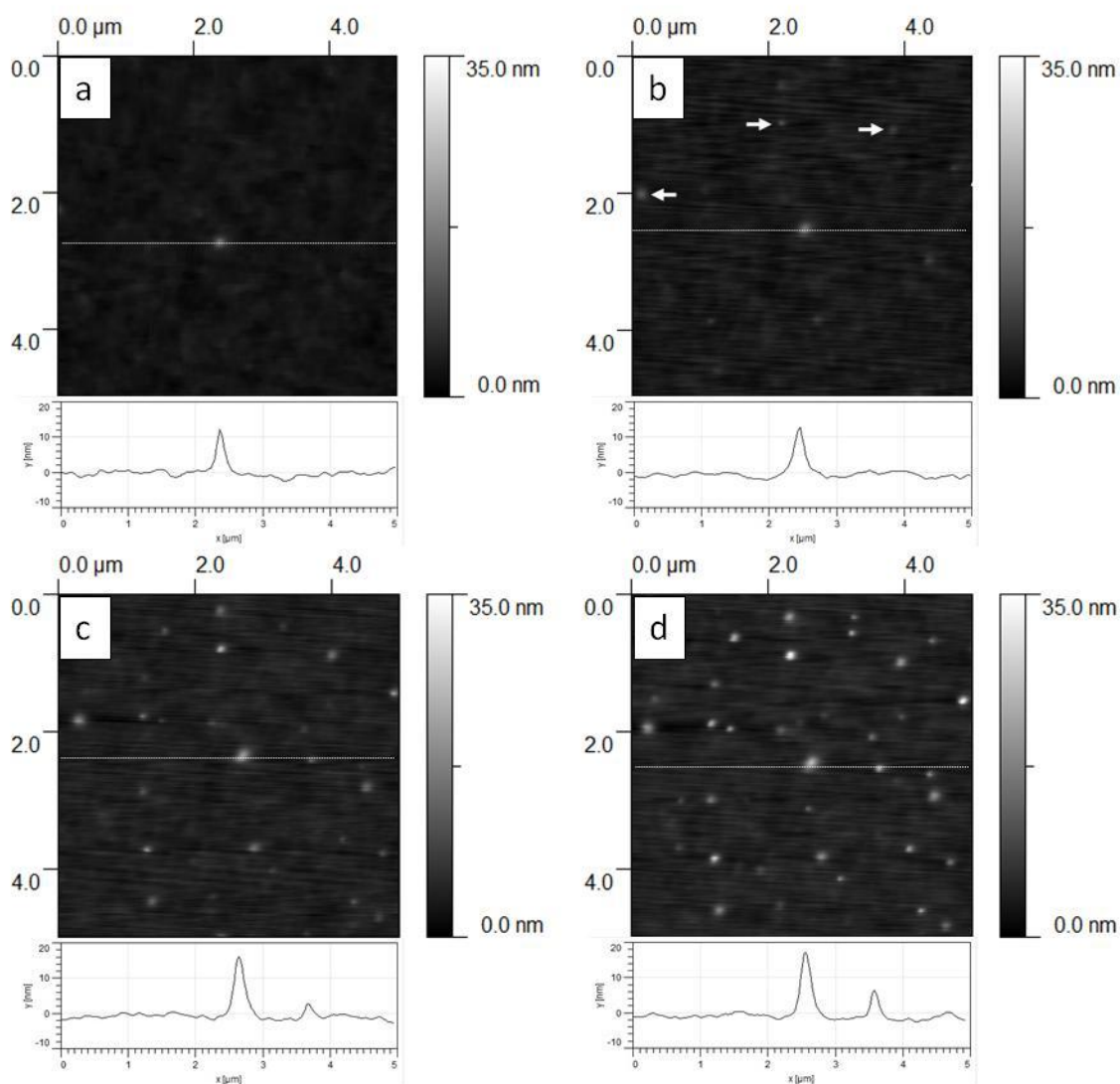


Figure 2.6 Time-lapse AFM images of a nanocomposite film after (a) 30, (b) 40, (c) 50, and (d) 60 minutes of drying in the air at the room temperature. Images show AgCl crystals, as indicated by the arrows, appear and grow on the film surface with time. Z-profile of the images shows that the height of the crystal at the center of the image continues to grow while other new crystals appear on the surface.

Chapter 3

Controlling Interconnected Silver Network Structure in Sol-Gel Nanocomposite via Shrinkage-induced Stress

Chi-Kai Chiu, Tsan-Yao Chen, and Tzy-Jiun M. Luo

Department of Materials Science and Engineering
North Carolina State University, Raleigh, NC 27606

Abstract

An interconnected silver network of granular layers with each layer about 100 nm thick is spontaneously formed inside a silica matrix when a sol-gel sample containing silver ion and poly(ethylene glycol) is dried and heat-treated. The minimum grain size of the silver structure is $\sim 15 \mu\text{m}$ and the density of the silver structure is related to the drying rate, which can be controlled by either drying temperature or vacuum drying time. It is found that the shrinkage-induced stress during the drying process results in microcracks where the crack surfaces serve as a 3-D template for silver to develop into interconnected network when the sample is annealed at $160 \text{ }^\circ\text{C}$. The ability to control the density of microcracks and utilize the microcracks as silver template suggests that this method can be utilized to (1) create interconnected silver network of desired density in silica materials, (2) visualize the microcracks of sol-gel materials, and (3) reinforce and repair the defects after microcracks have occurred.

3.1 Introduction

Materials synthesized via solution route sol-gel method are suitable for applications that rely on selectivity in diffusion,¹ size exclusion and filtration,² and encapsulation^{3,4} because of their intrinsic nanoporous structures. These pore structures that occur spontaneously during the gelation reaction are highly interconnected. Many literatures have reported on how pore diameters, pore structures, and pore volumes can be controlled.^{5,6} However, using these nanoscale pores as the template to produce secondary interconnected structures has been difficult due to that limited diffusion and the existing defects usually result in uneven distribution. We have reported that by incorporating low molecular weight poly(ethylene glycol) (PEG), silver nanoparticles and silver chloride nanoparticles inside the pores of sol-gel materials remain mobile and they are able to transport to the surface when the sol-gel material is under shrinkage-induced stress.⁷ It is known that silica materials synthesized by sol-gel method tend to shrink during drying. Solvent evaporation causes the structure of sol-gel materials to collapse and such shrinkage often induce stress, resulting in cracks. This is particularly common on films made via sol-gel processes as cracks are often thickness-dependent.⁸ Here we demonstrate that the microcracks also occur during the drying of a monolithic sol-gel sample and such microcrack surfaces can be utilized as the template to form interconnected silver structures (Figure 3.1a). We also show that the density of silver structure is related to the volume shrinkage rate in the drying process while the density is not related to the final annealing stage where the reductive polymer environment facilitate the

formation of interconnected silver network without causing the sample to disintegrate (Figure 3.1b).

3.2 Experimental procedures

3.2.1 Nanocomposite synthesis

The monolith of sol-gel samples that contained metal ions and poly(ethylene glycol) (PEG-300, MW = 300, Fluka) were synthesized using sol-gel method⁷ followed by drying and solid-state polyol process. All samples were prepared by mixing appropriate amount of the following three stock solutions. Solution 1 was prepared by dissolving 2.5 wt% polyvinylpyrrolidone (PVP, MW ~ 36,000, Sigma-Aldrich) in PEG-300; Solution 2 contains 0.3 M silver nitrate solution in deionized water. Finally, solution 3 containing 15.2 ml of tetramethylorthosilicate (TMOS 98%, Sigma-Aldrich), 80 μL of 0.5 N HCl, and 3.6 ml of deionized water was prepared according to the reported procedure,⁷ All mixing processes were performed at 0 $^{\circ}\text{C}$ in an ice bath. In the first step, 40 μL of solution 1 was mixed with 600 μL of solution 2 and stirred for 30 sec. After adding 300 μL of solution 3 with additional stirring for 30 sec, the mixtures were transferred to 10 \times 25 \times 3 mm polyacrylate cuvettes until gelation was completed (Wet gel, Figure 3.1a). Then, the samples were aged for 5 days at room temperature in the cuvettes (Aged gel, Figure 3.1a). The resulting monolithic samples were transferred from cuvettes to petri dishes and dried under various conditions. At the drying stage, the samples became semi-transparent monoliths. Upon exposing to light, the monolithic samples turned dark-brownish within hours. For vacuum drying samples, the

monoliths were transferred into desiccators then vacuumed under 0.1 torr for 1, 3, and 9 hours, respectively. For oven heating samples, the monoliths were respectively treated in Isotemp oven at 40, 60, 80 °C for 4 hours. One set of samples was placed in 40 °C oven for additional 48 hours (Dried gel, Figure 3.1a). The samples shrank to smaller dimensions according to different treatments. To induce silver reduction reaction and complete the metallization, all dry samples were heat-treated at 160 °C in the Isotemp oven for 3 hours, during which the dark-brownish monolith became silver metallic (Annealed gel, Figure 3.1a).

3.2.2 Micro-hardness, fragment size analysis, bulk resistivity, and cross-section analysis

After drying in different temperatures, the hardness value of the dried gels was measured by Buehler MicrometII (Lake Bluff, IL, USA) Vickers hardness tester using a 10 g load cell and a loading time of 15 sec. Five hardness values were measured for each sample. Analysis of fragment size, bulk resistivity, and cross-sectional imaging were performed on the 160 °C annealed gels. To analyze the fragment size, samples were broken by force into small particulates to reveal the silver color covered on the particle surface. The Image-J software was utilized to determine the feret's diameter of each fragment and each histogram was determined for each sample. The bulk-resistivity of composites was measured using Signatone four-point probe system consisting of a Keithaly S220 current source and a s2000 multimeter. Five data points were acquired for each sample. The cross-sectional images of monolith were prepared by first fixing monolith samples in epoxy resin followed by cutting with a diamond saw. Then the surfaces were polished using sandpapers of 600 and 1200 grits

size. Scanning electron microscopy images were taken on Hitachi S3200 SEM and the samples were imaged after sputtering additional metallic coating. The Oxford Isis energy dispersive X-ray spectrometer system attached on the SEM was used to identify the characteristic X-ray emission of the elements at surface areas using an accelerated voltage at 20 kV.

3.2.3 Determination of silver network density

The density of silver network on the cross-sectional images of the annealed samples was determined using ASTM standard E112-96 method (i.e., the standard method for average grain size). For each image of 685 μm x 508 μm , five horizontal lines of equal length separated by equal space were placed on the image. The numbers of intersects per 100 μm length where the silver network and the drawing line overlap are determined and then converted to grain size. Four images were analyzed for each sample.

3.3 Results and discussion

The general procedure for creating interconnected silver network in sol-gel nanocomposites includes preparation of wet gels, followed by aging and drying to form xerogels, then annealing heat-treatment at 160 $^{\circ}\text{C}$. The drying step was carried out by heat treatment at various temperatures (40 ~ 80 $^{\circ}\text{C}$) to achieve various degrees of drying states prior to the final annealing step at 160 $^{\circ}\text{C}$. During the annealing treatment, black samples became silver reflective color, indicating metallic silver layers have been produced. We have

previously reported that interconnected silver layers appear on both surface and internal space of sol-gel materials and their interconnectivity is related to the amount of polymer in the samples.⁷ Here, the sample dimension at each stage is shown in order to evaluate the degree of drying for the drying process (Figure 3.2). All aged gels retained 85% of the original size of wet gel volume and respectively shrank to 78%, 72%, and 61% of the wet gel size when drying for 4 hours at 40 °C, 60 °C, and 80 °C. The final size after annealing is ~55% of the wet gel and this value is independent of the drying process. Therefore the remaining dimension at ~55% is considered to be stable and fully dry. Without annealing, additional heat treatment at 40 °C for 2 days after 80 °C drying process was required to achieve this value at ~55%. After annealing treatment the volume of sample did not change and the silver sample was not disintegrated.

To determine the effect of drying process on the xerogel and silver network density, two drying processes were performed: isothermal vacuum drying and oven drying at various temperatures. The pictures of the resulting samples under vacuum drying and oven drying are shown in Figure 3.3a and 3.3b, respectively. Similar to the oven-dried samples, vacuum-dried samples also shrank with their size reduction proportional to the treating time and reached ~58% of the original size after 9 hours of vacuum drying. After annealing at 160 °C, the exterior surface of all samples was typically covered by a silver layer (Figure 3.3c), which has been confirmed by X-ray diffraction to be silver crystalline structure.⁷ To determine the density of silver network, the interior silver structure was revealed by breaking

the samples with force to expose the surface of granular structure (Figure 3.3d). Pictures of the broken pieces were later analyzed using Image-J software to determine the average Feret's diameter (Figure 3.3e and 3.3f). Both vacuum and oven drying processes show similar effects on the size of particulates, indicating temperature alone is not the direct factor for the size reduction of granular structure. We also found that the size of individual silver particles created during the annealing step is only dependent on the drying process but not the annealing process. Figure 3.3e show the average Feret's diameter decreases with both vacuum drying time and oven-drying temperature. For example, the minimum Feret's diameter reaches ~1.4 mm after 9 hours of vacuum drying. The same diameter can be achieved by heat-treatment although additional 2 days treatment at 40 °C is required. In general, vacuum drying is a more effective drying process, but rapid drying tends to damage the samples (Figure 3.3a). Considering the Feret's diameter is dependent on the drying process, we postulate the Feret's diameter of the granular structure must be related to the shrinkage of the sample. Hence, the diameter of granular structure is a function of the size reduction during the drying stage. However, the diameter is not related to the annealing stage. According to Figure 3.2, the size of a 40 °C oven-dried sample was reduced by ~30% during the annealing process, but the Feret's diameter only reduced to ~ 3.05 mm. In general, shrinkage of sol-gel materials results in lower porosity, which should increase the overall strength of the material. On the other hand, shrinkage also induces residual stress, which can be estimated by hardness measurement.

It is well known that the state of surface cracks around the corners of a Vickers pyramid indenter reveal the fracture toughness and surface stresses of materials.^{9, 10} The procedure is based on the principle of indentation fracture where the value of microcracking around hardness impressions provides a measure of resistance to crack extension. Measurement of crack size on surfaces of different samples can be estimated to yield information on the residual stress.¹¹ Here, the Vickers hardness of the dried gels and the corresponding stress values are shown in Figure 3.4a. The stress increases from 0.39 MPa to 15.66 MPa when the drying temperature increases from 40 °C to 80 °C. The stress reaches maximum of 28 MPa when additional 2 days of 40 °C treatment was performed after 80 °C drying process. The stress correlates well with the Feret's diameter of the annealed samples. In addition to the density of silver network structures, the actual connectivity of silver network of the annealed monoliths was furthered evaluated using bulk electric resistivity (Figure 3.4b). The bulk resistivity values decrease 10 times as the drying temperature increased from 40 °C to 80 °C, which confirms the higher interconnectivity of silver structures resulted from the higher shrinkage rate during drying process. It is interesting to note that the bulk resistivity of the annealed sample only changes from 6.54×10^{-3} to 5.04×10^{-3} ohm-cm when additional 2-days drying treatment at 40 °C was performed. The small decrease in the resistivity between two samples shows that the minimum threshold for good conductivity has been reached when the diameter of granular structure is ~ 2.0 mm.

We consider the shrinkage of sol-gel sample should have an effect similar to the rapid cooling process performed at glass tempering, which induces surface compressive stress to prevent the propagation of surface defects. The surface compressive stress and the tensile stress inside the bulk after tempering process increase the fracture toughness of glasses. Such surface compressive strain has been shown to generate tiny cracks on the surface,¹² which tends to result in small broken pieces due to the intervening release of stress around the microcracks.¹³ This phenomenon is similar to our drying process when various drying temperatures were used. In addition, high cooling rate during glass tempering could also induce the growth of small cracks into large ones.¹⁴

The volume shrinkage of the monoliths is the result of pore collapsing, which also induces the residual strain. Although all samples eventually shrank to the same size after annealing process, only the shrinkage at the drying process contributes to the stress accumulation in the samples. The presence of microcracks induced by residual stress was confirmed by examining the cross-sectional area of the sample (Figure 3.5a). Although microcracks appear as 2D bright fine lines on the image, these defects are in fact 3D surface defects. Depending on the orientation of the crack surfaces, when they are about parallel to the cross-sectional plane, defect surfaces of silver color are visible on the image (Figure 3.5a). The density of macro-size cracks also increases with the density of microcracks (data not shown). When an external force is applied to the monolith, fracture most likely follows the

surface of macrocracks (Figure 3.5b) and result in small fragments covered with silver (Figure 3.3d).

The propagation of cracks within sol-gel monolith during drying and annealing processes has been observed before.¹⁵⁻¹⁸ During the drying process, the volume of sol-gel decreases due to large capillary forces from solvent vaporization and additional polycondensation reaction. According to Gibbs-Kelvin equation, different shrinkage between the interior and exterior of a drying sol-gel sample may build up stress^{19, 20}. If the drying rate is increased, cracks will develop when it reaches to a critical value. Thus, when solvent evaporation rate increases, the interior tensile stress and the probability of cracking increase. Such stress has been shown to be as high as 100 MPa.¹⁹ These microscopic cracks occasionally merge together, resulting in macroscopic cracks and monolith disintegration. When annealing at 160 °C, few new cracks developed possibly due to the presence of more ductile silver phase. We have confirmed on SEM that both micro-size and macro-size cracks are present on cross-sectional surface (Figure 3.5b). Due to large void spaces at the macrocrack sites, silver layer appears to be thicker at the crack surfaces.

The proposed mechanism of silver network is shown in Figure 3.1b. Shrinking of samples during drying process built up internal stress and generated network of microcracks. In the mean time, the stress also forced the polymer in pore structures to migrate to the crack surfaces and open areas (i.e., the defect site and exterior surface). Upon heat-treated at

160 °C, the polymer turned into an effective reducing agent and facilitated the nucleation and growth of silver at the crack surfaces where exhibits high surface energy and low activation energy for silver to nucleate and grow. The formation of silver inclusion should increase the internal stress around the surface between silver and the matrix and caused the internal crack surfaces to propagate,^{21, 22} thus the cracks grew until they interconnected. In general, the possibility of fracture at this point could be high due to high stresses and low strain tolerance of the sol-gel materials. The reason our samples did not disintegrate because more ductile silver network reduce the overall brittleness and eventually increase the toughness of the samples.

The interconnectivity of the silver network explains why the bulk electrical resistivity of the sample decreases when the crack density increases. The thickness of the silver layer at the microcracks was estimated on SEM to be around 100 nm and the EDX analysis confirmed the presence of silver element on these defect areas (Figure 3.5b inset). The density of silver network resulted from microcracks was estimated using the cross-sectional surface of annealed gels. When the sample was dried at 40 °C, the average grain size (i.e., spacing) of the silver network in the annealed sample was 27 μm. The size decreased respectively to 20 and 17 μm when the drying temperatures were 60 °C and 80 °C (Figure 3.5c). Additional 2-days heat treatment at 40 °C after drying at 80 °C further decreased the grain size to 15 μm. Therefore we conclude that 15 μm is the minimum feature size of the

silver network that can be produced naturally from drying and annealing of the sol-gel materials.

3.4 Conclusion

In summary, synthesis of interconnected silver structures based on the presence of defects (i.e., microcracks) within sol-gel nanocomposite was reported. The interconnectivity density of silver covered area is related to either drying temperature or vacuum drying time carried out during the drying step while the density is not related to the annealing treatment when the metallization actually occurs. The minimum grain size of silver network was measured to be $\sim 15 \mu\text{m}$. In summary, our method can be utilized to (1) create interconnected silver network with controllable density in silica materials, (2) visualize the defects of sol-gel material, and (3) reinforce and repair the defects after microcracks have occurred.

3.5 References

1. N. Koone, Y. Shao, T. W. Zerda, *J. Phys. Chem.* 1995, 99, 16976.
2. S. Benfer, U. Popp, H. Richter, C. Siewert, G. Tomandl, *Separation and Purification Technology* 2001, 22-3, 231.
3. B. C. Dave, B. Dunn, J. S. Valentine, J. I. Zink, *Anal. Chem.* 1994, 66, A1120.
4. C. Sanchez, B. Julian, P. Belleville, M. Popall, *J. Mater. Chem.* 2005, 15, 3559.
5. C. J. Brinker, R. Sehgal, S. L. Hietala, R. Deshpande, D. M. Smith, D. Loy, C. S. Ashley, *J. Membrane Sci.* 1994, 94, 85.

6. Y. F. Lu, G. Z. Cao, R. P. Kale, S. Prabakar, G. P. Lopez, C. J. Brinker, *Chem. Mat.* 1999, 11, 1223.
7. T. Y. Chen, C. K. Chiu, Y. J. Choi, T. J. M. Luo, T. L. Lin, *J. Mater. Sci.* 2012, In press.
8. M. Bockmeyer, P. Loebmann, *Thin Solid Films* 2007, 515, 5212.
9. D. B. Marshall, B. R. Lawn, *J. Am. Ceram. Soc.* 1977, 60, 86.
10. G. R. Anstis, P. Chantikul, B. R. Lawn, D. B. Marshall, *J. Am. Ceram. Soc.* 1981, 64, 533.
11. J. J. Swab, J. C. LaSalvia, *Applied Ceramic Technology* 2011, I-6.
12. J. M. Barsom, *J. Am. Ceram. Soc.* 1968, 51, 75.
13. R. Gardon, *J. Am. Ceram. Soc.* 1978, 61, 143.
14. Pavlushk.Nm, Silvestr.Si, V. M. Firsov, V. D. Kazakov, *J. Mater. Sci.* 1969, 4, 479.
15. G. W. Scherer, *J. Non-Cryst. Solids* 1992, 147, 363.
16. T. Kawaguchi, H. Hishikura, J. Iura, *J. Non-Cryst. Solids* 1988, 100, 220.
17. H. Murata, D. E. Meyers, F. Kirkbir, S. R. Chaudhuri, A. Sarkar, *J. Sol-Gel Sci. Technol.* 1997, 8, 397.
18. F. Kirkbir, H. Murata, D. Meyers, S. R. Chaudhuri, A. Sarkar, *J. Sol-Gel Sci. Technol.* 1996, 6, 203.
19. G. W. S. Jeffrey Brinker, *Sol-gel science*, Academic Press, New York 1989.
20. L. L. Hench, M. J. R. Wilson, *J. Non-Cryst. Solids* 1990, 121, 234.
21. J. Selsing, *J. Am. Ceram. Soc.* 1961, 44, 419.
22. F. F. Lange, M. Metcalf, *J. Am. Ceram. Soc.* 1983, 66, 398.

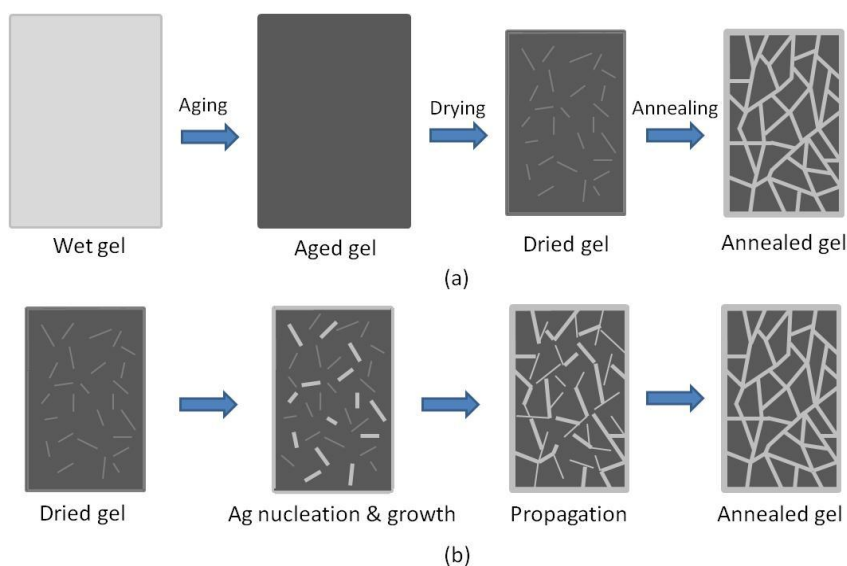


Figure 3.1 (a) A stepwise procedure for producing interconnected silver network within a nanocomposite sample includes aging, drying, and annealing at 160 °C, each of which respectively results in aged gel, dried gel, and finally the annealed gel. (b) A proposed mechanism explains the development of silver network during the annealing of a dried gel.

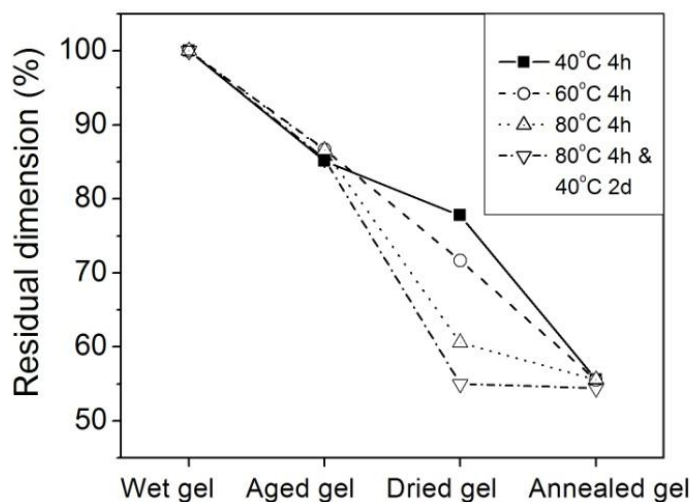


Figure 3.2 Evolution of the sample dimension during each treatment stage. The dimension of aged gels was 85% of the wet gel size and it reduced to 78%, 72%, and 61% after drying for 4 hrs at 40 °C, 60 °C, 80 °C, respectively. The dimension decreased to 55% when additional 2 days heat treatment at 40 °C was performed. The size of all annealed samples reduced to 55% regardless of the drying temperature prior to the annealing.

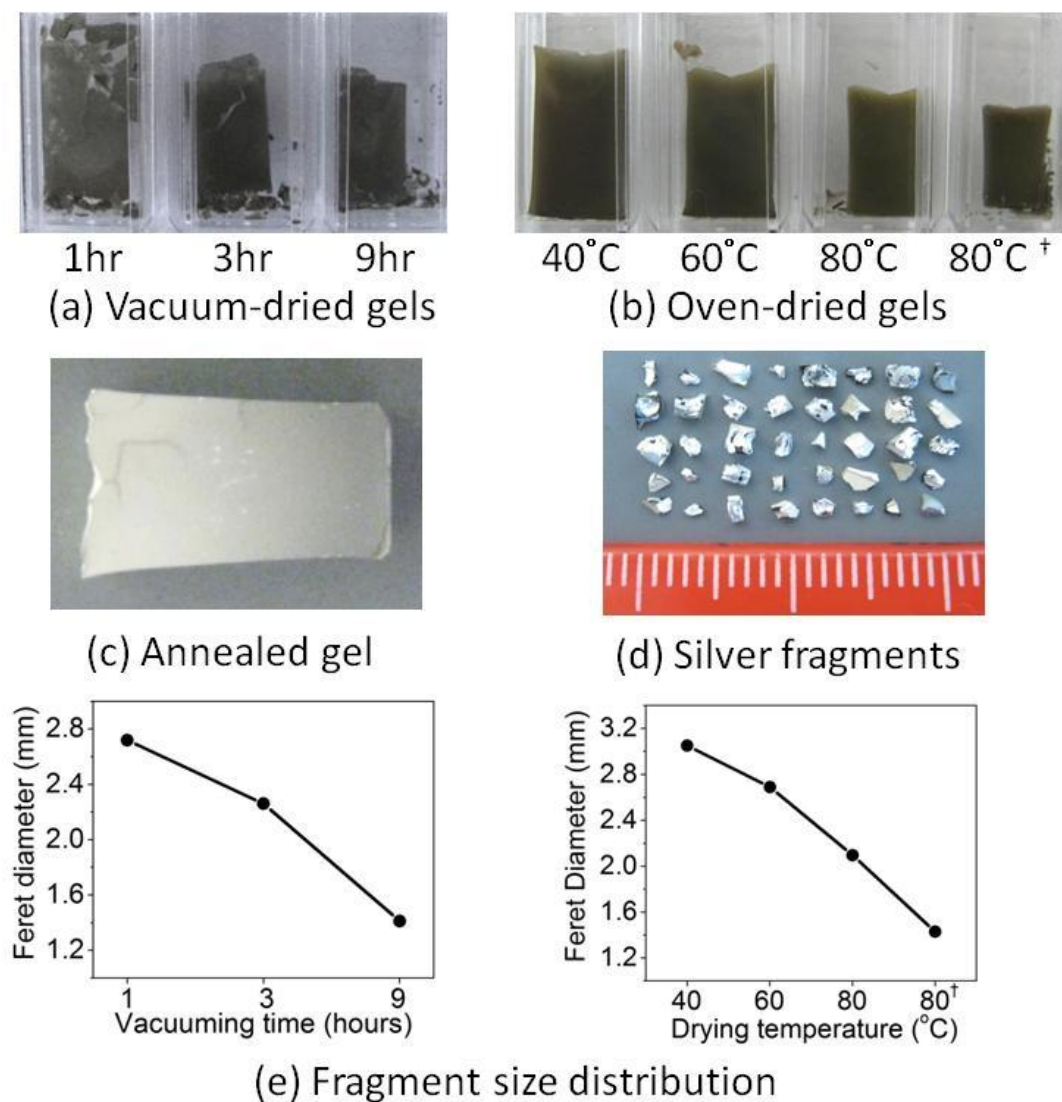


Figure 3.3 The density of silver network was evaluated by measuring the size of individual fragments after breaking the annealed samples by force. Dried gels were produced via (a) vacuum drying and (b) oven drying. After annealing at 160 °C, the annealed gel typically has a silver metallic appearance (c) and its macroscopic silver network structures are revealed by (d) individual fragments. The size of the pieces decreases with (e) vacuum time and (f) drying temperature during the drying process. (†additional treatment at 40 °C for 48 hours)

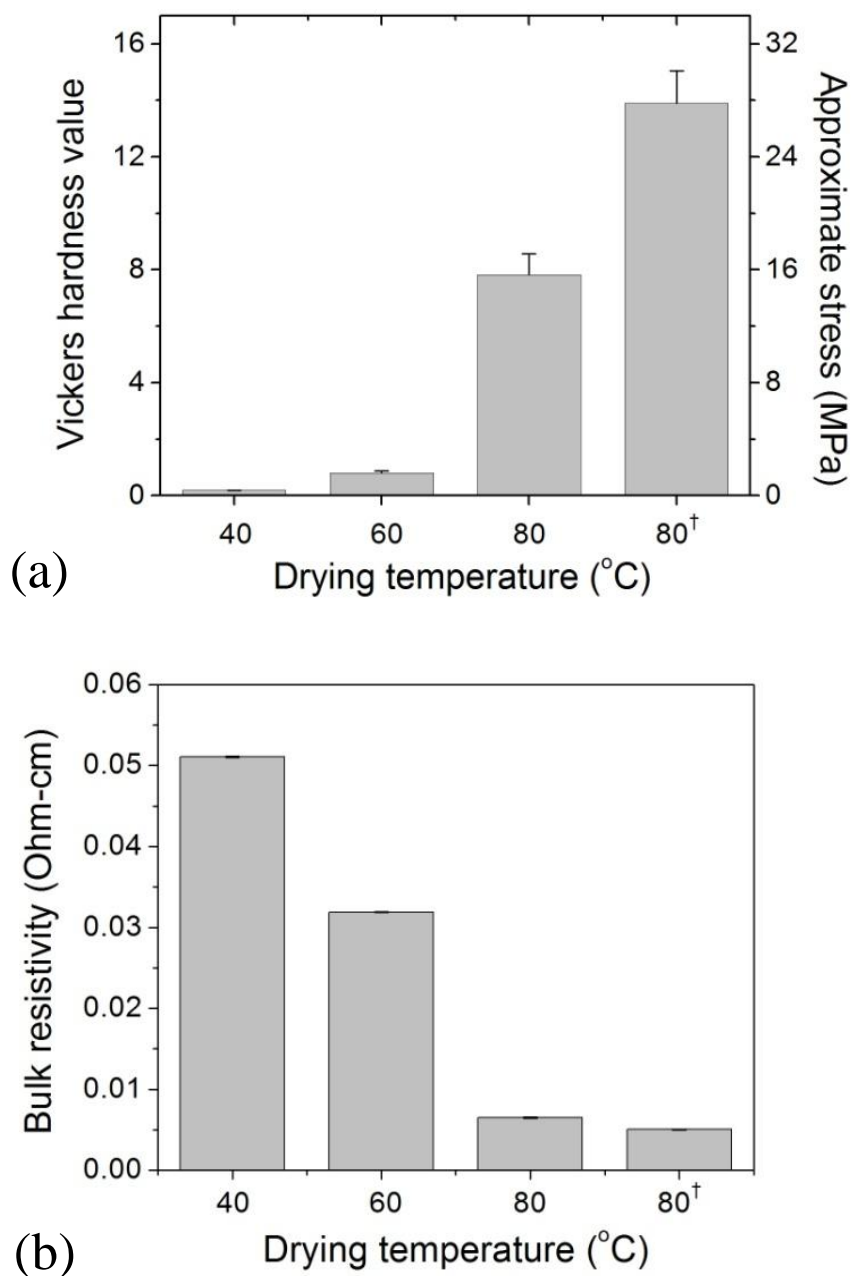


Figure 3.4 (a) Hardness of the dried gels on Vickers scale after respectively drying the samples for 4 hrs at 40 °C, 60 °C, 80 °C, and 80 °C with additional 40 °C treatment for 2 days (denoted by 80[†]). The estimated stress was converted from the hardness and shown on the right. (b) Bulk electric resistivity of the annealed gels. The gels were annealed to produce silver network after the 4 hrs drying treatment at 40 °C, 60 °C, 80 °C, and 80 °C with additional 40 °C treatment for 2 days (denoted by 80[†]).

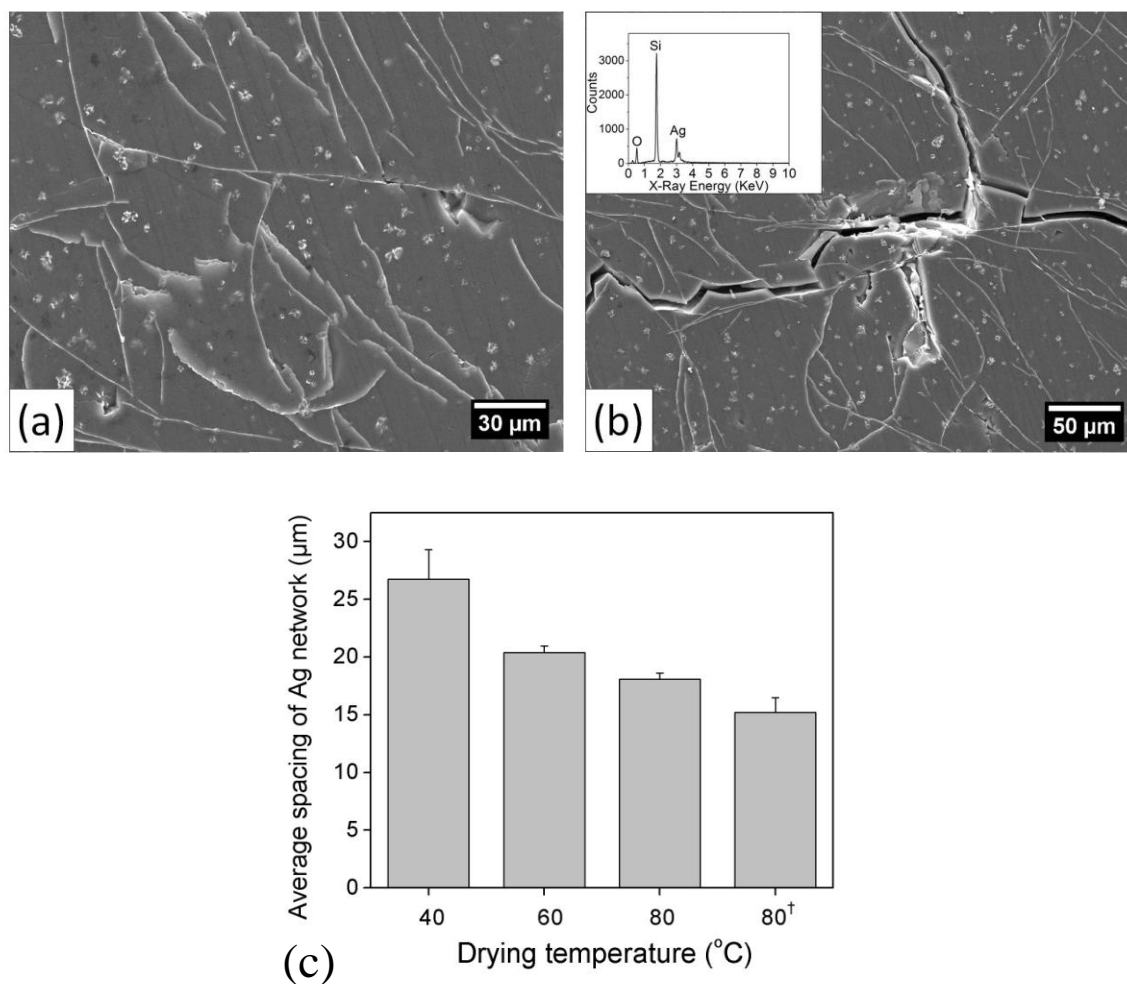


Figure 3.5 SEM images of cross-sectional area of the annealed gel, which has been oven-dried at 80 $^{\circ}\text{C}$ for 4 hrs followed by annealing at 160 $^{\circ}\text{C}$. (a) White fine lines and dots depict the silver network structures and aggregated silver nanoparticles. (b) Silver layer also appears at the fracture surface of macrocracks. The inset is the energy-dispersive X-ray spectroscopy of the surface near a macrocrack. The presence of silver element has been confirmed. (c) Average grain size of the silver network inside the annealed gels vs. various drying temperatures carried out at the drying stage. The average grain size reaches 15 μm when the oven-drying was performed at 80 $^{\circ}\text{C}$ followed by additional 40 $^{\circ}\text{C}$ treatment for 2 days.

Chapter 4

Synthesis of Porous Silver Metals by Ceramic Processing of Sol-Gel Particles

Chi-Kai Chiu, Tzy-Jiun M. Luo

Department of Materials Science and Engineering
North Carolina State University, Raleigh, NC 27606

Abstract

Porous metallic silver has been successfully produced by ceramic processing of sol-gel particles, whose procedure includes grinding a sol-gel synthesized silica into powder, powder-pressing, annealing at 600 °C, and silica etching in HF. Silica powder of 2 μm and 73 μm were produced and the pore size of porous silver is related to the particle size and pressing pressure. It is found that the interconnected silver network was formed after annealing, which has been proved using SEM, bulk resistivity, and 3-point bending test. The formation of interconnected silver network within powder-pressed sample is the key to the successful synthesis of the porous metals.

4.1 Introduction

Due to high specific surface area, low density, and intrinsic electrical conductivity, nanoporous metallic materials are ideal for power generation, filtration, deionization, and sensing. It has also been reported that nanoporous metals may show higher toughness and yield strength than the bulk materials because the grain size is limited by the nanostructure. To create such materials, methods include infiltrated deposition in inverted opal structures, chemical reduction with sacrificial templates and porous templates, selective etching, self-assembly, and hot-pressing. Currently, to create bulk porous structure at large quantity requires multiple steps of industry processes, which most utilize gas foaming^{1, 2} and melt filling^{3, 4} methods. Gas foaming is a non-homogeneous procedure while melt filling method is only suitable to create samples of large pore size (100-1000 μm). Hence, there is still a need to identify an economical and rapid approach for creating bulk porous samples particularly with desired geometry.

We have been investigating silver interconnected structures within sol-gel nanocomposites and exploring how to control their structures at nanoscopic to microscopic scales. Here, we report a simple and highly scalable approach for creating porous metals in bulk with a possibility to produce them in desired geometry. The starting material is a dry sol-gel produced silica sample containing 25 wt% silver nitrate. The procedure begins with grinding to produce silica powder, pressing into desired size and geometry under pressure, and then annealing to harden followed by etching in solution to give porous structures

(Figure 4.1). This approach combines the advantages of top-down and bottom-up methods to create porous structures of controllable pore size and connectivity as it utilizes the diffusivity of silver in the nanoporous silica when reduction of silver nitrate is carried out at the annealing step. Since the formation of interconnected silver is critical in this process, the composition of sol-gel silica, the size of milled silica powder, pressing pressure and heat treatment temperature should be controlled. Therefore, we report here how pore size and interconnectivity of the metal samples to be controlled using the size of silica powder (e.g., 2~73 μm) and the pressing pressure (100~400 MPa).

4.2 Experimental procedures

TMOS-sol was prepared by mixing 3.6 mL of deionized water and 15.2 mL of tetramethyl orthosilicate (TMOS). Upon adding 80 μL of 0.5 N HCl, the mixture was immediately placed in an ice bath and vigorously stirred for 2 min until the solution became clear and uniform. Then, the mixture was sonicated at room temperature for another 20 min. The stock solution was stored in the freezer for future preparation. To prepare silica sample containing silver, a solution of 1 M silver nitrate and the TMOS-sol were mixed at 4:1 (v/v) ratio. After stirring for 30 seconds, the mixture was transferred into cuvettes and aged at room temperature for 2 days. The mixture normally turned into gel-like solids after 6 hours. Later, the cuvette covers were removed, allowing the samples to dry at room temperature for another 4 days. The dry gels were briefly grinded and then dried at 50 $^{\circ}\text{C}$ for 2 days. The resulting samples that appeared to be white powder were further ground in a mortar with a

pestle for 5 min to derive the average particle size of 73 μm in diameter. The powder was stored in the dark for future use and was used to prepare all the samples in this study unless state otherwise. To prepare powder of 2 μm in diameter the grinding process should take longer than 50 min.

To form a compressed solid, 900 mg of the fine powder was transferred into a disk shape tungsten carbide mold. A carver press was placed on top of the sample and various pressures between 100 - 400 MPa was applied for 180 seconds using a laboratory press (Carver, Wabash, In). The compressed pellet was measured to be 7 - 13 mm in diameter and \sim 1 mm in thickness. Then, the sample was heat-treated at 600 $^{\circ}\text{C}$ in an oven for 90 min under a ramping rate of 20 $^{\circ}\text{C}/\text{min}$ from room temperature. The sample was remained in the oven and allowed to cool to room temperature for about 2 hours. Then, the sample was immersed in 10% hydrofluoric acid or 15 M sodium hydroxide solution for 120 min to remove the silica matrix. The resulting porous silver sample appeared to be silver color and should maintain its original shape with undetectable volume shrinkage.

4.3 Results and discussion

The surface of the silver sample is revealed on SEM images under 3 different magnifications. The porous structure appears to be through out the sample and the pores on the surface have uniform size all over the surface (Figure 4.2a). Pore space is interconnected and visible on Figure 4.2b. Pore size was estimated to be \sim 20 μm . Close examination on

SEM images reveals that the open pores are defined by the random arrangements of 1D silver aggregate (i.e., pore struts), which have irregular shape and interconnect in 3D space (Figure 4.2c). The surface of 1D silver struts is ragged and consists of many facets and small particles of various size $< 5 \mu\text{m}$. The thickness of individual 1D silver structures was estimated to be $\sim 10 \mu\text{m}$. The maximum size of aggregated silver structure is no more than $20 \mu\text{m}$. The ragged surface is formed due to the geometry and shape of void space between the compressed silica particles (Figure 4.2d). Because the silica powder was produced after the sol-gel silica sample was completely dry, it is expected that the individual powder particle created by grinding procedure and pressure pressing should create multiple facets instead of round and globular shape when fractures of ceramic particle occur.

To examine the effect of powder size on the pore structure of the samples, silica powder of much smaller diameter around $\sim 2 \mu\text{m}$ were produced and used. SEM images show that the pore size of such sample is $\sim 5 \mu\text{m}$ and the diameter of 1D interconnected struts is $\sim 2 \mu\text{m}$ (Figure 4.3a and 4.3b). Individual 1D silver aggregate are composed of individual silver particles about $1\sim 2 \mu\text{m}$ in diameter. In general, it is expected that the feature size of porous structure decreases with the particle size, but it is interesting to find that on both figure 4.2 and 4.3, the pore sizes of both samples are equal or smaller than the powder size. By studying annealed samples, we found that fracture of silica particles occurred during the pressure pressing and resulted in the reduction of powder size, as can be seen on the SEM image of annealed samples where small fractured particles are surrounding large particles (data not

shown here). The SEM images of annealed sample reveal created using 73 μm powder that the microstructure consists of large particles ($>10 \mu\text{m}$) and small particles ($<5 \mu\text{m}$). Both particles are smaller than the original powder size (73 μm), indicating deformation and compaction of the particles have occurred. Small void spaces and defects are found around the particles as both defect and void spaces serve as the template to form interconnected silver structures when annealing at 600 $^{\circ}\text{C}$. This explains why the high resolution SEM of silver structure surface reveals multiple facets, which represents typical fracture surfaces of brittle materials (i.e., dry silica). This observation also proves that the porous silver structures are the results of surface template where silver form in the void spaces and fractured surfaces between particles during annealing.

Because fracture density and void spaces of compressed particles are dependent of the pressing pressure, porous structures of the samples prepared from 73 μm powder under 100, 200, and 400 MPa pressures are shown on Figure 4.4. We found the 1D silver struts on the sample prepared under high pressure tend to have multiple facets while on the sample prepared under low pressing pressure has globular and round silver aggregates. The feature size of silver struts for samples prepared under 100, 200, and 400 MPa is 18 μm , 11 μm , and 6.5 μm , respectively. The large silver aggregate structures resulted from 100 MPa indicates larger void volume was produced at lower pressure. Fewer silica particles were crushed under 100 MPa and resulted in lower density. Although pore size may be different, the porosity of silver foam calculated from the theoretical density of silver decreased only

slightly from 89.0% at 100 MPa to 88.8% at 400 MPa, indicating the porosity remain constant in all three samples.

According to the TGA data, pure silver nitrate decomposes at 450 °C. Silver nitrate within the sol-gel matrix was found to decompose and reduce to metallic silver at 300 °C.^{5, 6} The release of oxygen radicals from the condensation reaction of silane may help to reduce silver. However, silver nitrate in our dry silica sample decomposed between 250 °C and 600 °C, according to our TGA results. Therefore, the reduction reaction of AgNO₃ was carried out at 600 °C. Above 400 °C, the thermionic decomposition of silver nitrate occurs while the diffusion and migration of silver nanoparticles are likely to occur at 600 °C. The weight percent of silver phases within Ag-silica composites increases to 40 wt% after annealing according to the TGA calculation. After annealing, SEM images show that silver phase surrounds large particles and fills out those void spaces (Figure 4.2d). In order to reduce surface free energy, silver tend to aggregate at void spaces at high annealing temperature. The result is larger silver structures. At the same time, sol-gel silica continues to shrink, reducing the sample size to 88 % of original volume. Later, silica can be removed with hydrofluoric acid or sodium hydroxide, leaving only interconnected silver structure with a strut size around 6.5-18 μm. EDXS was utilized to determine the composition of silver sample and only silver peak at 3.5 keV was found on the spectrum, indicating silica has been completely removed.

The strut size of porous network can be controlled by pressing pressure. The strut size decreases from 18 to 6.5 μm when pressure increases from 100 to 400 MPa (Figure 4.5a). As shown in the SEM images (Figure 4.4), the strut size decrease as the pressure increases. Low pressure results in larger void space between silica phases. Hence, density and pore size of the silver sponge can be easily controlled using pressing pressure. The reversed relation between pressing pressure and density of the silver sponge can be described using an empirical equation that it predicts that about 50-70% of the relative density can be derived after pressing.⁷ This phenomenon also serves as the proof that the void spaces between particles are the 3D template for silver. To further confirm the interconnected silver network was formed after annealing and its connectivity, the bulk electrical resistivity of annealed samples was measured. The results show resistivity decreases with the pressing pressure, which indicates the increase of interconnectivity density (Figure 4.5b). This confirms that the interconnected silver network was formed after annealing.

The stress-strain curve from the results of three-point bending test of annealed samples also provides the information on silver interconnectivity. After the formation of silver network structure within the compressed silica powder, both ductility and toughness of the annealed sample increase. Although the modulus is lower than the sample made of pure silica powder, the ultimate strength increases (Figure 4.6a). The ultimate strength increases by 64% from 11 MPa to 18 MPa (Figure 4.6b). Furthermore, this reinforced effect of silver network is significant, considering the porosity of the annealed sample with silver network is ~45%

compared to that of the one without silver network around $< 5\%$, which is the result of more ductile silver phase. SEM images confirm the elongation and distortion of silver structure at fracture surfaces. The overall toughness based on the stress-strain curve was determined to be 5.48 times higher. Although the nanoporous metals usually exhibit lower fracture toughness than the bulk metal due to the limited density of dislocations, it shows the reinforced effect when incorporating into the ceramic glass. Thus, combining its higher strength, the interconnected metal structure could be used as the reinforced phases for the ceramics produced from powder pressing and to replace the traditional polymers and ceramic phases.⁸

⁹ The interconnected structure also provides the isotropic reinforced effect all over the composites rather than only anisotropic effect of fiber reinforced composites.

4.4 Conclusion

We have successfully produced interconnected silver network inside powder-pressed silica and porous silver in bulk by etching the silica. The silica powder containing AgCl was ground from sol-gel synthesized solid. The milled silica particles do not have to be in spherical shape. Instead, silica powders of irregular shape with an average diameter of 2 and 73 μm produced from the grinding process were used and the efficient of packing can be enhanced by the pressing pressure. We have shown that the pore size of silver network is related to the final size of compressed particles and the presence of silver network after annealing, hence a metal-ceramic composite, significantly enhances the mechanical properties of powder-pressed ceramics.

4.5 References

1. Yu, C. J.; Eifert, H. H.; Banhart, J.; Baumeister, J., Metal foaming by a powder metallurgy method: Production, properties and applications. *Materials Research Innovations* 1998, 2, (3), 181-188.
2. Dunand, D. C., Processing of titanium foams. *Advanced Engineering Materials* 2004, 6, (6), 369-376.
3. Durian, D. J., Bubble-scale model of foam mechanics: Melting, nonlinear behavior, and avalanches. *Physical Review E* 1997, 55, (2), 1739-1751.
4. Davies, G. J.; Zhen, S., Metallic Foams - Their Production, Properties and Applications. *Journal of Materials Science* 1983, 18, (7), 1899-1911.
5. Huang, M. H.; Choudrey, A.; Yang, P. D., Ag nanowire formation within mesoporous silica. *Chemical Communications* 2000, (12), 1063-1064.
6. Cao, J. M.; Cao, Y. L.; Chang, X.; Zheng, M. B.; Liu, J. S.; Ji, H. M., Synthesis of silver nanoparticles within ordered CMK-3 mesoporous carbon. In *Nanoporous Materials Iv*, Elsevier Science Bv: Amsterdam, 2005; Vol. 156, pp 423-426.
7. Zheng, J.; Reed, J. S., Particle and Granule Parameters Affecting Compaction Efficiency in Dry Pressing. *Journal of the American Ceramic Society* 1988, 71, (11), C456-C458.
8. Rodeghiero, E. D.; Tse, O. K.; Chisaki, J.; Giannelis, E. P., Synthesis and Properties of Ni-Alpha-Al₂O₃ Composites Via Sol-Gel. *Materials Science and Engineering a-Structural Materials Properties Microstructure and Processing* 1995, 195, (1-2), 151-161.

9. Raj, R.; Thompson, L. R., Design of the Microstructural Scale for Optimum Toughening in Metallic Composites. *Acta Metallurgica Et Materialia* 1994, 42, (12), 4135-4142.

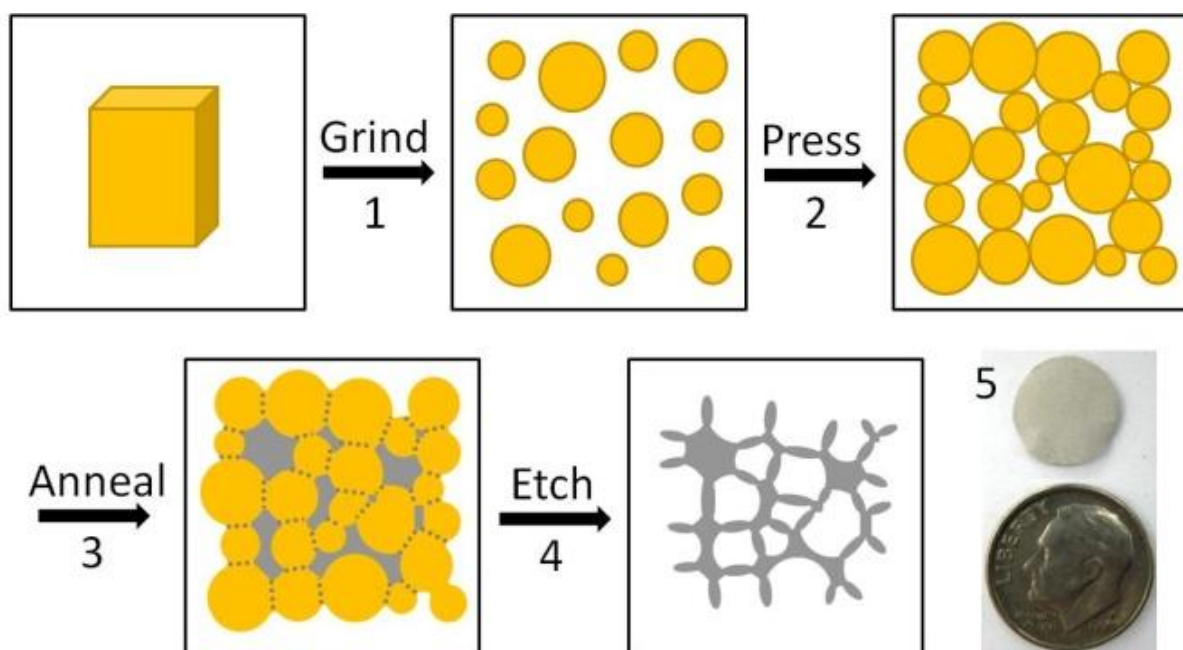


Figure 4.1 The step-by-step procedure for producing bulk porous silver from a dry sol-gel silica containing AgNO_3 includes (1) grinding, (2) press-forming, (3) annealing, and (4) etching in HF. The resulting solid is a silver color sample as shown on the photo.

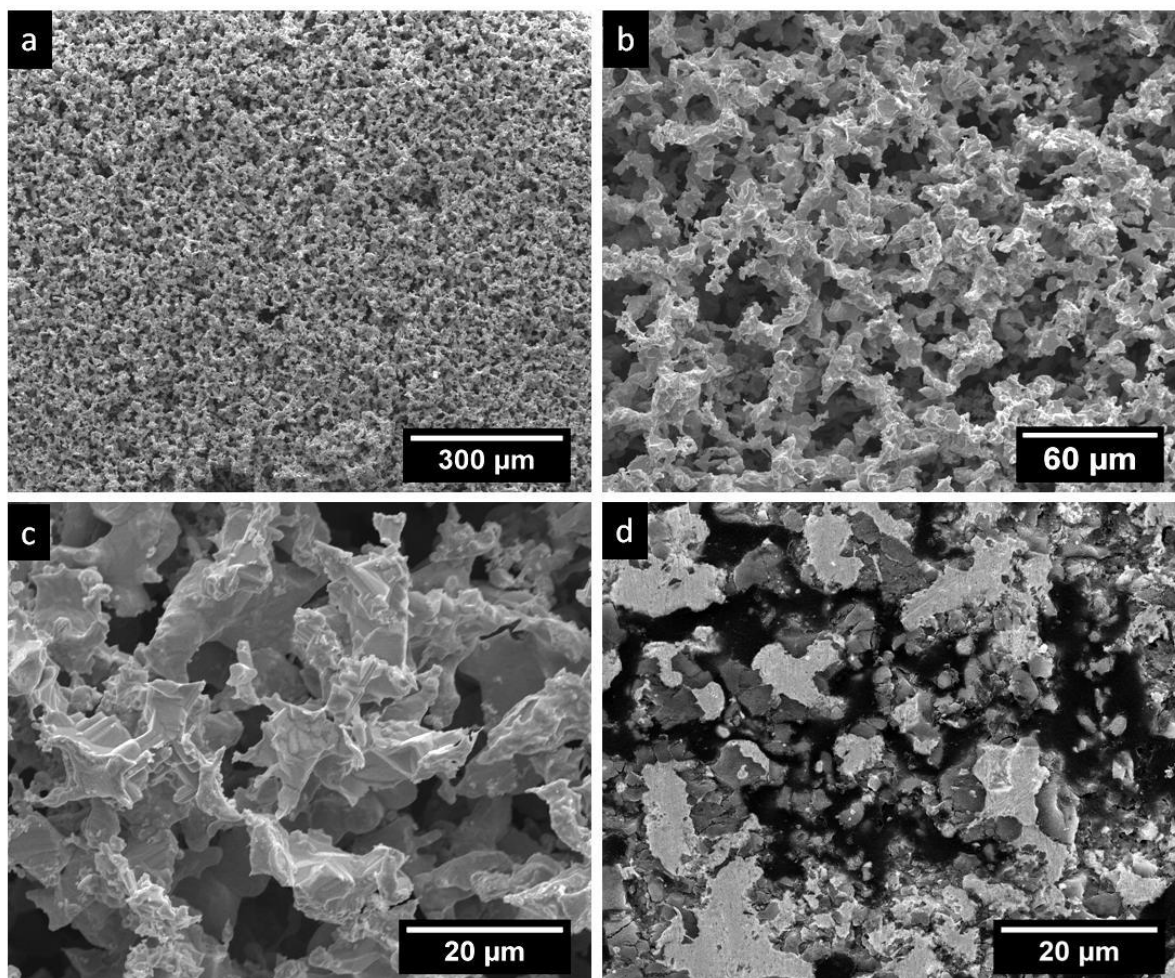


Figure 4.2 A uniform porous structure can be seen on the silver solid sample produced using 70 μm size powder at (a) 250x and (b) 500x magnifications. (c) Surface of the sample is magnified at 2,000x to reveal the open pores and strut surface structures. (d) Silver distribution on the surface of annealed sample prior to the etching step indicates that silver appear at the void spaces between silica particles.

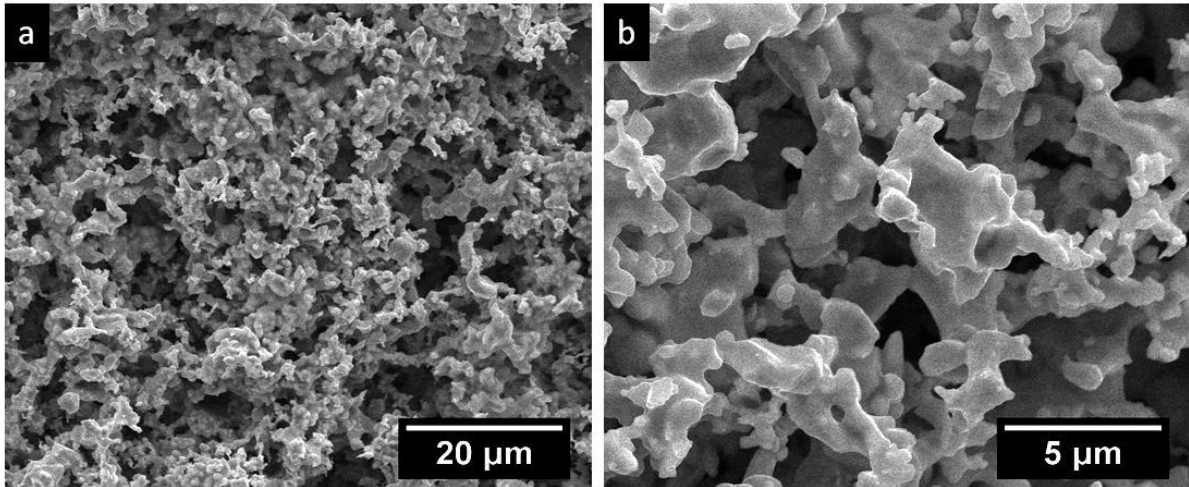


Figure 4.3 (a) SEM images of the silver metal made from powder of 2 μm in diameter reveal much smaller pore structures (2,000x). (b) High resolution image at 8,000x reveals the grain-like silver struts arranging in anisotropic order due to the packing of powder particles.

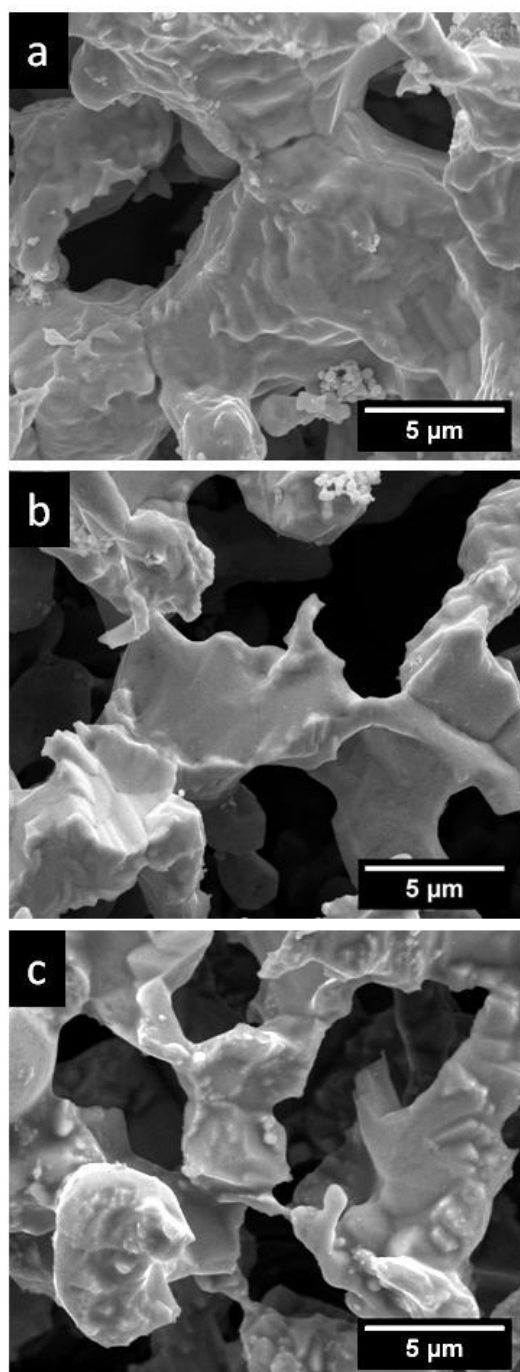


Figure 4.4 SEM images of three porous silver samples that were prepared respectively under (a) 100 MPa, (b) 200 MPa, and (c) 400 MPa, show that the size or pore struts decreases with the pressing pressure.

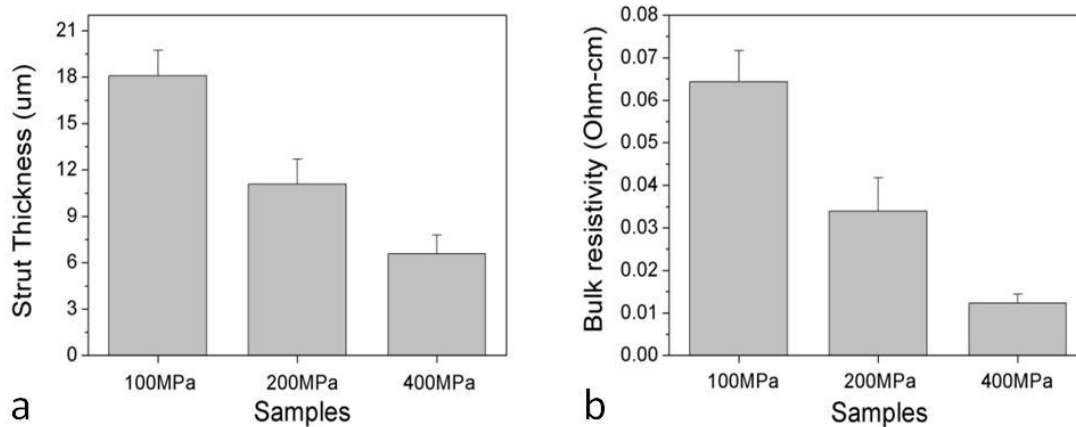


Figure 4.5 (a) The size of pore struts in silver sponge decreases with the pressing pressure. (b) The interconnectivity of silver network increases with the pressing pressure as revealed by the bulk resistivity of the annealed sample, which proves that silver network is formed after annealing.

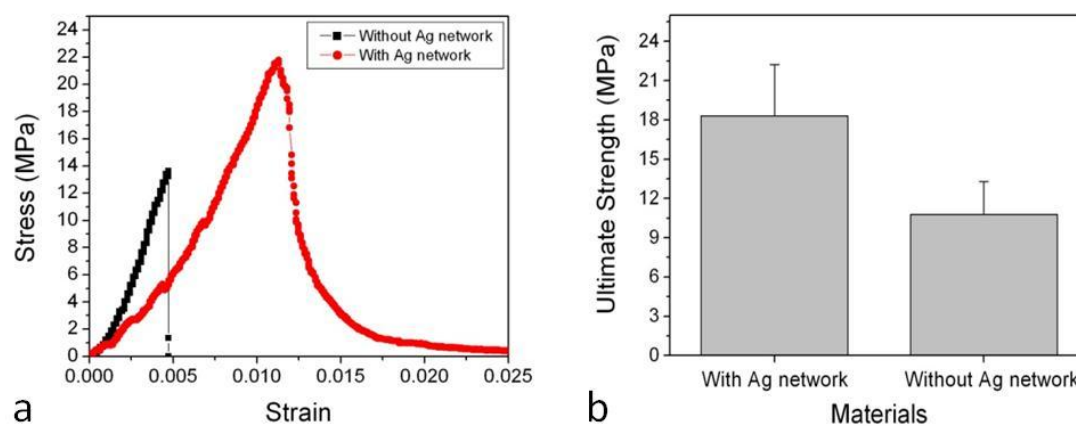


Figure 4.6 (a) Effect of silver on the stress-strain behavior of the annealed samples shows that silver phase contributes to the ductility of the annealed sample. The annealed sample without the silver phase appears to be brittle. (b) The ultimate strength of annealed samples with the presence of silver network is 64% higher than that of silica only.

Chapter 5

Self-Assembled Silver Nanoparticle Pattern Using Silane Treated Sol-gel Nanocomposites

Chi-Kai Chiu, Tzy-Jiun M. Luo

Department of Materials Science and Engineering
North Carolina State University, Raleigh, NC 27606

Abstract

We have demonstrated a simple but highly selective method for creating silver nanoparticles on patterned polymer-silica nanocomposite films. The deposition of nanoparticles on the nanocomposite film only occurs at the area that is thicker than 100 nm where enough concentrated Ag^+ could be migrated to the surface to nucleate and grow. This selectivity makes imprint patterning useful for this application as the removal or post-processing of the residual layer of the film is not needed. In the present study, (3-mercaptopropyl)trimethoxysilane (3-MTS) was added into polymer-silica nanocomposites as the silver absorption agent to form patterned arrays of nanoparticle. AFM and SEM were used to observe the structures of silver nanoparticle patterns. The EDX and UV-Vis spectrum were measured to investigate the formation of silver nanoparticles. Two methods at different temperatures are utilized to form nanoparticles patterns including decomposition and electroless deposition (ELD), respectively. The silver nanoparticles with average size of 100 - 120 nm and linear density of $2.6 - 3.4 \mu\text{m}^{-1}$ are synthesized at 400 - 600 °C treatments by decomposition. The 67 nm silver

nanoparticles with linear density of $5.65 \mu\text{m}^{-1}$ can be synthesized at room temperature by ELD. The strong affiliation of thiol groups of 3-MTS to silver was found critical to the selective growth of silver nanoparticles on the protruded areas, suggesting this simple approach have high potentials in industrial nano-imprint and nanotechnology applications.

5.1 Introduction

To fully utilize the properties of nanoparticles for applications in optics,^{1, 2} microelectronics,^{3, 4} sensors^{5, 6} and biomedicines,^{7, 8} patterned arrays of nanoparticles are often constructed. Recent studies have shown that an array of metal nanoparticles may overcome the diffraction limit and guide light in sub-wavelength regions, making it useful for optoelectronics and light emission applications.^{9, 10} However, synthesizing patterned arrays of nanoparticles only receives limited success and only two methods have been proposed to control the nanoparticles' position on solid substrates. First method, also known as the top-down method, utilizes electron beam to create patterns onto a uniform layer of nanoparticles or their precursors on substrates followed by a development step.^{11, 12} This technique can damage the nanoparticles and the feature size is limited by the theoretical limits of irradiation source and inherent materials. Second method, called bottom-up method, utilizes a monolayer of patterned molecule on the substrate as a template to guide the self-adsorption of nanoparticles from solution.^{13, 14} However, it does not yield high quality and good selectivity features because of the existence of the residual layers left by the imprint method.^{15, 16} These residual layers are usually removed at the following steps using either

chemical etching or plasma etching. The alternative method is self-assemble and in-situ growth of nanoparticles at patterned region on the solid surface.

We have reported that by incorporating low molecular weight poly(ethylene glycol) (PEG), silver nanoparticles and silver chloride nanocrystals inside the pores of sol-gel materials remain mobile and they are able to transport to the surface when the sol-gel material is under shrinkage-induced stress. The formation of silver and silver chloride nanoparticles on the surface suggests the possibility to self-assemble silver nanoparticle array patterns. Thus, how to control the deposition sites becomes the new task in the present study. Here, thiol chemical group within sol-gel nanocomposites was utilized to control the mobility of silver ions toward surface and thus vary the density of nanoparticles at different locations. Two processes were demonstrated to grow silver nanoparticles and they are heat treatment (Figure 5.1a) and electroless deposition (Figure 5.1b). Both processes consist of two steps 1. Formation of thiol containing pattern and 2. Deposition of silver nanoparticles (Figure 5.1). The thiol group is known for its strong affiliation to gold, silver and platinum atoms and has been utilized to produce self assembled monolayer.¹⁷⁻¹⁹ By limiting the mobility of silver ions within the sol-gel nanocomposites, the formation density of silver nanoparticles at selected areas can be controlled. The silver nanoparticle arrays exhibits well-defined pattern, highly selective nanoparticle deposition and tunable nanoparticle sizes regardless the thin residual layer. Thus, the fabrication method of Ag nanoparticle array described here can be

generalized to fabricate diverse arrays with various materials having controllable geometry and dimensions.

5.2 Materials and Methods

5.2.1 Preparation of stock solutions

TMOS-sol was prepared by mixing 3.6 mL deionized-water with 15.2 mL Tetramethyl orthosilicate (TMOS, $\text{Si}(\text{OCH}_3)_4$, 98%, Sigma-Aldrich). After adding 80 μL of 0.5 N HNO_3 , the mixture was transferred into ice bath immediately. During the vigorous stir for 2 min in ice bath, the solution became clear and uniform. Then, the mixture was sonicated for 20 min. The resulting solution should be colorless and particle free. PEG-sol was prepared by adding 3.6 mL DI-water into TMOS-sol and then adding 7.2 mL Poly(ethylene glycol) (PEG-300, MW=300, Sigma-Aldrich) into mixture. Methanol was removed from the sol by rotary evaporation (200 mbar reduced pressure, 45 $^\circ\text{C}$) for 35 minutes to get viscous PEG-sol.

5.2.2 Synthesis of patterned nanoparticle arrays

The CD-ROM pattern template was made by cutting a CD-ROM disc (Verbatim brand) into 10x10 mm size and the metal coating was peeled away using scotch tape. The template was sonicated subsequently in isopropyl alcohol (IPA) and methanol solution for 10 min to clean and remove the dye. After sonication, the template was dry by purging the air. The glass substrate was made by cutting glass slide (Fisher brand) into 10x10 mm size and then

cleaned subsequently in IPA and methanol for 10 min sonication. After drying by purging air, the glass substrate was plasma-treated for 2 min immediately before use.

Two procedures were employed to create sol-gel patterns and each requires different casting solution. For first method, two surfactant solutions used in the first procedure are (3-mercaptopropyl)trimethoxysilane solution (3-MTS, 0.1 M in methanol, Gelest) and polyvinylpyrrolidone solution (PVP, 0.1 M in methanol). A 40 μL of surfactant solution mixed with 600 μL of 1 M silver nitrate solution and agitated for 30 seconds. Then, a 200 μL of PEG-sol was added into the mixture and mixed for 30 seconds. (**note:** the PEG-sol should be warmed up to room temperature before using). For second method, 50 μL of ammonia water and 10 μL of 3-MTS solution were added into methanol instead of silver nitrate solution. Then, 200 μL of PEG-sol was added into solution and the mixture was mixed for 30 seconds.

After 10 μL of casting solution was dropped onto a plasma-treated glass, the glass slide was quickly covered with a CD-ROM template, which was secured using a pressure clamp for 2 hours. After removing the template, the sol-gel pattern should be visible on the glass substrate. Then, the pattern was aged in ambient environment for 20 hours. Later, the pattern was treated using one of the following three treatments: (a) heat treatment at 160 $^{\circ}\text{C}$ with a heating rate of 10 $^{\circ}\text{C}/\text{min}$ for 3 hours followed by oven cool down to 25 $^{\circ}\text{C}$, (b) heat treatment at 400 $^{\circ}\text{C}$ and 600 $^{\circ}\text{C}$ with heating rate of 10 $^{\circ}\text{C}/\text{min}$ and heated for 90 min and

oven cool down to 25 °C, and (c) soaked in 1 M silver nitrate solution for 20 hours followed by rinsing with acetone three times and drying in the air. Except for the sample containing ammonia water (Method 2) that was treated in treatment (c), all other samples (Method 1) were treated by either (a) and (b).

5.2.3 Characterization methods

The AFM images were obtained by a Veeco calibrator AFM equipped with phosphorous doped silicon tip. The tapping mode was performed to scan the pattern surface for showing the particle on the pattern. Scanning electron microscope (SEM) observation was carried out on a field emission microscope (Hitachi S3200) under an acceleration voltage of 15 kV and the samples were imaged after sputtering additional metallic coating. The Oxford Isis energy dispersive X-ray spectrometer system attached on the SEM was used to identify the characteristic X-ray emission of the elements at surface to acquire the elemental information. UV-Vis spectroscopy was performed on Varian Cary 100 spectrophotometer equipped with dual beam chamber, where the nanocomposite patterns on the glass substrate were measured. In order to subtract the absorption caused by glass, the plain glass substrate was measured as reference at the same time.

5.3 Results and discussion

The AFM images of different surfactant-treated, non-treated, PVP, and 3-MTS treated samples after 160 °C annealing are shown in Figure 5.2. The none-treated sample shows

average size of 200 nm particles randomly distributed at the bottom and protrusion areas of the patterns (Figure 5.2a). The cross section profile of AFM images confirms that the height of particles approximate 150-200 nm distributed evenly across the whole pattern. For PVP-treated samples, the particle size is 413 nm with the least number of particles formed on the patterns (Figure 5.2b). The increased particles size indicates that the increased growth rate is due to high reducing power of PVP-treated samples as compared to none-treated ones. PVP is known for its reducing power and capping effect with strong affiliation force with silver nanoparticles.²⁰⁻²² Although larger nanoparticles were produced, they are also evenly distributed on the pattern without showing any selectivity. As for 3-MTS treated sample, the particles of average size at 240 nm are observed (Figure 5.2c). According to the size and number of the particle, 3-MTS treated film also shows higher reducing powder than the none-treated sample although the reducing power is lower than PVP. The particles distribute selectively at the edge and the top areas rather than the bottom areas of the pattern. These results can be confirmed by comparing the roughness measurements on different areas of three samples (Figure 5.2d). The roughness values at the edge, the top, and the bottom areas for both none- and PVP-treated samples are similar, which shows no selective deposition. However, the average roughness at the edge and the top areas vs. at the bottom area of 3-MTS sample is 16 nm vs. 4.5 nm, which indicates the particles are mainly deposited at the edge and the top areas. In the same time, when comparing the particle numbers at different areas, Table 5.1 shows the particle numbers ratio between top/edge to bottom areas significantly increased from 2~3 for none- and PVP-treated samples to 22 for 3-MTS-treated

samples. Thus, 3-MTS shows the most significant effect on selective deposition of silver particles at different areas of patterns (Figure 5.3).

According to our previous study, the polymer within the sol-gel derived nanocomposites tends to diffuse to the surface during the high temperature annealing process. The further condensation reaction and shrinkage of the gel have been found to be the main driving forces. When incorporating silver ions, these ions can be carried by the polymer phase to the surface. PEG have been shown to exhibit the reducing power for silver ions at 160 °C because the oxygen atoms on the carbon backbones tend to oxidize and reduce the silver ion to silver.^{23, 24} This reducing powder depends on the heating temperature and molecular weight of PEG but PEG shows no affiliation force to the silver ions. Thus, non-treated sample shows reducing power but no selectivity in controlling the deposition position. Both PVP^{9, 20, 21} and 3-MTS^{25, 26} show affinity to silver ions. However, the PVP within PEG solution tend to diffuse to the surface of the pattern during high temperature annealing and form silver particles at the surfaces. There is no control of the position when PVP diffuses with PEG at high temperature, and silver particles can be reduced at any position on the surface although PVP exhibits strong bonding with silver. For 3-MTS, during the hydration and condensation reaction of sol-gel reaction, the silanol group of 3-MTS tends to bind to the TMOS matrix and form chemical bonding. During high temperature annealing, the thiol group of 3-MTS will be fixed within the silica matrix to stabilize silver ions.²⁷ Thus, some of silver ions will be trapped within the matrix instead of moving to the pattern surface. Thus, at

valley areas, most of silver ions will be trapped within the matrix instead of diffusing to the surface. On the other hand, a small portion of silver ions will be trapped within thick films, but residual silver ions still diffuse to the protrusion areas with PEG. At the same time, PEG and thiol groups on the surface reduce silver ions and form silver nanoparticles on the thick films. Studies have shown that residual layers with thicknesses of several tens of nanometers may exist via the micro-contact imprint method.¹⁵ For example, AFM images show that the thickness of the residual layers on our samples is around 30 nm. This residual polymer layer usually decreases the selectivity of nanoparticle deposition, which could jeopardize the function of devices. Thus, the distinct particle density between top and bottom areas of the pattern was derived from the immobilization of thiol groups and silver ions, and a distinct silver particles array can be formed. To further demonstrate the selectivity of our deposition method, the sample with 3-MTS was further heat treated in a 1 M AgNO₃ solution for 3 hours, and its SEM images show that the patterned interconnected silver crystals appear only on the sample surface (Figure 5.4).

For most dichromic device applications, the size of silver nanoparticles should be less than 100 nm.^{9, 28} In order to decrease the particles size and increase the density of particles distribution, the samples are high temperature (400 °C - 600 °C) treated to remove the mobile PEG. First, the nucleation rate of nanoparticles was promoted at high temperature to increase particles density. Second, removal of PEG decreases the diffusivity of silver ions and thus controls the further growth of particles. The SEM images show the formation of silver

nanoparticles on the nanocomposite pattern after 400 °C treatments (Figure 5.5a). The silver nanoparticle with the average Feret's diameter of 102 nm have been produced and distributed on the top area of the patterns. The particles are mainly distributed on the top area with the linear density of $3.36 \text{ } \mu\text{m}^{-1}$. It is known that silver nitrate could decompose above 300 °C and reduce to silver with the aid of radicals within sol-gel materials.^{29, 30} Although PEG decomposes above 200 °C, elimination of PEG at high temperature reduces the silver ion diffusivity to the surface and the tendency to grow into larger particles. Thus, silver particles tend to stabilize at small sizes instead of further growing into large particles. At the same time, the Ostwald growth also happens when annealing temperature increases to 600 °C (Figure 5.5b) and average Feret's diameter increases to 128 nm with lower linear density of $2.63 \text{ } \mu\text{m}^{-1}$. Thus, temperature could be used to control the size of silver nanoparticles and the wavelength of the plasmon absorption for optical applications.

High temperature heat treatment requires costly equipment and energy consumption. Also, high temperature treatment increases the diffusivity of the particles, which might decrease the selectivity of particles deposition positions. Thus, the second method of low temperature processes is introduced by selectively deposition Ag on the printed region of a substrate. This is achieved by patterning a layer of reducing agent that initiates the deposition of a metal from solution by means of electroless deposition (ELD). As an alternative to vacuum deposition processes, ELD is a method for obtaining films of a variety of metals or alloys on insulating substrates at low cost.³¹ This method uses metastable solutions

containing complex metal ions (as the source of the metal) and a reducing agent. When immersing a substrate into an ELD solution, the reducing agent supplies the electrons for converting the metal ions into the metal on the surface. In the present study, the ammonia water has been utilized to form silver complex ions for mirror reaction^{32, 33} known as Tollens' reagent. Figure 5.6a shows the SEM images when adding ammonia water into sol-gel nanocomposites where the silver nanoparticles are produced on the protrusion areas of the pattern after 20 hours at room temperature. The nanoparticles are evenly distributed at the protrusion area, indicating the evenly distributed thiol function groups on the surface. The particles have an average size of 67 nm with a higher linear density of $5.65 \text{ } \mu\text{m}^{-1}$. Comparing to the pattern without 3-MTS, the nanoparticles show up at both the top and the bottom area of the pattern, indicating losses the selectivity of distribution of silver nanoparticles (Figure 5.6b). The EDX spectrum indicates the formation of silver nanoparticles after ELD treatment (Figure 5.7a). Also, UV-Vis spectroscopy of silver nanoparticles on the patterns reveals that the maximum absorption appears at 454 nm (Figure 5.7b), which is corresponding to silver nanoparticles of about 65 nm in diameter.³⁴ At the same time, the samples with HNO_3 showed no absorption peak indicating no silver formation (Figure 5.7b). Tollens' reagent is a chemical reagent most commonly used to determine whether a carbonyl-containing compound is an aldehyde or a ketone. The diamminesilver(I) complex form between silver nitrate and ammonia water in the mixture is an oxidizing agent and is the essential reactant in Tollens' reagent.^{35, 36} The diamminesilver(I) complex oxidizes the hydroxyl group and form an aldehyde and in the process is reduced to elemental silver and aqueous ammonia. In the

case of using PEG as the solvent and reducing agent, the active hydroxyl sites for reduction are remarkably decreased and diluted compared to conventional reducing agent, which should be beneficial for a mild and controllable reducing reaction. On a thick film of pattern, high densities of nanoparticles originate from higher concentration of diammine-silver, which are later reduced and anchored on the surface thiol groups. Compared with the samples without thiol group, the unanchored silver nanoparticles cause randomly distributed particles. Thus, formation of complex ions using ammonia water and utilization of thiol groups as nucleation sites both decrease the activation energy of silver reduction at low temperature, where the selectivity is better than that on high temperature treated samples and very few particles are present at the bottom area of the patterns. Though, the kinetics of reduction reaction is slower, both higher selectivity of particle position and uniform particles distribution provide better control for optical applications.

5.4 Conclusion

Versatile polymer-silica nanocomposites films made by microcontact imprint process were utilized as the template to grow silver nanoparticles. The nanoparticles arrays were formed at predetermined areas using thiol containing films. The silver nanoparticles size with average size of 100 - 120 nm can be synthesized by high temperature decomposition. The 67 nm in diameter of silver nanoparticles with higher linear density can be produced at room temperature by ELD. Both high selectivity and uniform distribution provide better control of

nanoparticles arrays. The self-assembly method could be adapted for other metal systems and produce promising nanoparticles arrays for future optical and sensory applications.

5.5 References

1. Haes AJ, Van Duyne RP. A nanoscale optical biosensor: Sensitivity and selectivity of an approach based on the localized surface plasmon resonance spectroscopy of triangular silver nanoparticles. *J Am Chem Soc* 2002 Sep;124(35):10596-10604.
2. Jensen TR, Malinsky MD, Haynes CL, Van Duyne RP. Nanosphere lithography: Tunable localized surface plasmon resonance spectra of silver nanoparticles. *J Phys Chem B* 2000 Nov;104(45):10549-10556.
3. Feldheim DL, Keating CD. Self-assembly of single electron transistors and related devices. *Chem Soc Rev* 1998 Jan;27(1):1-12.
4. Hu MS, Chen HL, Shen CH, Hong LS, Huang BR, Chen KH, et al. Photosensitive gold-nanoparticle-embedded dielectric nanowires. *Nat Mater* 2006 Feb;5(2):102-106.
5. Nam JM, Thaxton CS, Mirkin CA. Nanoparticle-based bio-bar codes for the ultrasensitive detection of proteins. *Science* 2003 Sep;301(5641):1884-1886.
6. Maier SA, Kik PG, Atwater HA, Meltzer S, Harel E, Koel BE, et al. Local detection of electromagnetic energy transport below the diffraction limit in metal nanoparticle plasmon waveguides. *Nat Mater* 2003 Apr;2(4):229-232.
7. Maxwell DJ, Taylor JR, Nie SM. Self-assembled nanoparticle probes for recognition and detection of biomolecules. *J Am Chem Soc* 2002 Aug;124(32):9606-9612.

8. Hu M, Chen JY, Li ZY, Au L, Hartland GV, Li XD, et al. Gold nanostructures: engineering their plasmonic properties for biomedical applications. *Chem Soc Rev* 2006;35(11):1084-1094.
9. Quinten M, Leitner A, Krenn JR, Aussenegg FR. Electromagnetic energy transport via linear chains of silver nanoparticles. *Opt Lett* 1998 Sep;23(17):1331-1333.
10. Pinchuk AO, Schatz GC. Nanoparticle optical properties: Far- and near-field electrodynamic coupling in a chain of silver spherical nanoparticles. *Mater Sci Eng B-Adv Funct Solid-State Mater* 2008 Apr;149(3):251-258.
11. Hamann HF, Woods SI, Sun SH. Direct thermal Patterning of self-assembled nanoparticles. *Nano Lett* 2003 Dec;3(12):1643-1645.
12. Corbierre MK, Beerens J, Beauvais J, Lennox RB. Uniform one-dimensional arrays of tunable gold nanoparticles with tunable interparticle distances. *Chem Mat* 2006 May;18(11):2628-2631.
13. Fernandes R, Li M, Dujardin E, Mann S, Kanaras AG. Ligand-mediated self-assembly of polymer-enveloped gold nanoparticle chains and networks. *Chem Commun*;46(40):7602-7604.
14. Korth BD, Keng P, Shim I, Bowles SE, Tang C, Kowalewski T, et al. Polymer-coated ferromagnetic colloids from well-defined macromolecular surfactants and assembly into nanoparticle chains. *J Am Chem Soc* 2006 May;128(20):6562-6563.
15. Kao YC, Hong FCN. Residual-layer-free direct printing by selective filling of a mould. *J Micromech Microeng* Feb;21(2):8.

16. Folch A, Schmidt MA. Wafer-level in-registry microstamping. *J Microelectromech Syst* 1999 Mar;8(1):85-89.
17. Laibinis PE, Whitesides GM, Allara DL, Tao YT, Parikh AN, Nuzzo RG. Comparison of the Structures and Wetting Properties of Self-Assembled Monolayers of Normal-Alkanethiols on the Coinage Metal-Surfaces, Cu, Ag, Au. *J Am Chem Soc* 1991 Sep;113(19):7152-7167.
18. Schreiber F. Structure and growth of self-assembling monolayers. *Prog Surf Sci* 2000 Nov-Dec;65(5-8):151-256.
19. Sellers H, Ulman A, Shnidman Y, Eilers JE. Structure and Binding of Alkanethiolates on Gold and Silver Surfaces - Implications for Self-Assembled Monolayers. *J Am Chem Soc* 1993 Oct;115(21):9389-9401.
20. Washio I, Xiong YJ, Yin YD, Xia YN. Reduction by the end groups of poly(vinyl pyrrolidone): A new and versatile route to the kinetically controlled synthesis of Ag triangular nanoplates. *Adv Mater* 2006 Jul;18(13):1745-+.
21. Huang HH, Ni XP, Loy GL, Chew CH, Tan KL, Loh FC, et al. Photochemical formation of silver nanoparticles in poly(N-vinylpyrrolidone). *Langmuir* 1996 Feb;12(4):909-912.
22. Sun YG, Mayers B, Herricks T, Xia YN. Polyol synthesis of uniform silver nanowires: A plausible growth mechanism and the supporting evidence. *Nano Lett* 2003 Jul;3(7):955-960.

23. Luo CC, Zhang YH, Zeng XW, Zeng YW, Wang YG. The role of poly(ethylene glycol) in the formation of silver nanoparticles. *J Colloid Interface Sci* 2005 Aug;288(2):444-448.
24. Nam S, Parikh DV, Condon BD, Zhao Q, Yoshioka-Tarver M. Importance of poly(ethylene glycol) conformation for the synthesis of silver nanoparticles in aqueous solution. *J Nanopart Res Sep*;13(9):3755-3764.
25. Shankaran DR, Uehera N, Kato T. Determination of sulfur dioxide based on a silver dispersed functional self-assembled electrochemical sensor. *Sens Actuator B-Chem* 2002 Dec;87(3):442-447.
26. Guo HQ, Tao SQ. Silver nanoparticles doped silica nanocomposites coated on an optical fiber for ammonia sensing. *Sens Actuator B-Chem* 2007 Apr;123(1):578-582.
27. Chumanov G, Sokolov K, Cotton TM. Unusual extinction spectra of nanometer-sized silver particles arranged in two-dimensional arrays. *J Phys Chem* 1996 Mar;100(13):5166-5168.
28. Fort E, Ricolleau C, Sau-Pueyo J. Dichroic thin films of silver nanoparticle chain arrays on faceted alumina templates. *Nano Lett* 2003 Jan;3(1):65-67.
29. Huang MH, Choudrey A, Yang PD. Ag nanowire formation within mesoporous silica. *Chem Commun* 2000(12):1063-1064.
30. Cao JM, Cao YL, Chang X, Zheng MB, Liu JS, Ji HM. Synthesis of silver nanoparticles within ordered CMK-3 mesoporous carbon. *Nanoporous Materials Iv*. Amsterdam: Elsevier Science Bv, 2005. p. 423-426.

31. Milan Paunovic MS. *Fundamentals of Electrochemical Deposition*. New York: John Wiley & Sons, 1998.
32. Yin YD, Li ZY, Zhong ZY, Gates B, Xia YN, Venkateswaran S. Synthesis and characterization of stable aqueous dispersions of silver nanoparticles through the Tollens process. *J Mater Chem* 2002;12(3):522-527.
33. Montazer M, Alimohammadi F, Shamei A, Rahimi MK. In situ synthesis of nano silver on cotton using Tollens' reagent. *Carbohydr Polym* Jan;87(2):1706-1712.
34. Bogle KA, Dhole SD, Bhoraskar VN. Silver nanoparticles: synthesis and size control by electron irradiation. *Nanotechnology* 2006 Jul;17(13):3204-3208.
35. Benet WE, Lewis GS, Yang LZ, Hughes DEP. The mechanism of the reaction of the Tollens reagent. *J Chem Res* Dec(12):675-677.
36. Dondi R, Su W, Griffith GA, Clark G, Burley GA. Highly Size- and Shape-Controlled Synthesis of Silver Nanoparticles via a Templated Tollens Reaction. *Small* Mar;8(5):770-776.

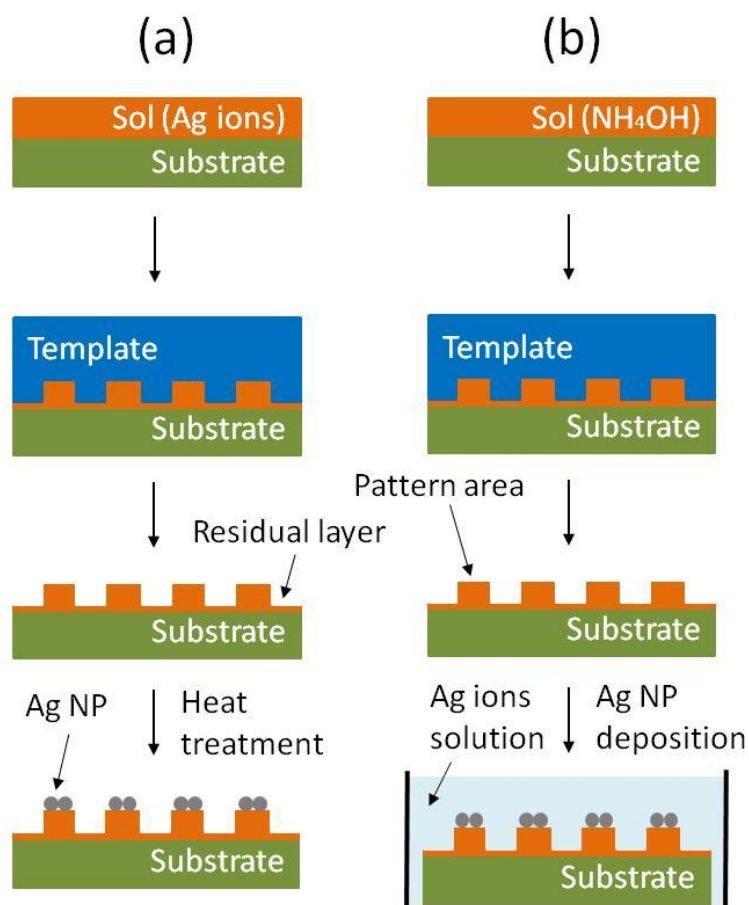


Figure 5.1 Two different processes of producing patterned silver nanoparticles. (a) A PEG-sol containing silver ion was casted on a glass substrate followed by imprint, drying, and heat treatment. (b) A PEG-sol containing ammonia water either with or without 3-MTS was casted on a glass substrate followed by imprint, drying, and room temperature silver deposition in a 1 M AgNO_3 solution.

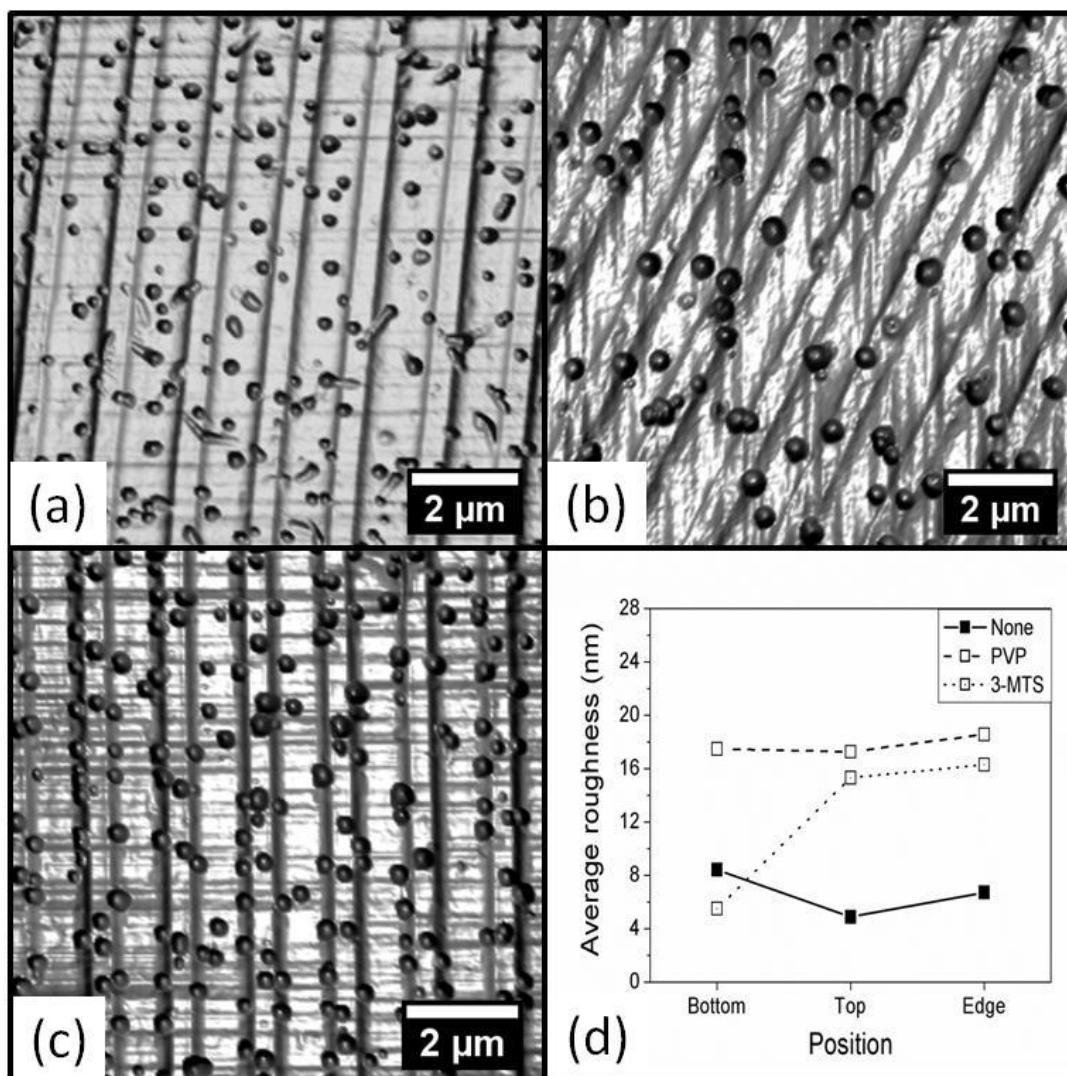


Figure 5.2 AFM images of patterned surface containing silver nanoparticles created from different surfactant solutions by performing heat treatment at 160 °C for 3 hours. The surfactant solution for each pattern contains (a) none, (b) PVP, and (c) 3-MTS, respectively. The average roughness at different spots of each film pattern was summarized in (d).

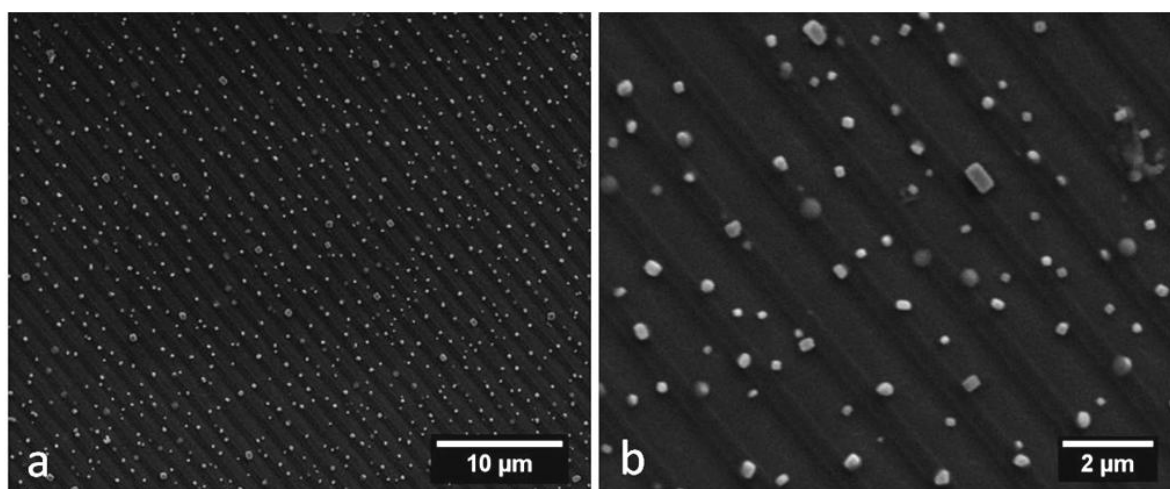


Figure 5.3 SEM images of patterned silver nanoparticles after heat-treating 3-MTS contained films at 160 °C are shown at (a) 2,500x and (b) 9,000x magnifications.

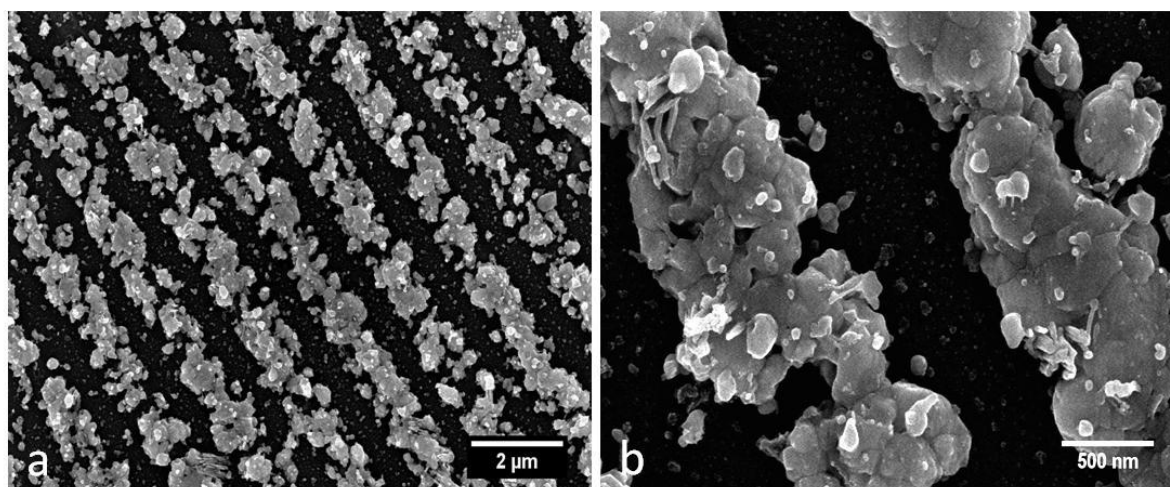


Figure 5.4 SEM images of patterned silver nanoparticles created by heat-treating 3-MTS contained film for 3 hours at 160 °C in 1 M AgNO_3 solution. The images are shown at (1) 9,000x and (2) 40,000x.

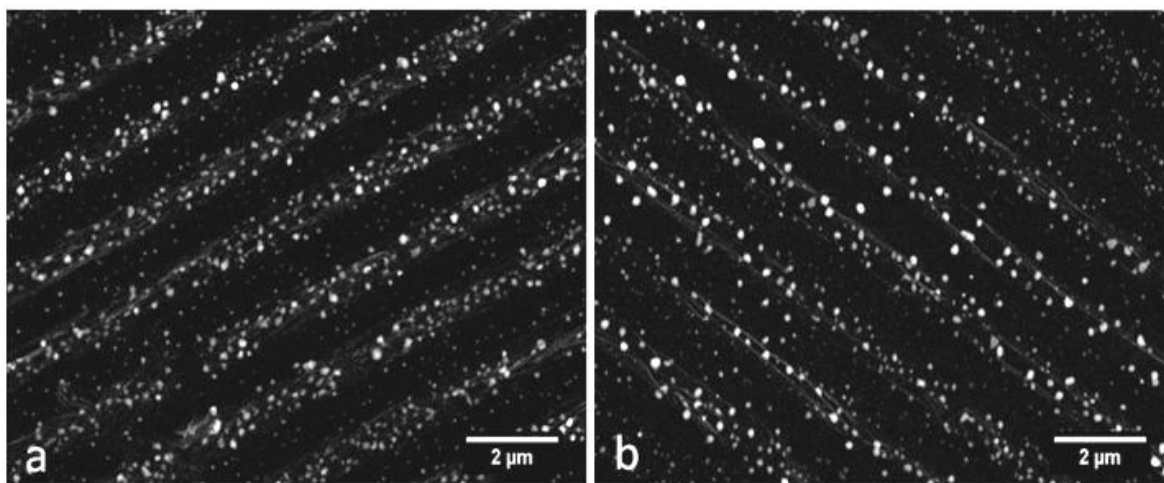


Figure 5.5 SEM images of patterned silver nanoparticles created by heat-treating 3-MTS contained film for 2 hours at (a) 400 °C and (b) 600 °C. Both images are magnified at 10,000x.

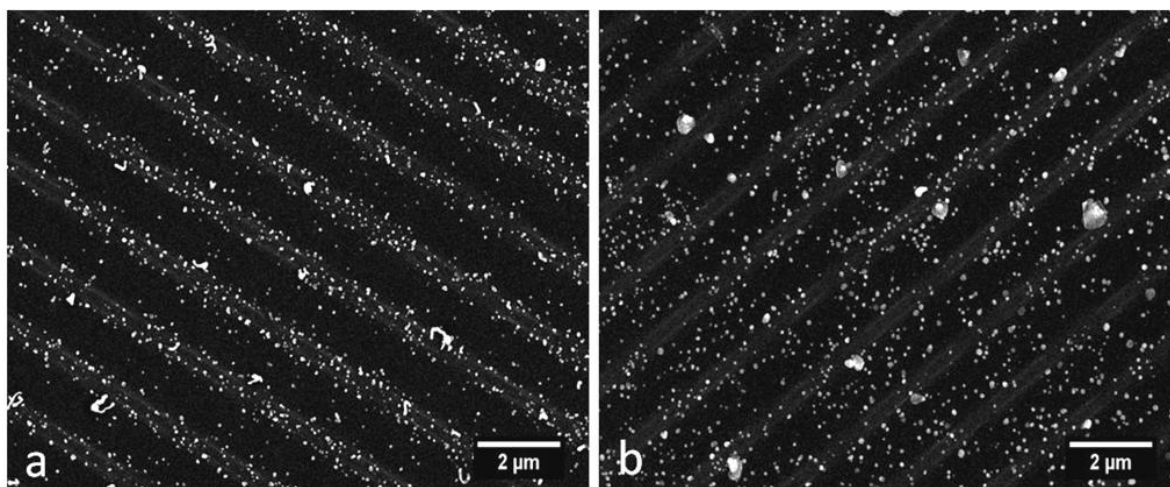


Figure 5.6 SEM images of patterned silver nanoparticles that were prepared from patterned samples of mixing PEG-sol and ammonia water (a) with and (b) without 3-MTS followed by 20 hours of room temperature treatment in 1 M AgNO_3 solution.

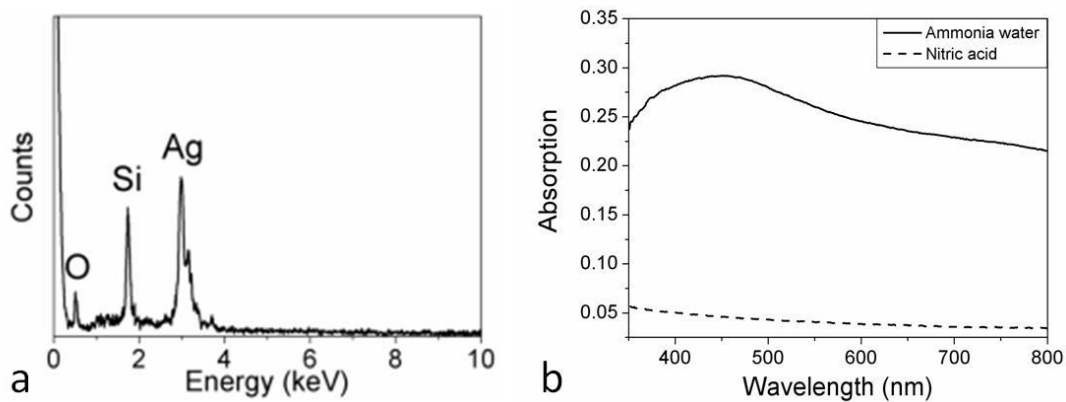


Figure 5.7 (a) EDX spectrum of silver nanoparticles. (b) UV-Vis spectrum of patterned silver nanoparticles created by treating PEG-sol sample containing either ammonia water (solid line) or nitric acid (dashed line) in 1 M AgNO_3 solution at 25 °C for 20 hours.

Table 5.1 Particles distribution of different surfactant at various spots of the film.

Samples	Linear density at edge ($1/\mu\text{m}$)	Ratio Pattern area : Residual layer
None	0.375	2.062
PVP	0.325	3.05
3-MTS	0.892	22.182

Chapter 6

Direct Scaffolding of Biomimetic Hydroxyapatite-gelatin Nanocomposites using Aminosilane Cross-linker for Bone Regeneration

Chi-Kai Chiu¹, Joao Ferreira², Tzy-Jiun M. Luo¹, Haixia Geng^{2,3},
Feng-Chang Lin⁴, Ching-Chang Ko^{2,5}

1. Department of Materials Science and Engineering, EBI 3002, North Carolina State University, Raleigh, NC 27606, US
2. Oral Biology Program, School of Dentistry, University of North Carolina, CB #7454, Chapel Hill, NC 27599, US
3. Dental School of Jining Medical College, Jining, China
4. Department of Biostatistics, University of North Carolina, Chapel Hill, US
5. Department of Orthodontics, School of Dentistry, University of North Carolina, CB #7454, Chapel Hill, NC 27599, US

Abstract

Hydroxyapatite-gelatin modified siloxane (GEMOSIL) nanocomposite was developed by coating, kneading and hardening processes to provide formable scaffolding for alloplastic graft applications. The present study aims to characterize scaffolding formability and mechanical properties of GEMOSIL, and to test the *in vitro* and *in vivo* biocompatibility of GEMOSIL. Buffer Solution initiated formable paste followed by the sol-gel reaction led to a final hardened composite. Results showed the adequate coating of aminosilane, 11-19 wt%, affected the cohesiveness of the powders and the final compressive strength (69 MPa) of the composite. TGA and TEM results showed the effective aminosilane coating that preserves hydroxyapatite-gelatin nanocrystals from damage. Both GEMOSIL with and without titania

increased the mineralization of preosteoblasts *in vitro*. Only did titania additives revealed good *in vivo* bone formation in rat calvarium defects. The scaffolding formability, due to cohesive bonding among GEMOSIL particles, could be further refined to fulfill the complicated scaffold processes.

6.1 Introduction

Critical size defect in bone represents a challenging problem and may require multiple-phase surgery to achieve adequate reparation and function. Autografts have achieved various degrees of success in treating bone defects. However, the autograft is limited by the donor site morbidity, prolonged rehabilitation, increased risk of deep infection and restricted availability. Allografts might cause potential risks of transmitted diseases such as HIV or contamination.^{1,2} Thus, the development of synthetic biomaterials for alloplastic grafts is in high demand.

Hydroxyapatite (HAp) is a calcium-containing biomaterial composed of chemical elements similar to the mineral components in natural bone. The HAp possesses excellent properties that are required for bone grafts such as great stiffness, biocompatibility, cell affinity, and osteoconductivity.³⁻⁶ There are two methods for HAp synthesis: sintering (high temperature) and precipitation (lower temperature). Because of lower surface activity, scaffolding of HAp requires a stereo lithographic process followed by high temperature (> 1250 °C) sintering, a procedure limiting its clinical applicability. Calcium phosphate cement

(CPC) involves dissolution of amorphous calcium phosphate and phase transformation to stabilized HAp precipitation. During the dissolution phase, CPC does not exhibit sufficient plasticity to form a controllable porous scaffold although blending with porogens (e.g., salt particles^{7, 8} and paraffin microspheres^{9, 10}) was reported. Alternatives have used calcium-alumina and magnesium-phosphate for 3D scaffolding.^{11, 12}

Hydroxyapatite-gelatin (HAp-Gel) system was developed by Chang et al. in 2003¹³ and it has been proven with chemical binding between hydroxyapatite and gelatin molecule, which mimics natural bone microstructure. The hydroxyapatite formed nanocrystal clusters within gelatinous particulates in a colloid slurry at 38 °C. Various attempts have been made to cross-link HAp-Gel slurry particles after dehydration and solidification.^{14, 15} Among these, siloxane cross-linker^{16, 17} has been found to provide biocompatibility as biodegradable scaffold for bone regeneration, and thus has attracted lots of attention recently. A sol-gel process has been utilized by Ren et al. to synthesize porous gelatin-siloxane scaffolds for bone tissue engineering.^{18, 19} The biodegradable gelatin and the bioactive inorganic components such as silanol group and calcium ions contribute to osteoconductivity. A solution process mixing aminosilane, bis[3-(trimethoxysilyl)propyl]-ethylenediamine (enTMOS) - a siloxane cross-linker, with HAp-Gel slurry combined with the salt leaching technique has also been utilized for hydroxyapatite-gelatin modified siloxane (GEMOSIL) scaffolding.^{20, 21} Although the pore morphology of scaffolds was well controlled, the resultant scaffold was too brittle and contained inherent cracks. The solution process also

took too long time to dehydrate because of excessive water. The contact angle measurements (data not shown here) also indicate that the freeze-dried HAp-Gel powders possess specific surface energy and reactivity in the ambient environment than the sintered hydroxyapatite powder. This discovery raises the question whether such high reactivity could render a powder process with robust formability to allow direct scaffolding at room temperature.

In the present study, we synthesized a GEMOSIL porous scaffold derived from a formable paste by a new powder process consisting of coating, kneading and hardening. The results showed that the gelatin content of HAp-Gel powder requires only minimal addition of buffer solution, yielding adhesion among the particles. When incorporating enTMOS coating, hydrogen bonding further enhanced the paste formability and finally HAp-Gel nanocrystals were interwoven inside the aminosilica matrix after hardening. The new powder process also allows the incorporation of TiO_2 to further improve osteoconductivity and bone formation. We hypothesized that the amount of aminosilane determines the formability of the paste and the strength of the final composite, and the presence of TiO_2 promotes osteogenic response *in vitro* and *in vivo*. Therefore, the objective of the present study is to investigate the effect of the enTMOS cross-linker on physical, mechanical, and surface chemical properties of the nanocomposites. Cell viability and animal test for GEMOSIL with/without TiO_2 addition were also studied.

6.2 Materials and Methods

6.2.1 Materials

The stock slurry of hydroxyapatite-gelatin (HAp-Gel) was prepared by the simultaneous titration method using peristaltic pumps (Masterflex, Cole-Parmer, USA), and a pH controller (Bukert 8280 H, Germany).¹³ Briefly, a double jacket beaker served as the reaction vessel. The temperature of the water bath was digitally controlled to within 0.1 °C. The amount of Ca(OH)₂ and H₃PO₄ was calculated to make 10 g of HAp. A homogeneous suspension that included Ca(OH)₂ dispersed in 1.2 L of an aqueous H₃PO₄ solution with a measured amount of gelatin (Type A : From porcine skin, Sigma-Aldrich, St. Louis, MO, USA) was gradually added to the reaction vessel through peristaltic pumps. After the coprecipitation reaction, the total volume was adjusted to 2.6 L. The temperature and pH of reaction solution in the vessel were maintained at 38 °C and 8.0, respectively. The amount of gelatin in H₃PO₄ aqueous solution was 5 g. The resulting slurries will be centrifuged at 5000 rpm under 4 °C for 30 minutes to remove excess water. The condensed HAp-Gel will be freeze dried at -80 °C overnight followed by lyophilization until dry, followed by grinding into fine particles. Bis[3-(trimethoxysilyl)propyl]-ethylenediamine (enTMOS) was purchased from Gelest, Inc (Morrisville, PA, USA). Phosphate buffered saline (PH = 7.4) was obtained from Sigma-Aldrich Co. and TiO₂ (Evonik Aeroxide® P25) powder was supplied by Evonik Degussa Co. (Parsippany, NJ, USA) and used without further treatment.

6.2.2 Sample preparation and conditions

A 400 mg of HAp-Gel powder was transferred into a mortar and grinded into fine powder. The predetermined amount of enTMOS was added according to Table 6.1 and the mixture was continuously blended for another 3 minutes to form GEMOSIL powder. This GEMOSIL powder mixture appeared uniformly yellow color at this step and later was used for TEM measurement. To convert the mixture into GEMOSIL paste, 640 μL of phosphate buffer saline (PBS, 1X) was added to the GEMOSIL powder. After mixing for 2 minutes, another 160 μL of PBS was added into mixture followed by kneading for 2 minutes until the sample showed plasticity. At this state, GEMOSIL appeared as paste and was pressed with a mold to create round shape disc samples and cylindrical shape samples. All samples were solidified within an hour. The amount of enTMOS (95% concentration) used was 48, 96 and 144 μL , equivalent to 10.6, 19.2, 26.3 weight percentage. Sample notations were coded as GEMOSIL-11, GEMOSIL-19 and GEMOSIL-26 respectively, based on the enTMOS content (Table 6.1). The samples without enTMOS were also made for comparison (coded as HAp-Gel-PBS). For samples that contained TiO_2 , the same procedure was followed except that a 38 mg of P25 powder was added prior to the mixing with enTMOS; and notation was coded as GEMOSIL-19-P25. All five groups of samples were used in the following experiments except for cell culture testing.

6.2.3 Mechanical testing

The mechanical testing consisted of compressive and Vickers hardness tests. After drying the samples under ambient environment for 5 days, the cylindrical shape samples with a 1 : 2 ratio of diameter (3.5 mm) to length (7.0 mm) were prepared for compressive test. The round disc samples for hardness testing were polished with the sand paper of grid sizes 600 and 1200 before measurement. Compressive testing was performed on an Instron 4204 (Canton, MA, USA) compression tester with a testing rate of 0.5 mm/min. Testworks 4 software (MTS, Inc) was used to analyze the data and the compressive strength was determined from the maximum strength value on the stress-strain curve. The hardness value was measured by Buehler MicrometII (Lake Bluff, IL, USA) Vickers hardness tester using 50 g constant load at a loading time of 15 sec. The measurement was performed every 24 hours in the period of 168 hours (7 days). The testing results were analyzed by one-way ANOVA and followed by Tukey HSD comparison among the material groups. IBM SPSS statistics 19 (SPSS Inc., Chicago, IL, US) was used for all statistical analysis.

6.2.4 Contact angle testing

The disk samples were dried under ambient environment for 5 days. The contact angle was measured using conventional contact angle instrument (200-F1, Rame-Hart Instrument Co., Succasunna, NJ, US) by placing a disc shape sample onto a platform underneath a water syringe and in front of a CCD camera. DropImage 2.4.04 software (Rame-Hart Instrument Co.) was used for measurements and the images of the droplet were taken when each water

droplet stabilized and remained symmetrical on the disc surface. The contact angle was measured from the digital photo with image analysis software. Each measurement was repeated two times.

6.2.5 Thermogravimetric analyzer (TGA) testing

GEMOSIL samples of various amounts of enTMOS (Table 6.1) were synthesized, cured in the air, and grinded into powders. Each 10 mg of powder was placed on a platinum sample holder, and the sample holder was loaded inside the Q-500 thermogravimetric analyzer (TA Instrument, New Castle, DE, US). Q Series 2.5 software (TA Instrument) was used for data analysis. The TGA test was performed from 30 °C to 800 °C with a heating rate of 5 °C/min. Weight changes were recorded versus temperature. The weight percentage of individual components (H₂O, gelatin, HAp, Silica) in each sample was estimated from the TGA data.

6.2.6 Transmission electron microscopy (TEM)

Transmission electron microscopy (TEM) was performed on a JEOL 2010F using an accelerated voltage of 200 kV. To prepare samples suitable for TEM observation, sample was prepared by dispersing enTMOS-treated GEMOSIL powder in methanol and sonicating for 20 minutes. Then, formvar/carbon-coated TEM grids were immersed in the mixture solution followed by drying at room temperature.

6.2.7 Cell culture testing

The GEMOSIL-19 was chosen, based on the result of mechanical tests, to further study its influence on preosteoblast proliferation and differentiation. Three experimental groups of materials were investigated, including GEMOSIL-19, GEMOSIL-19-P25, and dishes as received without coating (control). Preosteoblasts, MC3T3-E1, were cultured in 96-well plates (Falcon, Becton, Dickinson Labware, Franklin Lakes, NJ, USA) in which all wells were coated with the specified material. Cells were seeded at a density of 1×10^4 per milliliter using α -MEM medium supplemented with 10% of FBS and 1% penicillin/streptomycin under 37 °C, 5% CO₂ atmosphere. Cellular metabolic activity was determined with MTS colorimetric assay at day 1, 4, 7, 10 and 13 according to the manufacturer's instructions (CellTiter96; Promega, Madison, WI, USA). Briefly, 20 μ L of MTS reagent was added to the cells in 96 well plates at the end of the designed cultivation period and incubated for 1 hour at 37 °C. Colored formazan products were quantified by measuring absorbance at 490 nm (plate reader). The average background (medium plus MTS without cells) was subtracted from the absorbance values of experimental groups for normalization purposes. The resultant optical densities were quantified to assess cell proliferation for each group. Three samples were tested with triplicate at each time point for each group.

Assessment for cell differentiation on the material was performed using the Alizarin Red as a calcium mineralization stain. Three groups including GEMOSIL-19 coated, GEMOSIL-19-P25 coated and uncoated (as received) 35 mm Petri dishes were used for

differentiation studies. The same groups without cell seeding were used as control for quantification analysis. A total of 3.2×10^5 MC3T3-E1 cells were seeded onto the dish and pre-cultured for 3 days to reach confluence using the above same growth medium and conditions. After three days, the differentiation medium was supplemented with 10 mM β -glycerophosphate and 0.2 mM ascorbic acid and cultured for 14 days. Visual indication for calcification was achieved by Alizarin Red (Acros Organics, Geel, Belgium) staining using manufacturer's protocol.²² The quantification results of mineralization characteristics were derived from color differences (δ) by CIELAB method. Optical color measurement, CIELAB (the Commission Internationale de l'Eclairage) tristimulus values, was based on the principle of light transmission which is wavelength-dependent. Given an externally applied illuminating light to the stain, the detectable color spectrum was used as signals to differentiate and analyze the degree of mineralization. The dish colors of the digital images were converted to CIELAB tristimulus values for each image pixel. The tristimulus values of ten evenly distributed points from each dish were calculated relative to the Commission Internationale de l'Eclairage (CIE). The characteristic values and standard deviations for L, a^* , and b^* were calculated using the Photoshop software (Adobe System Inc., CA). For each material group, a formula to calculate the mineralization's characteristics was a color difference between the with and the without cell dishes, $\delta = ((L-L_o)^2 + (a^*-a^*_o)^2 + (b^*-b^*_o)^2)^{1/2}$ where (L, a^* , b^*) and (L_o , a^*_o , b^*_o) were tristimulus values for the having cell and non-cell dish, respectively. The mean δ were compared among three groups using one way ANOVA

and Tukey-Kramer's HSD. IBM SPSS Statistics 19 (SPSS Inc., Chicago, IL, US) was used for all statistical analysis.

6.2.8 Bone regeneration in rat calvarium defects

GEMOSIL-19 and GEMOSIL-19-P25 porous scaffolds with bases were implanted in 8mm critical-size defects (CSD) in rat calvaria. The craniofacial defect consisted of an 8mm-diameter calvaria critical-size defect, which has previously been described.²³ Briefly, 11- to 13-week-old Sprague-Dawley rats (Charles River, Wilmington, MA) were anesthetized and an 8-mm-diameter defect was created on the calvaria bone using a dental trephine drill. Three rats were used for each material. Animals were euthanized either at 8 weeks after surgery, calvaria specimens were retrieved and fixed in 10% formalin for 7 days and then transferred to isopropanol 70% for non-decalcified sectioning. The tissue sections were stained with Stevenel's Blue and Van Gieson to assess the formation of newly formed bone (NFB) tissue. All procedures were compliant with the animal care regulation at University of North Carolina - Chapel Hill (IACUC09-270.0-B).

6.3 Results

The formable GEMOSIL paste is illustrated in Figure 6.1a. This plastic property would be ideal for making complicated scaffold geometries as well as injectable scaffolding (Figure 6.1b). The final composites appear white or yellowish depending on the amount of enTMOS and TiO₂ additive. The compressive strength (Figure 6.2) varies significantly with the

amount of enTMOS ($p < 0.01$). The strength increases as enTMOS increases and reaches a maximum when enTMOS amount is about 10.6 ~ 19.2 wt% without apparent difference in the compressive strength according to Tukey HSD test. However, adding TiO₂ lowered the strength by 20% when compared to the sample without it.

One way ANOVA showed that Vickers hardness (HV) (Figure 6.3) of the composite increased significantly with enTMOS ($p < 0.01$). The value of HV reached the maximum when sample contained 26.3 wt% of enTMOS. Compared to the aminosilane treated samples, the untreated samples were more susceptible to fracture and had lower hardness. By adding TiO₂, the surface hardness increased 5% compared to the sample without TiO₂ due to the high modulus of TiO₂ particles. The hardness value increased over time and reached a maximum after 120 hours, which indicates that the complete hardening time would be 5 days.

According to TGA measurements, the absorbed water inside the GEMOSIL solid could not be removed completely until 200 °C²⁴ (Figure 6.4). The data revealed that slightly more water was trapped in GEMOSIL than in HAp-Gel-PBS sample. The HAp-Gel-PBS samples showed three distinct weight drops, contributing to the degradation of gelatin.²⁵ The GEMOSIL sample showed similar TGA pattern when compared to HAp-Gel-PBS sample, except for the final degradation region between 400 °C - 500 °C, which was attributed to the degradation of aminosilica. The weight reduction increased as the amount of aminosilica

increased; this was due to the decomposition of hydrocarbon on aminosilica molecules. The amount of aminosilica after setting was derived by TGA results and Figure 6.5 compares the theoretical weight percentage of aminosilica to that of the actual content in the final composite. The discrepancy between the theoretical and actual contents suggests that there was aminosilica remained in nanocomposites at 800 °C and the residual component increased as the aminosilica amount increased. The remaining weight was contributed by silica and HAp phases after 800 °C.

The TEM images were obtained for GEMOSIL-11 (Figure 6.6a) and GEMOSIL-19 (Figure 6.6b) samples after enTMOS treatment. The needle shape structures represent the typical HAp-Gel nanocrystals derived from the precipitation process.¹³ The TEM images also confirmed the integrity of HAp-Gel nanocrystals where the needle shape crystals are embedded inside the matrix without damage. This result indicates the new dry grinding process used to apply enTMOS coating preserves the structure of HAp-Gel nanocrystals. However, the GEMOSIL-11 sample shows more distinct needle shape nanocrystals, which might be due to the different amount of enTMOS coating.

There is no obvious difference in the contact angle measurements between HAp-Gel-PBS and GEMOSIL samples (Figure 6.7). The enTMOS did not change the hydrophilic properties of the composites. However, the addition of the TiO₂ increased the contact angle by 10 degrees, indicating a decrease of hydrophilicity on the material surface, which might

affect cell adhesion.²⁶ The cell growth (proliferation) curves showed no differences over time between the GEMOSIL-19-P25 dish and the positive control (Figure 6.8). The cell growth on the GEMOSIL-19 had the lowest growing rate among three groups. However, Alizarin red stain showed the equal ability of preosteoblasts to mineralize at day 14 on both the GEMOSIL and the GEMOSIL-19-P25 superior to the control (Figure 6.9).

For the calvarium defect study, both GEMOSIL-19 and GEMOSIL-19-P25 revealed new bone formation 8 weeks after implantation. GEMOSIL-19-P25 (red arrows in Figure 6.10b) had more areas and thicker islands (50-300 μm diameter) of bone formation within the pore space than GEMOSIL-19 (red arrows in Figure 6.10a), suggesting that titania additives could increase *in vivo* bone in-growth on the HAp-Gel biomaterial surfaces. GEMOSIL-19 resulted in thin (15-35 μm) and network-like bone nodules.

6.4 Discussion

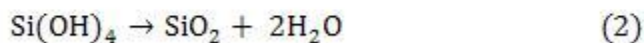
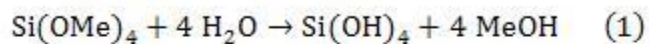
The cohesive strength of the powder depends upon interparticular interactions such as electrostatic forces, van der Waals force, hydrogen bonding, and steric hindrance. Gelatin is known to possess polyampholytic and polyelectrolytic properties due to its intrinsic protein composition.^{27, 28} The carboxylic and amino groups of gelatin may absorb water molecular and cause swelling.²⁹ The swelling of gelatin maintains water content and hydrogen bonding within GEMOSIL paste providing lubrication for molecular movement, which contributes to materials' formability. Simultaneously, these functional groups also form hydrogen bonds

with silanol group of aminosilica^{21, 30} to provide additional cohesive strength of formability. The siloxane has been shown to form hydrogen bonding with hydroxyapatite,³¹ which also provides additional cohesive strength. This synergetic effect between biological and mineral components contributed to the formable plasticity of the GEMOSIL paste. The hydrogen bonding provided weak bonding force and allowed short distance sliding between the HAp-Gel particles, which resulted in formable properties.^{32, 33} The paste could be packed into a syringe and extruded without creeping overtime, and the final porous scaffolding (Figure 6.1b) suggests that the present processes are capable of achieving acceptable moldable property, which would be suitable for complex geometry scaffolding.

The residual water in GEMOSIL samples was more than that of HAp-Gel-PBS sample, which indicates the stronger hydrogen bonding within GEMOSIL nanocomposites causing excessive water absorption.³⁴ This strong hydrogen bonding is critical to the plasticity and processibility of the material. The gelatin degradation temperature was 420 °C in HAp-Gel and shifted to higher temperature when enTMOS content increased, which proved the presence of chemical bonding between HAp-Gel and enTMOS. It is interesting to note on Figure 6.5 that the percentage of the decomposed aminosilica from the TGA calculation decreased with the increase of enTMOS coating in the composite, which indicates the alkyl side groups did not decompose completely. This result may be due to that the alkyl side groups inside a highly cross-linked silica phase did not fully react with oxygen. The TEM images of GEMOSIL-11 (Figure 6.6a) and GEMOSIL-19 (Figure 6.6b) appeared to confirm

that the aminosilica layer preserved the structure of HAp-Gel nanocrystals from damage during the coating process. This coating process by dry grinding method was also effective as evidenced that 8~16 wt% aminosilica was quantified via TGA data.

Besides the formability, siloxane also provided the effective cross-linkage for HAp-Gel within nanocomposites. Siloxane has been considered as potentially effective cross-linking agent due to their interaction with some poly-amino acids and proteins via both electrostatic forces and hydrogen bondings.^{35, 36} Gelatin consists of various amounts of aminoacids, including glycine, proline and hydroxyproline.³⁷ It would be expected that these amino acid contained in its structure could form the hydrogen bonding with silanol groups. In our previous FTIR study,²¹ the bands at 1647 cm^{-1} in the spectra corresponded to the gelatin's amide I band due to CO stretching. The results showed a red shift in amide I band to the lower wavenumber indicating the hydrogen bonding of the CO in gelatin to the silanol hydrogen.³⁸ These interactions could be used to induce physical cross-linkage.^{39, 40} The formation of the continuous aminosilica phases within GEMOSIL nanocomposites relies on the cross-linkage of the enTMOS. This sol-gel reaction consists of hydrolysis and condensation reactions. First, enTMOS reacted with water and replaced methoxy (Me) group by hydroxyl (OH) group with methanol release attributed to hydrolysis reaction (Eq.1). Then, the two hydrolyzed molecules can link together in a condensation reaction to form a siloxane bond (Eq.2).



The compression data confirmed our hypothesis that there exists an optimal range of enTMOS for GEMOSIL nanocomposites. Both the high and low amount of enTMOS reduces the strength of the composite. In theory, HAp-Gel particles do not form strong aggregates when there are insufficient enTMOS binders. The HAp-Gel-PBS sample without enTMOS showed a low compressive strength. On the contrary, high amount of binder could leave a thick, porous silica layers between the particles, which are prone to fracture. The redundant coating increases the amount of nanoporous, brittle glassy phases between HAp-Gel particles and, therefore, increase the chance for crack nucleation and propagation, which decrease the mechanical properties of composite materials.^{41, 42} The increased volume of brittle silica phase due to thicker coating among HAp-Gel particles were also confirmed by TGA results. The enTMOS coating provides strong intermolecular force for the nanocomposites and hence increases the surface hardness. The hardness test was performed to measure the resistance to permanent shape change when a force applied to assess the intermolecular bonds within composite materials.⁴³ The data showed that hardness increases with the amount of enTMOS. This coupling agent is primarily used to enhance the bonding among particles and between different phases within composite materials. The amount of coupling agent has a great influence on the micro structure and strength of the composites.^{44,}

⁴⁵ The hardness value also increased throughout the aging process (up to 120 hours), which is

attributed to the complete condensation reaction within the gel that further enhances the network structure and mechanical properties of the nanocomposites.

From these remarks, a model (coating, kneading and hardening) can be proposed to explain the setting mechanism, as illustrated in Figure 6.11. Coating stage: The coating layer of enTMOS was proven by detecting the chemical bonding formation between different phases of compounds.²¹ At this point, hydrogen bonds and Si-O-P bonding began to form at the interface between the thin enTMOS coating and HAp-Gel particles. In this stage, the particles did not aggregate together because there was not enough water to induce sol-gel reactions. Kneading stage: After adding PBS and performing kneading process, water molecules filled in the gaps between enTMOS and HAp-Gel, forming hydrogen bonds within/between phases. In the same time, the excessive water also induced the hydrolysis and condensation reactions of enTMOS, making paste less formable over time. The processing window (working time) for formable plasticity properties was around five minutes. Hardening stage: At the end of working time, hardness increased due to the formation of silica phase. This formation of the solid matrix was the result of the condensation reaction. The silica phase was believed to be nanoporous structure that contained water and held the structure together. During hardening, condensation reaction continued to occur and further strengthened the silica phase, which increased the overall strength of the final sol-gel materials.⁴⁶ Further drying eliminated the water inside the pore structures and condensed the silica phases into rigid monoliths. The present dry powder approach shortened the processing

time for samples and scaffold fabrications. The drying process lasted for twelve hours until the weight stopped changing, which was relatively short compared to the previous solution method.²¹ In summary, at the completion of sol-gel reaction, enTMOS served as binder and matrix for the HAp-Gel particles and formed rigid nanocomposites.

TiO₂ appeared to enhance osteogenesis by affecting both proliferation and differentiation of preosteoblasts. The color analysis was directed towards performing stain intensity and wave analysis of photon signals generated by the transmission light, quantifying the signals and correlating the sources with microstructural parameters, e.g., sizes and numbers of mineral nodules. The CIELAB color system provided an orthogonal, three-dimensional space in which color is defined by three coordinates: lightness (L), red-green (a*), and yellow-blue (b*). The uniform color space provided by the CIELAB system had the property that a perceived difference, defined as δ , between colors is quantitatively the same in all its areas.⁴⁷ It appeared the mineralization (ability of biomaterials to promote cell differentiation) of three groups was distinguishable using quantitative δ values.

The *in vivo* data further confirmed the *in vitro* outcomes. Our data were consistent with those of previous studies suggesting that TiO₂ could enhance the biocompatibility of bioceramics because TiO₂ increased calcium ion interactions, promoted protein and cell adhesion, and differentiation and mineralization of preosteoblasts.^{48, 49} Hydrophobic adsorption has been considered as one of the most important mechanisms for protein

adsorption. Several studies have shown the similar results that the quantity of proteins adsorbed is higher on the more hydrophobic surface.^{50, 51} Besides stable adsorption of protein, the protein must retain its configuration to react with receptors for cell attachment. Topoglidis and coworkers have found stable immobilisation of various proteins on TiO₂ film with a high binding stability and no detectable denaturation.⁵² Also, the molecular dynamic simulation showed denaturation of BMP-2 induced by adsorption was not observed at the initial stage of adsorption.⁵³ These proteins can facilitate the attachment of various cells such as osteoblasts that can stimulate bone repairs. Thus, relative hydrophobic GEMOSIL-19-P25 suggested that there might be more proteins absorbed onto the material surfaces. Sequentially, more MC3T3-E1 cells adhered to the material surface and facilitate cellular proliferation and differentiation. Histological data proved that newly formed bone was abundant and seamlessly adhered to the GEMOSIL-19-P25 surface more than GEMOSIL-19, suggesting that TiO₂ might prepone host marrow stromal cells to osteogenic path. The formation of the harvasian system suggested that an intramembranous bone formation may be associated with the TiO₂ additives. Future investigation assessing gene expression may provide necessary information for its biological mechanism. The compressive results implied that TiO₂ might decrease efficacy of enTMOS cross-linker. It is, however, a trade off by using TiO₂ to promote biological properties of the GEMOSIL scaffold.

6.5 Conclusion

The present study reports a new method of scaffolding made of hydroxyapatite-gelatin and aminosilane nanocomposites. The moldable properties of GEMOSIL owing to inherent gelatin's and aminosilane's bonding interaction would be favored for complicated scaffolding. In particular, the aminosilane binder affects final mechanical strength of the scaffold in a non-linear manner, with optimal concentration being 11-19 wt%. The process also allowed the addition of TiO₂ to enhance osteoconductivity of MC3T3-E1 preosteoblasts and *in vivo* bone formation. In summary, the new GEMOSIL nanocomposites could provide opportunities of easy handling, sturdy materials, and direct scaffolding for potential tissue engineering applications.

6.6 Acknowledgement

This work was supported, in part, by NIH/NIDCR K08DE018695, NC Biotech and American Association for Orthodontist Foundation. Although CC Ko is the co-founder of Ironwood Materials Science Inc., this study was not supported by any companies.

6.7 References

1. Hou CH, Yang RS, Hou SM. Hospital-based allogenic bone bank-10-year experience. *J. Hosp. Infect.* 2005;59:41.
2. Nishida J, Shimamura T. Methods of reconstruction for bone defect after tumor excision: A review of alternatives. *Med. Sci. Monitor* 2008;14:RA107.

3. Bucholz RW, Carlton A, Holmes RE. Hydroxyapatite and Tricalcium Phosphate Bone-Graft Substitutes. *Orthop. Clin. North Am.* 1987;18:323.
4. Ishihara K, Arai H, Nakabayashi N, Morita S, Furuya K. Adhesive Bone-Cement Containing Hydroxyapatite Particle as Bone Compatible Filler. *J. Biomed. Mater. Res.* 1992;26:937.
5. Radin SR, Ducheyne P. Effect of Bioactive Ceramic Composition and Structure on in-Vitro Behavior .3. Porous Versus Dense Ceramics. *J. Biomed. Mater. Res.* 1994;28:1303.
6. Narasaraju TSB, Phebe DE. Some physico-chemical aspects of hydroxylapatite. *J. Mater. Sci.* 1996;31:1.
7. Tas AC. Preparation of porous apatite granules from calcium phosphate cement. *J. Mater. Sci.-Mater. Med.* 2008;19:2231.
8. Hesarakı S, Zamanian A, Moztarzadeh F. The influence of the acidic component of the gas-foaming porogen used in preparing an injectable porous calcium phosphate cement on its properties: Acetic acid versus citric acid. *J. Biomed. Mater. Res. Part B* 2008;86B:208.
9. Yu NYC, Schindeler A, Little DG, Ruys AJ. Biodegradable Poly(alpha-hydroxy acid) Polymer Scaffolds for Bone Tissue Engineering. *J. Biomed. Mater. Res. Part B*;93B:285.
10. Silva TSN, Primo BT, Silva AN, Machado DC, Viezzer C, Santos LA. Use of calcium phosphate cement scaffolds for bone tissue engineering: in vitro study. *Acta Cir. Bras.* 2011;26:7.

11. Maier AK, Dezmirean L, Will J, Greil P. Three-dimensional printing of flash-setting calcium aluminate cement. *J. Mater. Sci.*;46:2947-54.
12. Klammert U, Vorndran E, Reuther T, Muller FA, Zorn K, Gbureck U. Low temperature fabrication of magnesium phosphate cement scaffolds by 3D powder printing. *J. Mater. Sci.-Mater. Med.*;21:2947.
13. Chang MC, Ko CC, Douglas WH. Preparation of hydroxyapatite-gelatin nanocomposite. *Biomaterials* 2003;24:2853.
14. Chang MC, Ko CC, Douglas WH. Modification of hydroxyapatite/gelatin composite by polyvinylalcohol. *J. Mater. Sci.* 2005;40:2723.
15. Chang MC, Douglas WH. Cross-linkage of hydroxyapatite/gelatin nanocomposite using imide-based zero-length cross-linker. *J. Mater. Sci.-Mater. Med.* 2007;18:2045.
16. Dunn B, Miller JM, Dave BC, Valentine JS, Zink JJ. Strategies for encapsulating biomolecules in sol-gel matrices. *Acta Mater.* 1998;46:737.
17. Coradin T, Bah S, Livage J. Gelatine/silicate interactions: from nanoparticles to composite gels. *Colloid Surf. B-Biointerfaces* 2004;35:53.
18. Ren L, Tsuru K, Hayakawa S, Osaka A. Novel approach to fabricate porous gelatin-siloxane hybrids for bone tissue engineering. *Biomaterials* 2002;23:4765.
19. Ren L, Tsuru K, Hayakawa S, Osaka A. In vitro evaluation of osteoblast response to sol-gel derived gelatin-siloxane hybrids. *J. Sol-Gel Sci. Technol.* 2003;26:1137.

20. Ko CC, Luo TJM, Chi L, Ma A. Hydroxyapatite/Gemosil Nanocomposite. *Advances in Bioceramics and Porous Ceramics*, vol. 29. Westerville: Ceramic Engineering and Science Proceedings; John Wiley & Sons; 2009;29:123-35.
21. Luo TJM, Ko CC, Chiu CK, Llyod J, Huh U. Aminosilane as an effective binder for hydroxyapatite-gelatin nanocomposites. *J. Sol-Gel Sci. Technol.* 2010;53:459.
22. Gregory CA, Gunn WG, Peister A, Prockop DJ. An Alizarin red-based assay of mineralization by adherent cells in culture: comparison with cetylpyridinium chloride extraction. *Anal. Biochem.* 2004;329:77.
23. Ferreira J. Engineering hydroxyapatite-gelatin nanocomposites with MAPC cells for calvarium bone regeneration. vol. Ph.D.: University of North Carolina-Chapel Hill, 2011: (923638399).
24. Zholobenko V, Garforth A, Dwyer J. TGA-DTA study on calcination of zeolitic catalysts. *Thermochim. Acta* 1997;294:39.
25. Word AG CA. *The science and technology of gelatin*: London: Academic Press, 1977.
26. Horbett TA, Waldburger JJ, Ratner BD, Hoffman AS. Cell-Adhesion to a Series of Hydrophilic-Hydrophobic Copolymers Studied with a Spinning Disk Apparatus. *J. Biomed. Mater. Res.* 1988;22:383.
27. Veis A. *The macromolecular chemistry of gelatin*. New York: Academic Press, 1964.
28. Darder M, Ruiz AI, Aranda P, Van Damme H, Ruiz-Hitzky E. Bio-nanohybrids based on layered inorganic solids: Gelatin nanocomposites. *Curr. Nanosci.* 2006;2:231.

29. Ren L, Tsuru K, Hayakawa S, Osaka A. Synthesis and characterization of gelatin-siloxane hybrids derived through sol-gel procedure. *J. Sol-Gel Sci. Technol.* 2001;21:115.
30. Coradin T, Durupthy O, Livage J. Interactions of amino-containing peptides with sodium silicate and colloidal silica: A biomimetic approach of silicification. *Langmuir* 2002;18:2331.
31. Dupraz AMP, deWijn JR, vanderMeer SAT, deGroot K. Characterization of silane-treated hydroxyapatite powders for use as filler in biodegradable composites. *J. Biomed. Mater. Res.* 1996;30:231.
32. Laird DA. Bonding between polyacrylamide and clay mineral surfaces. *Soil Sci.* 1997;162:826.
33. Lee SR, Park HM, Lim H, Kang TY, Li XC, Cho WJ, Ha CS. Microstructure, tensile properties, and biodegradability of aliphatic polyester/clay nanocomposites. *Polymer* 2002;43:2495.
34. Tang Y, Finlay JA, Kowalke GL, Meyer AE, Bright FV, Callow ME, Callow JA, Wendt DE, Detty MR. Hybrid xerogel films as novel coatings for antifouling and fouling release. *Biofouling* 2005;21:59.
35. Coradin T, Livage J. Effect of some amino acids and peptides on silicic acid polymerization. *Colloid Surf. B-Biointerfaces* 2001;21:329.
36. Coradin T, Coupe A, Livage J. Interactions of bovine serum albumin and lysozyme with sodium silicate solutions. *Colloid Surf. B-Biointerfaces* 2003;29:189.

37. Segtnan VH, Isaksson T. Temperature, sample and time dependent structural characteristics of gelatine gels studied by near infrared spectroscopy. *Food Hydrocolloids* 2004;18:1.
38. Farhat IA, Orset S, Moreau P, Blanshard JMV. FTIR study of hydration phenomena in protein-sugar systems. *J. Colloid Interface Sci.* 1998;207:200.
39. Fujitsu M, Hattori M, Tamura T. Effects of hydroxy compounds on gel formation of gelatin. *Colloid Polym. Sci.* 1997;275:67.
40. Wu J, Chiu SC, Pearce EM, Kwei TK. Effects of phenolic compounds on gelation behavior of gelatin gels. *J. Polym. Sci. Pol. Chem.* 2001;39:224.
41. Baji A, Wong SC, Srivatsan TS, Njus GO, Mathur G. Processing methodologies for polycaprolactone-hydroxyapatite composites: A review. *Mater. Manuf. Process.* 2006;21:211.
42. Causa F, Netti PA, Ambrosio L, Ciapetti G, Baldini N, Pagani S, Martini D, Giunti A. Poly-epsilon-caprolactone/hydroxyapatite composites for bone regeneration: in vitro characterization and human osteoblast response. *J. Biomed. Mater. Res. Part A* 2006;76A:151.
43. Thomas V, Dean DR, Jose MV, Mathew B, Chowdhury S, Vohra YK. Nanostructured biocomposite scaffolds based on collagen coelectrospun with nanohydroxyapatite. *Biomacromolecules* 2007;8:631.
44. Schutte CL. Environmental Durability of Glass-Fiber Composites. *Mater. Sci. Eng. R-Rep.* 1994;13:265.

45. Kent MS, Smith GS, Baker SM, Nyitray A, Browning J, Moore G, Hua DW. The effect of a silane coupling agent on water adsorption at a metal/polymer interface studied by neutron reflectivity and angle-resolved X-ray photoelectron spectroscopy. *J. Mater. Sci.* 1996;31:927.
46. Dumas J, Quinson JF, Bovier C, Baza S, Serughetti J. Correlations between Textural and Mechanical-Properties in Wet Silica-Gels. *J. Non-Cryst. Solids* 1986;82:220.
47. German R, Guzowski M, Wright D. The colour of gold-silver-copper alloys. *Gold Bulletin* 1980;13:113.
48. Ellingsen JE. A Study on the Mechanism of Protein Adsorption to TiO_2 . *Biomaterials* 1991;12:593.
49. Kitsugi T, Nakamura T, Oka M, Yan WQ, Goto T, Shibuya T, Kokubo T, Miyaji S. Bone bonding behavior of titanium and its alloys when coated with titanium oxide (TiO_2) and titanium silicate (Ti_5Si_3). *J. Biomed. Mater. Res.* 1996;32:149.
50. Malmsten M. Formation of adsorbed protein layers. *J. Colloid Interface Sci.* 1998;207:186.
51. Yoon JY, Park HY, Kim JH, Kim WS. Adsorption of BSA on highly carboxylated microspheres - Quantitative effects of surface functional groups and interaction forces. *J. Colloid Interface Sci.* 1996;177:613.
52. Topoglidis E, Cass AEG, O'Regan B, Durrant JR. Immobilisation and bioelectrochemistry of proteins on nanoporous TiO_2 and ZnO films. *J. Electroanal. Chem.* 2001;517:20.

53. Utesch T, Daminelli G, Mroginski MA. Molecular Dynamics Simulations of the Adsorption of Bone Morphogenetic Protein-2 on Surfaces with Medical Relevance. *Langmuir*;27:13144.

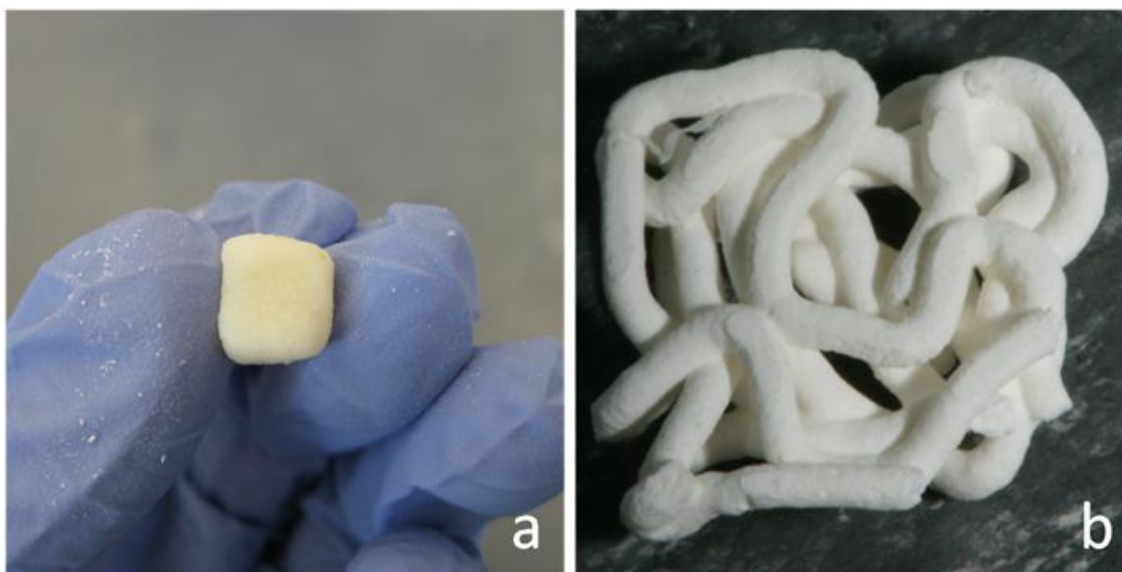


Figure 6.1 GEMOSIL paste for direct scaffolding. Formable GEMOSIL paste can be molded into a (a) cube by hand and injected to form a (b) porous scaffold.

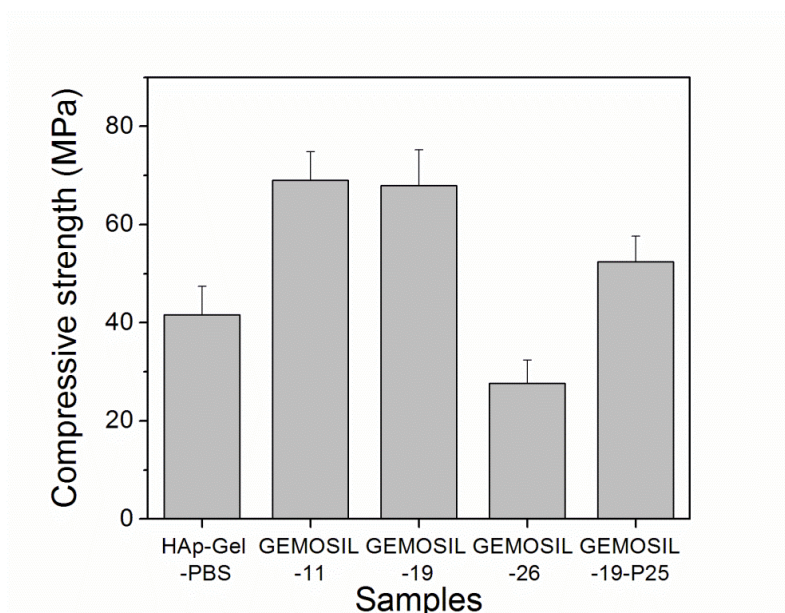


Figure 6.2 The compressive strength of GEMOSIL nanocomposites. The optimal compressive strengths of GEMOSIL nanocomposites are observed when enTMOS percentage is between 11 wt% and 19 wt%. Decrease of strength due to TiO_2 (GEMOSIL-19-P25) is not statistically significant ($p = 0.25$).

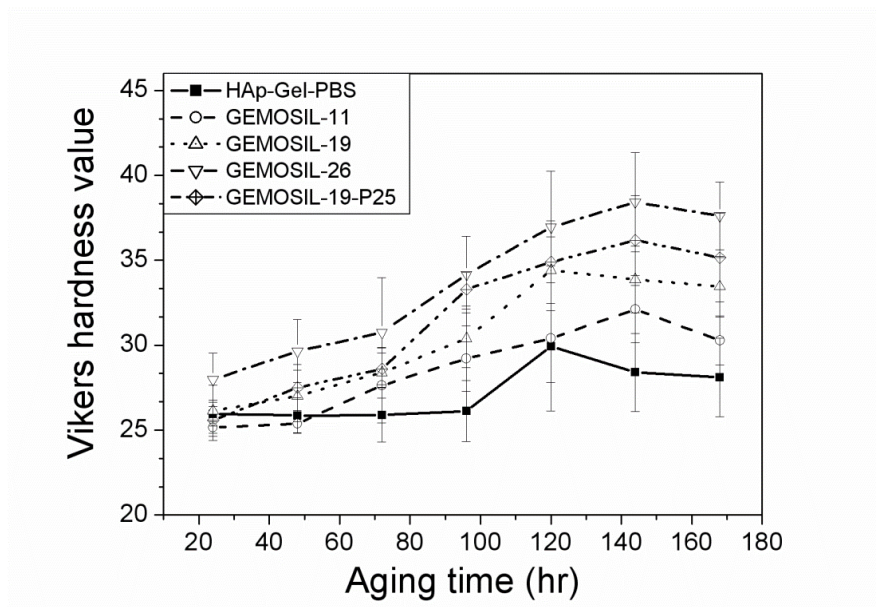


Figure 6.3 Vickers hardness (HV) of GEMOSIL nanocomposites. HV increases with the amount of enTMOS ($p < 0.01$) and the aging time. HV reaches the maximum when sample contains 26.3 wt% of enTMOS.

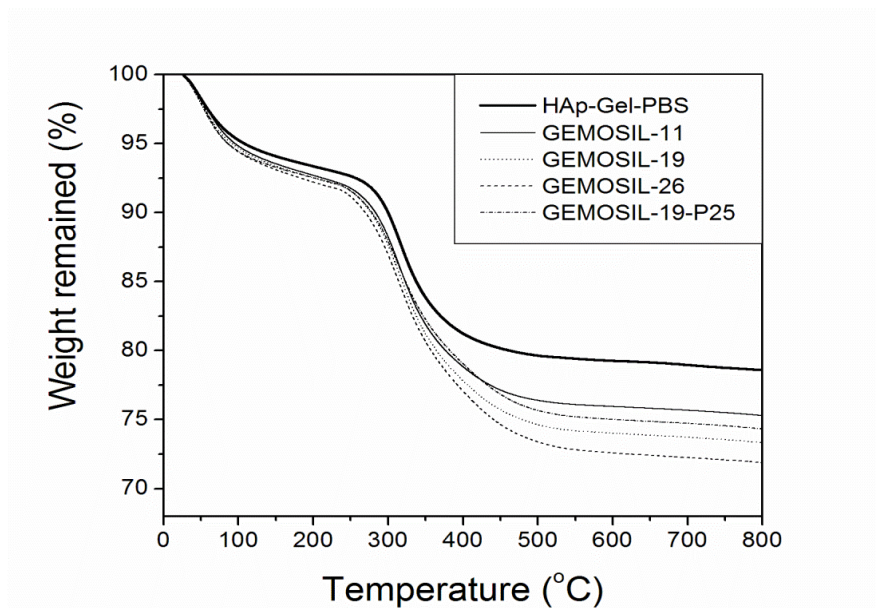


Figure 6.4 TGA analysis of GEMOSIL nanocomposites. Distinct weight drop patterns are attributed to the elimination of water, gelatin, and alkyl side groups.

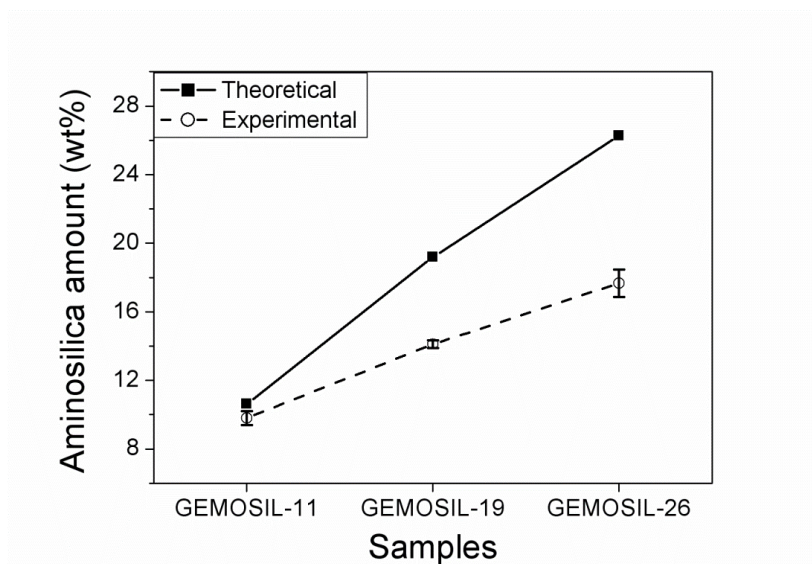


Figure 6.5 Theoretical predictions and experimentally measured weight percentages of aminosilica in GEMOSIL samples. The discrepancy between the two measures suggests that there exists residual aminosilica in the nanocomposites after 800 °C treatment and residuals increase with aminosilica amount.

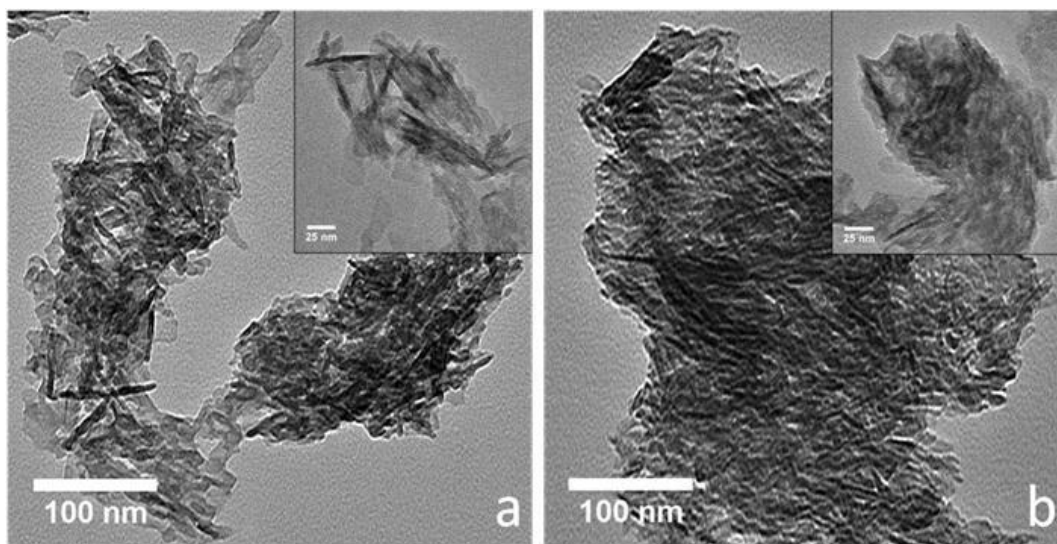


Figure 6.6 TEM images of (a) GEMOSIL-11 at 100 kx (inset at 200 kx) and (b) GEMOSIL-19 at 100 kx (inset at 200 kx) samples taken from the mixing step. Results confirm the integrity of the HAp-Gel nanocrystals where the needle shape crystals are embedded inside the matrix without damage. However, the GEMOSIL-11 sample shows more distinct needle shape crystals than GEMOSIL-19 sample, which is due to the lower amount of enTMOS coating layer.

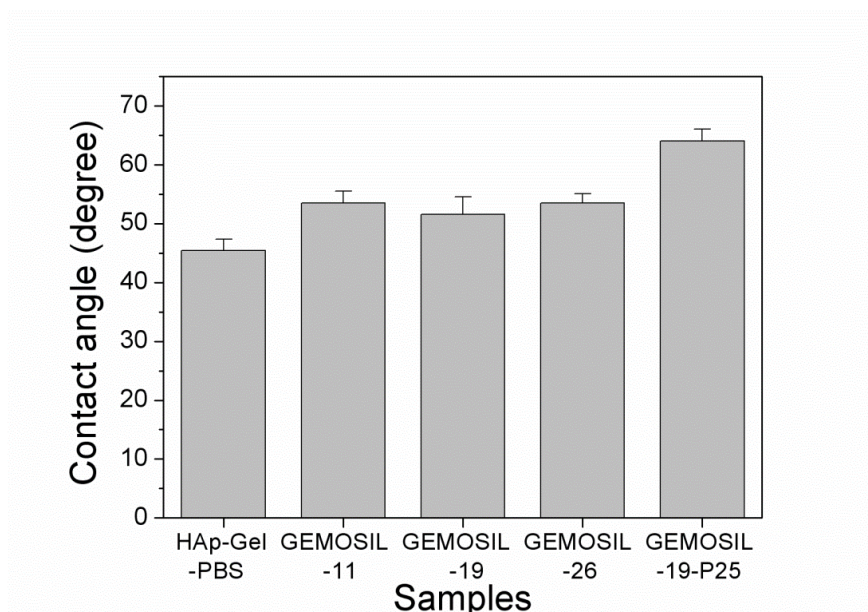


Figure 6.7 Contact angles measurements show no obvious difference between HAp-Gel-PBS and GEMOSIL samples. However, the addition of the TiO₂ (GEMOSIL-19-P25) increases the contact angle by about 10 degrees.

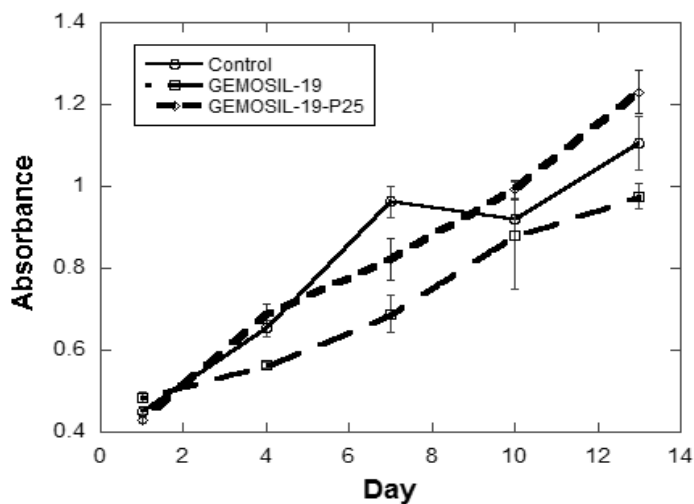


Figure 6.8 The growth curve of preosteoblasts, MC3T3-E1, was measured by formazan absorbance using CellTiter kits (Promega, Madison). There were significant differences among groups over time (1, 4, 7, 10 and 13 days) ($p < 0.05$).

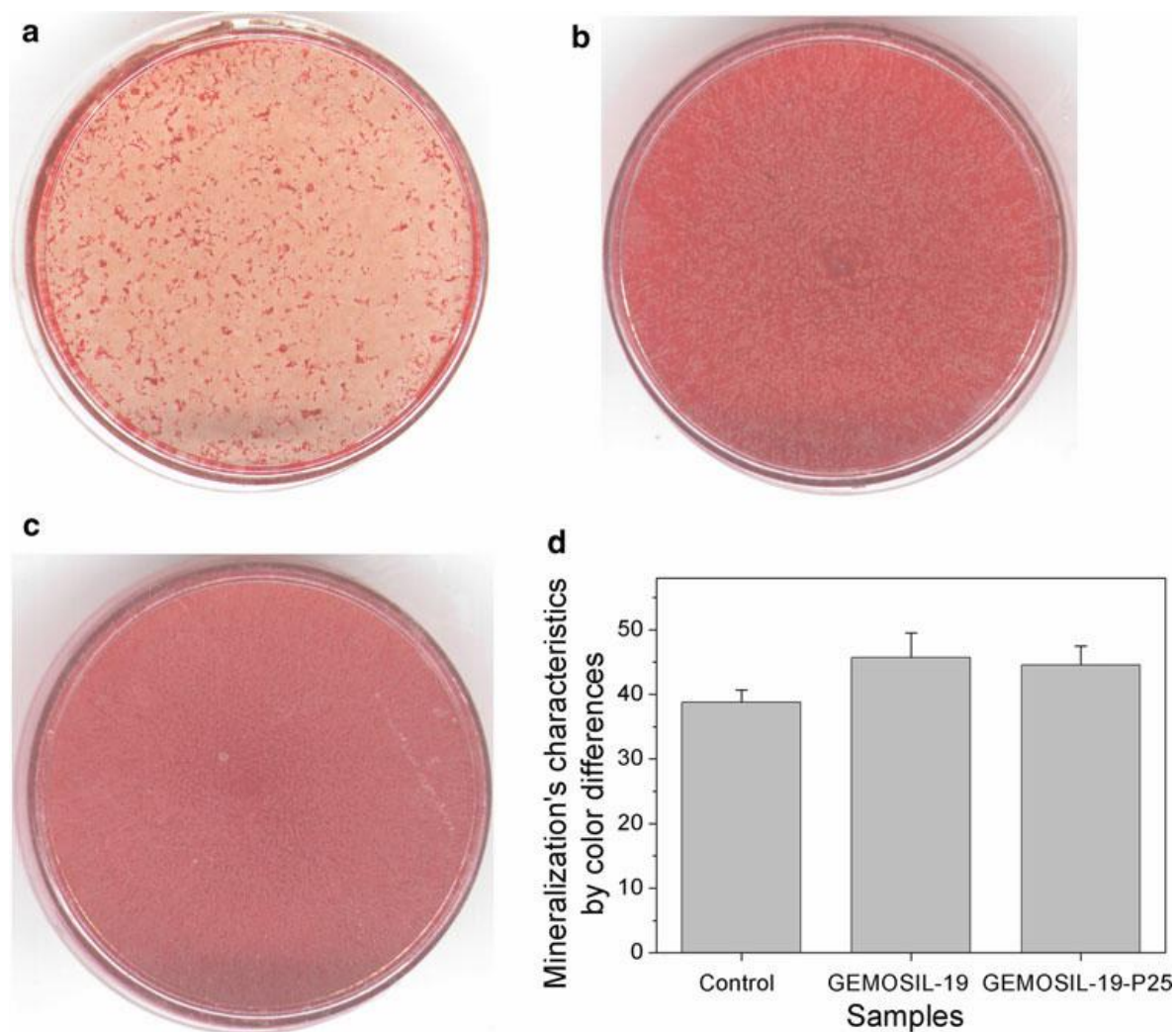


Figure 6.9 Alizarin red stain for MC3T3-E1 at the differentiation day 14 shows mineral nodules red for the (a) control. Both (b) GEMOSIL-19 and (c) GEMOSIL-19-P25 show abundant mineral stains covering the entire culture surface. (d) Quantification results of mineralization characteristics of control, GEMOSIL-19 and GEMOSIL-19-P25 derived from color differences (δ) by CIELAB method.

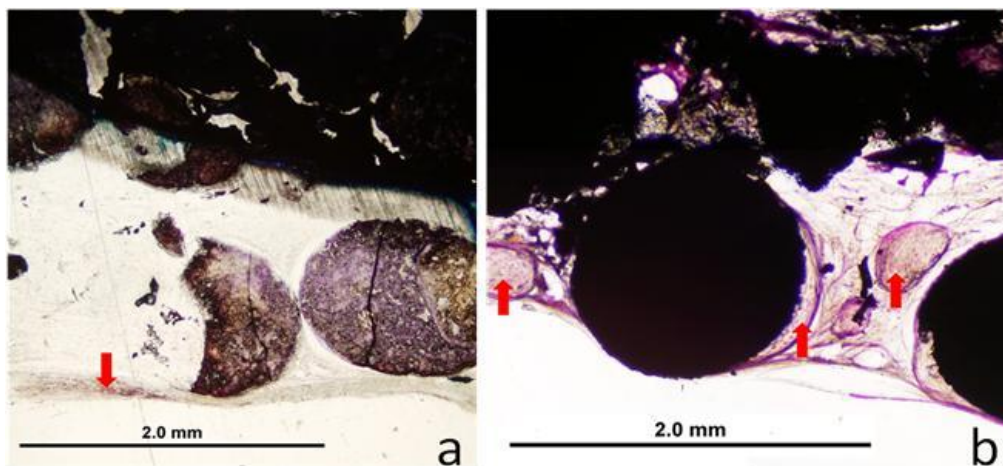


Figure 6.10 The rat calvarium defect study shows the new bone formation 8 weeks after implantation of the (a) GEMOSIL-19 and (b) GEMOSIL-19-P25.

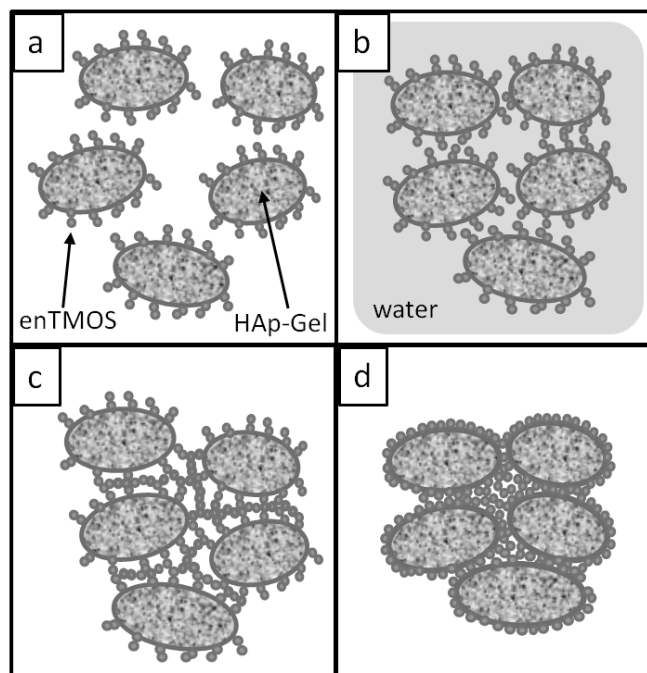


Figure 6.11 Setting mechanism for the GEMOSIL scaffold. (a) coating : hydrogen and chemical bonding begin to form between the thin enTMOS coating and HAp-Gel particles, (b) kneading : The hydrogen bonding provides the weak bonding and allowed short distance sliding among the HAp-Gel particles, which results in shapeable paste type. properties and (c,d) hardening : solidification and particle packing start due to the gelation reaction and become strong monolith after aging and drying.

Table 6.1 Composition of GEMOSIL nanocomposites

Sample	Notation code	HAp-Gel (mg)	enTMOS (μL)	PBS (μL)	P25 (mg)
1	HAp-Gel-PBS	400	0	800	0
2	GEMOSIL-11	400	48	800	0
3	GEMOSIL-19	400	96	800	0
4	GEMOSIL-26	400	144	800	0
5	GEMOSIL-19-P25	400	96	800	38

Chapter 7

In-situ Hybridization of Calcium Silicate and Hydroxyapatite-Gelatin Nanocomposite Enhances Physical Properties and *In Vitro* Osteogenesis

Chi-Kai Chiu¹, Dong-Joon Lee², Tzy-Jiun M. Luo¹, Li Zhang^{2,3},
Feng-Chang Lin⁴, Ching-Chang Ko^{2,5}

1. Department of Materials Science and Engineering, EBI 3002, North Carolina State University, Raleigh, NC 27606, US
2. Oral Biology Program, School of Dentistry, University of North Carolina, CB #7454, Chapel Hill, NC 27599, US
3. Faculty of Stomatology, Capital Medical University, Beijing, China
4. Department of Biostatistics, University of North Carolina, Chapel Hill, US
5. Department of Orthodontics, School of Dentistry, University of North Carolina, CB #7454, Chapel Hill, NC 27599, US

Abstract

We demonstrate a new GEMOSIL-calcium silicate (GEMOSIL-CS) nanocomposites using in-situ formation of calcium silicate through a interfacial interactions between gelatin, silica and $\text{Ca}(\text{OH})_2$. The study aims to examine the formation and reinforcement mechanism of GEMOSIL-CS, and to test the *in vitro* biocompatible and osteogenic properties. The setting time can be adjusted between 3 to 6 minutes and it can be set at ambient or within PBS solution. The formation of calcium silicate phase is evaluated by FTIR and XRD measurements. The interfacial bindings within nanocomposites are studied by FTIR and TGA. Both gelatin and calcium silicate have been found critical to the structure integrity and mechanical strength. Cell viability is assessed by proliferation assay, while ultrastructural

evaluation was investigated by SEM and TEM. Osteogenic differentiation is evaluated by observing type I collagen secretion and mineralized nodule formation. The major advantages of this present approach are that it is simple, fast setting, low cost, and has potential to incorporate bioactive molecules, such as growth factors for clinical tissue engineering applications.

7.1 Introduction

Bone substitutes (alloplastic grafts) have been widely studied to overcome the limitations associated with autografts and allografts, such as donor site complications and immune rejections. However, most of alloplastic grafts lack cellular stimulation and not osteoconductive. A new alternative of bone augmentation procedure is to use tissue engineering approach that applies synthetic scaffold-cell constructs for in situ tissue formation.¹⁻³ Ideal synthetic scaffolds must fulfill the following criteria⁴⁻⁶: 1. Biocompatible and osteoconductive properties to stimulate bone growth. 2. Temporary mechanical support at defect areas. 3. Suitable degradation rate to match bone growth. 4. Porous structure to allow cell penetration and bone in-growth. Today, materials developed for tissue engineering scaffolds include polymers, calcium containing ceramics, and hybrid of polymers and ceramics.

Polymer scaffolds including natural and synthetic polymers such as polysaccharides, collagen, poly(α -hydroxy ester) and hydrogels have been studied for tissue engineering

applications.^{7, 8} Among these, biodegradable polyester such as poly(lactic-co-glycolic acid) (PLGA) and Poly-L-lactide acid (PLLA) are the most commonly used materials because they are FDA-approved suture materials for medical uses. In addition, these polymers are suitable for scaffolding by various methods such as phase separation, leaching and casting methods. Also, the biodegradation rate can be adjusted by the compositions and crystallinity of the polymer to match the bone remodeling rate. However, the modulus (1.2 - 3.0 GPa)^{9, 10} of these polymers are about 6-10 times lower than the cortical bones (12 - 18 GPa),¹¹ which greatly limits their clinical applications for bone tissue engineering.

Calcium-containing biomaterials, such as hydroxyapatite (HAp) and calcium silicate (CS), are composed of chemical elements similar to the inorganic components in natural bones. The HAp has shown to possess great stiffness, mechanical strength, excellent biocompatibility, cell affinity, and osteoconductivity.^{12, 13} It has been utilized as space filler and replacement as bone graft. However, the requirement of high temperature (> 1250 °C) processing and poor resorption ability hinder its clinical applicability. Recently, a calcium silicate (CS) based bone graft has been developed with compressive strength within the cortical bones range.¹⁴ Besides mechanical properties, calcium silicate based materials have been found to foster osteoblast adhesion, growth, and differentiation due to the release of the calcium ions.^{15, 16} However, the previously reported formation of calcium silicate was based on solution-precipitation of pre-sintered calcium silicate particles that were synthesized using high temperature annealing process at 600 - 1000 °C, which decreases degradability of CS

phases.^{17, 18} Annealing process also precludes the possibility of incorporating polymeric phase, such as collagen and growth factors.

Although polymers usually exhibit low strength and stiffness, they have been used to toughen the inherent brittle calcium-containing ceramics. The hybrid material with nanoscale bioceramics embedded within polymer matrix, mimicking bone structures, is expected to provide better osteogenic properties and resorption than the ceramics without polymers. Among all, the deposition of HAp minerals on natural collagen/gelatin phases provides the most similar structures comparing to natural bones. Thus, the HAp-Collagen^{19, 20} and HAp-Gelatin (HAp-Gel)²¹⁻²³ systems that nucleate HAp nanocrystals onto amino-acid residues have been studied in the past decade. HAp-Gel particles possess higher surface tension and greater hydrophilicity than the pure HAp particles; these intrinsic properties rendered improved manipulation and mechanical properties of the HAp-Gel composites, superior to the HAp composites. The studies suggested that the presence of gelatin improves up to three times of the flexural and compressive strength of the bioceramics due to the strong bonding formation between minerals and gelatins.^{24, 25} In addition, deposition of HAp nanoapatites on gelatin molecules imitating microstructures of real bones has shown to provide *in vivo* resorptive capability superior to the pure HAp.^{14, 26}

In our previous study, the aminosilane (enTMOS) served as an effective cross-linker for HAp-Gel modified siloxane (GEMOSIL) nanocomposites.²⁷ The room temperature

processes, including coating, kneading and hardening, form formable paste to create a porous scaffold for bone graft applications. The simple synthesis method not only preserves the nanocrystal structure of HAp-Gel and more importantly, its biocompatibility. The *in vitro* studies showed that the cells proliferate and differentiate on the nanocomposites. The *in vivo* results showed the bone growth around the GEMOSIL nanocomposites further demonstrating its biocompatibility to animals. However, slow setting process and low mechanical properties were the drawbacks for clinical uses.

Recently, in-situ formation of calcium silicate hydrate from calcium hydroxide and silica particles has been shown to reinforce the mechanical properties of Portland cement.^{28,}
²⁹ This pozzolanic reaction occurred during the hydration process at room temperature to produce strong calcium silicate hydrate. In addition to osteogenic properties of calcium silicate, we hypothesize the GEMSOIL could be reinforced in conjunction with in-situ formation of calcium silicate at low temperature for synthesizing mechanical strong and bioactive scaffolds. To the best of our knowledge, in-situ formation of calcium silicate as reinforced phases within biomimetic HAp-Gel systems has been rarely studied. Here we prepared novel GEMOSIL-calcium silicate (GEMOSIL-CS) nanocomposites using in-situ formation of calcium silicate through strong interfacial interactions between Gelatin, silica, and $\text{Ca}(\text{OH})_2$. Effects of calcium hydroxide amounts on both the mechanical properties and microstructures of the bio-inspired composites were studied. Additionally, the osteogenic properties of the composites were evaluated by culturing MC3T3-E1 preosteoblasts. The

study demonstrates that the GEMOSIL-CS composites can be self-hardening within aqueous environment, providing the simple, fast and low cost method to produce a porous scaffold. Most importantly, additional calcium ions provide the degradation and bioactive properties for GEMOSIL-CS composites that can be utilized for tissue engineering applications.

7.2 Materials and Methods

7.2.1 Materials

Hydroxyapatite-gelatin (HAp-Gel) slurry was prepared according to the co-precipitation method²¹. The HAp-Gel slurries were centrifuged at 5000 rpm under 4 °C for 30 minutes to remove excess water. The condensed HAp-Gel was freeze dried at -80 °C overnight followed by lyophilization until dry to form HAp-Gel powder. The Ca(OH)₂ was derived by hydration of CaO calcined.³⁰ Bis[3-(trimethoxysilyl)-propyl]ethylenediamine (enTMOS) was purchased from Gelest, Inc (Morrisville, PA, USA). Pure hydroxyapatite (HAp) powder and Phosphate buffered saline (PH = 7.4) was obtained from Sigma-Aldrich Co. and used without further treatment.

7.2.2 Synthesis of GEMOSIL-CS samples

A 100 mg of HAp-Gel/HAp powder was transferred into a mortar and grinded into fine powder. The predetermined amount of calcium hydroxide powder was added into the mortar and mixed with HAp-Gel powder for 2 minutes. The predetermined amount of enTMOS was added according to Table 7.1 and the mixture was continuously blended for 30 seconds.

Then, 48 μL calcium chloride solution (1 M in phosphate buffer saline, PBS 1X) was added to the mixture to initiate sol gel reaction. At this state, the mixture became viscous and was pressed into a mold to create cylindrical-shaped samples. All samples hardened within 6 minutes. Each sample was coded according to its composition, based on the content of calcium hydroxide and enTMOS (Table 7.1). The samples without calcium hydroxide were also made for comparison (coded as GEMOSIL).

7.2.3 Compressive testing

The cylindrical samples with a 1 : 2 ratio of diameter (3.5 mm) to length (7.0 mm) were prepared for compressive test at two conditions. The samples after mixing were (1) immersed in PBS solution at 37 $^{\circ}\text{C}$ for 2 hours and (2) aged (no PBS) at 37 $^{\circ}\text{C}$ oven for 48 hours. Compressive testing was performed on an Instron machine (model 4204, Canton, MA, USA) with the cross-head speed of 0.5 mm/min. The compressive strength was determined from the maximum strength value on the stress-strain curve. Five samples for each group were used in the compressive testing. The testing results were analyzed by one-way ANOVA and followed by Tukey HDS comparison among each groups.

7.2.4 Thermogravimetric analyzer (TGA) testing

The samples with various compositions (Table 7.1) were synthesized, hardened in the air, and grinded into powders. Each 10 mg of powder was placed on a platinum sample holder, and the sample holder was loaded inside the TA Instruments thermogravimetric

analyzer Q-500 (TA Instrument, New Castle, DE, US). The TGA test was performed from 30 °C to 800 °C with a heating rate of 5 °C/min. Weight changes were recorded versus temperature.

7.2.5 Fourier transform infrared spectroscopy (FTIR)

The samples with various compositions (Table 7.1) were synthesized, hardened in the air, and grinded into powders for FTIR measurements. The chemical interaction and functional groups within nanocomposites were analyzed using the Thermo Scientific Nicolet 670 FTIR (Waltham, MA, USA).

7.2.6 Proliferation assay

The GEMOSIL-CS2 was chosen, based on the result of compressive tests, to further study its influence on preosteoblast proliferation and differentiation. Three experimental groups of materials were investigated, including GEMOSIL-CS2, GEMOSIL, and dishes as received without coating (control). After 1, 3, 5, and 7 days in culture, 40 µL of 3-(4,5-dimethylthiazol-2-yl)-5-(3-carboxymethoxy-phenyl)-2-(4-sulfophenyl)-2H-tetrazolium salt (MTS) reagent (Promega, Madison, WI, USA) was added to each dish containing 400 µL of Alpha Minimal Essential Media (α -MEM), and the dish was incubated for 1 hour at 37 °C under a humidified atmosphere of 5% CO₂. From each dish, 100 µL of MTS solution was transferred into each well of the 96 well plates. Each sample was triplicated and repeated three times. The absorbance of each well at 490 nm was measured using a microplate reader

(Microplate Reader 550, Bio-Rad laboratories, Philadelphia, PA USA). Relative cell numbers were quantified on the basis of the concentration of the formazan product of MTS. Coated dishes with GEMOSIL-CS2 and GEMOSIL without cells were used as a blank (negative control).

7.2.7 Picrosirious staining

MC3T3-E1 cells cultured on both GEMOSIL-CS2 and GEMOSIL coated glass slide (Corning, Corning, NY USA) and differentiated with osteogenic media (α -MEM,) for 1, 4 and 7 days respectively. Cells were fixed in a solution of 10% formalin for 30 minutes. After washing with PBS, cells were incubated in 0.1% (w/v) Sirius red F3B in saturated Picric acid solution (Electron Microscopy Sciences, Hatfield, PA, USA) for 1 hour at room temperature. Slide glasses were dehydrated in an ethanol-graded series (60, 70, 80, 90, and 100%) for three minutes each and allowed to leave in xylene until mount. Each sample was triplicated. The sections were analyzed using a Nikon microscope equipped with filters to provide polarized illumination. Collagen fiber images were obtained with a 40x objective lens, recorded on a digital camera (DP11, Olympus USA, Center Valley, PA USA), equipped separately on microscope for color image acquisition.

7.2.8 Alizarin red staining

MC3T3-E1 Cells were cultured on both GEMOSIL-CS2 and GEMOSIL coated dishes and differentiated with osteogenic media for 1, 4, 7, 14, and 21 days respectively. Osteogenic

media was composed of Alpha Minimal Essential Media (α -MEM) with the addition of 10mM of b-glycerophosphate (Sigma) and ascorbic acid at 0.2 mM (Sigma). After washing with PBS, the cells were fixed for 10 minutes in formalin, washed, stained with 40 mM Alizarin Red (Acros Organics, Geel, Belgium) at pH 4.2 for 10 min, rinsed with deionized water 6 times and air dried. Stained plates were scanned using HP scanner (dpi or specific info). Simple method using photoshop software was applied to measure and analyze the surface color intensity of Alizarin red staining. The quantification results of mineralization characteristics were derived from color differences (δ) by CIELAB method²⁷. Briefly, The characteristic values and standard deviations for L, a*, and b* were calculated using the Photoshop software (Adobe System Inc., CA). For each material group, a formula to calculate the mineralization's characteristics was a color difference between the with and the without cell dishes, $\delta = ((L-L_o)^2+(a^*-a^*_o)^2+(b^*-b^*_o)^2)^{1/2}$ where (L, a*, b*) and (L_o, a*_o, b*_o) were tristimulus values for the having cell and non-cell dish, respectively. The mean δ were compared among three groups using one way ANOVA and Tukey-Kramer's HSD. IBM SPSS Statistics 19 (SPSS Inc., Chicago, IL, US) was used for all statistical analysis.

7.2.9 Scanning and transmission electron microscopy (SEM and TEM)

The cell culture samples for SEM were prepared by dehydration, fixation and critical point dry. SEM was performed on a Hitachi S-4700 using an accelerated voltage of 15 kV. The Energy-dispersive X-ray spectroscopy (EDX) has been used to determine the composition of mineral nodules. For TEM, The samples were prepared according to the

methods provided by the Microscopic Services Laboratory (MSL) at the University of North Carolina.³¹ Then, the samples were stained with uranyl acetate and lead citrate, and observed using a LEO EM-910 transmission electron microscope operating at 80 kV (Carl Zeiss SMT, Peabody, MA, USA).

7.3 Results

7.3.1 Physical properties and characterizations

The compressive testing results showed the reinforced effects by incorporation of gelatin and calcium hydroxide after 48 hours drying at 37 °C (Figure 7.1). By incorporation of gelatin, the compressive strength of scaffolds can be enhanced from 38.3 MPa of HAp-CS2 to 93.6 MPa of GEMOSIL-CS2 by 2.44 times. The reinforced effect of calcium hydroxide is shown by comparing GEMOSIL with GEMOSIL-CS2 that compressive strength increased from 43.7 to 93.6 MPa by 2.14 times. The strength increases with the amount of calcium hydroxide. ANOVA shows significant difference between the compressive strength of different groups ($p < 0.01$) and both incorporation of gelatin and calcium hydroxide showed the significant reinforced effects on compressive strength of GEMOSIL nanocomposites.

Before setting, GEMOSIL samples appeared as a formable paste with moldable and injectable properties. The setting time of GEMOSIL scaffolds can be adjusted between 3 to 6 minutes and it can be hardened at ambient or within PBS solution. The strength increases with the amount of calcium hydroxide and reaches the maximum of 28.5 MPa for

GEMOSIL-CS2 samples after 2 hours setting in PBS at 37 °C (Figure 7.2). This value was around 3.1 times higher than the samples without Ca(OH)₂ (GEMOSIL) after 2 hours setting in PBS. The reinforced effect decreases from 3.1 times at 2 hours to 2.14 times at 48 hours indicating the faster initial setting of GEMOSIL-CS. Incorporation of calcium hydroxide could accelerate the setting process of GEMOSIL-CS samples.

TGA results are shown in Figure 7.3 that absorbed water inside the GEMOSIL and GEMOSIL-CS nanocomposites could not be removed completely until 200 °C. The weight loss of GEMOSIL-CS was attributed to the thermal degradation of various compositions including gelatin (300 - 560 °C),³² alkyl groups on enTMOS (400 - 500 °C),²⁷ dehydration due to further condensation reaction (400 - 600 °C) and calcium hydroxide (550 - 650 °C).³³ ³⁴ The GEMOSIL sample showed continuous weight drop from 300-600 °C. The GEMOSIL-CS1 showed the continuous weight drop until 450 °C, followed by gradual weight drop until 600 °C with the final weight loss. The weight drop even ceased at 450 °C for GEMOSIL-CS2 samples until abruptly dropped at 600 °C indicating the existence of the residual calcium hydroxide within the scaffolds. The remained mineral contents after TGA testing can be derived from TGA data (Figure 7.3) and are a close match to the theoretical amounts as shown in Figure 7.4.

As shown in Figure 7.5, the FTIR spectrum of GEMOSIL nanocomposites containing characteristic peaks resembled both spectrum of HAp-Gel and enTMOS. GEMOSIL

nanocomposites showed the typical hydroxyl (OH) peak at 3361 cm^{-1} , the typical amide peak at 1645 cm^{-1} , and the methylene ($-\text{CH}_2-$) bending at 1456 cm^{-1} as shown in the HAp-Gel²¹. There were also vinyl (C-H) stretch peak at 2939 cm^{-1} , amide peak at 1645 cm^{-1} , the amine (C-N) stretch at 1202 cm^{-1} , the siloxane (Si-O-C) at 1090 cm^{-1} , and siloxane (Si-O-Si) at 1024 cm^{-1} as revealed in enTMOS.³⁵

The amide groups have been used to confirm the formation of chemical bonding between calcium ions with gelatin and silica.³⁶ For GEMOSIL-CS2 sample, the amide I band blue shifts from 1645 to 1648 cm^{-1} and the amide III red shifts from 1202 to 1185 cm^{-1} where GEMOSIL-CS1 showed the similar shifts. The peak shift increased as the calcium ion amount increased. The dramatic blue shift of siloxane band from 919 cm^{-1} to 965 cm^{-1} indicated the formation of Si-O-Ca chemical bonding of calcium silicate.³⁷ The peak positions were the same regardless of the amount of calcium hydroxide.

The x-ray diffraction study was conducted to examine of formation of calcium silicate. Figure 7.6 showed the XRD diagram of GEMOSIL and GEMOSIL-CS after drying at $37\text{ }^\circ\text{C}$ for 48 hours. The peaks at 26.1° and 32.1° represented the hydroxyapatite crystals and intensity decreases as increase of calcium hydroxide amount. The peaks at 18.2° , 28.0° , 34.2° and 47.3° represented the calcium hydroxide and the intensity increase as increase of the calcium hydroxide amounts. The peak at 29.5° indicated the formation of calcium silicate hydrate which remains the similar intensity regardless of calcium hydroxide amount. The

broad peak at around 22.2° represented the silica phase within GEMOSIL samples and it disappeared in GEMOSIL-CS samples, which could be due to the formation of calcium silicate.

7.3.2 *In vitro* osteogenic properties

For the purpose of bone regeneration, the material should be biocompatible and allow population of the extracellular matrix. To this end, cytocompatibility was assessed by MTS assay, culturing MC3T3-E1 cells on the GEMOSIL-CS coated dishes. Mineralization also was evaluated by collagen detection and nodule formation after initiating osteogenic differentiation with defined media.

Cell proliferative potential on the material coated dish was analyzed by MTS assay. Figure 7.7 shows the resultant growth curves of MC3T3-E1 cells. Cells on both GEMOSIL-CS2 and GEMOSIL increased their numbers up to 7 days. Cells on GEMOSIL-CS2 coating showed higher proliferative potential than those on GEMOSIL ($P < 0.01$), but less potential than those of the control between days 1 and 7 ($P < 0.01$). There was no difference at day 7 between the control and GEMOSIL-CS2 ($P < 0.01$).

Osteoblasts produce collagen fibers prior to apatite deposition during bone matrix formation. Here, we analyzed the ability of MC3T3-E1 cells to secrete a collagenous matrix on 1, 4 and 7 days (early time points) of culture on both GEMOSIL-CS2 and GEMOSIL

coated dishes. Polarized light microscopic image of MC3T3-E1 cells displayed collagen fibers as short and stretched linear form with orange and yellow-reddish color. For both materials, the collagen secreted on day 1 only showed few fibers, but the amount increased on day 4. The fiber became thicker and appeared more reticular form on the day 7 (Figure 7.8).

The deposition of calcified matrix was analyzed by Alizarin Red staining. Culture dishes were stained with Alizarin red at 1, 4, 7, 14, and 21 days for the evidence of mineralization. Even though the calcium deposition was significantly increased after 7 days of culture on both GEMOSIL-CS2 and GEMOSIL, more calcium deposition was observed on the GEMOSIL-CS2 culture than GEMOSIL culture on day 21 (Figure 7.9). Mineralization was not detected during first week of culture. However, dense aggregation form was examined after a week as proceeding nodule formation. By day 21, differentiated MC3T3-E1 cell culture represented mineralized nodules, and their appearance differs in GEMOSIL-CS2 and GEMOSIL culture. The surface color intensity of Alizarin red staining was increased from day 1 to 21. These mineralization characteristics of control, GEMOSIL and GEMOSIL-CS2 can be derived from quantitative color differences (δ) by CIELAB method (Figure 7.10).

SEM and TEM were performed on both GEMOSIL-CS2 and GEMOSIL after 4 and 7 days of culture. SEM images confirmed the MTS proliferation results that GEMOSIL-CS2

coating showed higher proliferative potential than those on GEMOSIL at both 4 and 7 days (Figure 7.11). Especially for GEMOSIL-CS2 at 7 days, the formation of collagen fibers has been observed around the cells (Figure 7.12a). High magnification image clearly indicated small particles of hydroxyapatite were attached on the surface of collagen fiber indicating mineralization. (Figure 7.12b) TEM images also showed the cross-sectional view of MC3T3-E1 cells, collagen fibers, and mineral particles in culture after 7 days. The cells contacted with materials intimately indicating the biocompatibility of GEMOSIL-CS2 (Figure 7.12c). The formation of collagen fibers and mineral particles also provided the evidence of mineralization in early stage of osteogenic differentiation (Figure 7.12d).

7.4 Discussion

7.4.1 Physical properties and characterizations

The incorporation of gelatin and calcium hydroxide both show the reinforced effects on the mechanical property and solidification of GEMOSIL-CS scaffolds. By incorporation gelatin (GEMOSIL-CS), the compressive strength can be enhanced by 2.44 times compared to HAp only samples (HAp-CS2). This phenomenon has been attributed to the formation of chemical bonding between gelatin with silica and gelatin with calcium ions. First, the hydrogen bonding properties of polyols could be used to induce physical cross-linking.³⁸ Thus, silica species have utilized as a cross-linking agent for gelatin since they were shown to interact through both electrostatic interactions and hydrogen bonding.³⁹ Second, the carboxylic group of gelatin at high pH environment tends to be ionic and form chemical bond

with calcium ions.⁴⁰ Thus, these two gelatinous interactions within the GEMOSIL-CS composites contribute, partially, to the increase of compressive strength.

It is known that the properties of composite materials are not just the sum of the individual contributions from both phases; the role of the inner interfaces is considered to be predominant in determining the overall properties. The bonding between different phases has been shown as one of most critical factors to the reinforced effect of composites. Thus, in-situ formation of chemical bonding between gelatin, silica and calcium hydroxide significantly enhances the structure and property of GEMOSIL-CS composites. It has been demonstrated that the short term and long term strength of Portland cement system can be greatly enhanced by formation of calcium silicate between silica and calcium hydroxide.^{28, 34} Silica behaves as an activator to promote pozzolanic reaction with calcium hydroxide to form calcium silicate. Thus, in-situ formation of calcium silicate from calcium hydroxide and silica has been identified to further enhance the mechanical properties of GEMOSIL-CS nanocomposites.

The setting process of the GEMOSIL-CS composites is mainly attributed to the catalytic accelerated sol-gel reaction even within biological fluid. During synthesis, all samples consisting of calcium chloride solution hardened within 6 min. With increasing calcium chloride concentration, the setting time of the cement could be shortened, reaching 3 min. The calcium chloride solution has been reported to disturb stability of colloidal system

and trigger gelation of sol-gel reaction. The basic environment due to leaching of calcium hydroxide also accelerates the hydrolysis and condensation of enTMOS sol-gel reaction.

From the TGA results, the distinct pattern between GEMOSIL-CS and GEMOSIL samples indicates the chemical bonding formation between gelatin, aminosilica and calcium hydroxide. The weight loss during 450 - 600 °C mainly contributes to the thermal degradation of gelatin (300 - 560 °C) and alkyl groups on aminosilica (400 - 500 °C). The TGA weight loss delays or stops in GEMOSIL-CS samples during 450 - 600 °C and then followed by thermal degradation of calcium hydroxide at 600 °C which is delayed about 50 - 70 °C.³³ This distinct weight loss pattern of GEMOSIL-CS samples attributes to the interfacial bonding between within nanocomposites. The chemical bondings between gelatin, calcium ions and silica slow down the weight loss of GEMOSIL-CS1 and even delayed the weight loss in GEMOSIL-CS2 samples. This phenomenon indicates the formation of chemical bonding increases with the amount of calcium ions, which is consistent with the reinforced effects of calcium ions by compressive testing.

Gelatin consists of varying amounts of 18 amino acids, of which glycine, proline and hydroxyproline are most abundant.⁴¹ Our previous FTIR studies has shown the amino acid residues contained in HAp-Gel structure could make a possible association with silanol groups through hydrogen bonding.³⁵ In the same time, the amide I peak at 1645 cm⁻¹ and amine III stretch peak at 1202 cm⁻¹ are two characteristic peaks of gelatin which represent the

amines on the backbones. Blue shift of the amide I and red shift of the amine III band indicate the chemical bonding formation between calcium ions of calcium hydroxide and gelatin. The calcium ions have been found to form the chemical bonding with amide and carboxyl of gelatin during the preparation of gelatin-calcium phosphate composites.⁴² It is also known the carboxylic group of gelatin at high pH environment tends to be ionic and form chemical bond with calcium ions. Also, Matsuyama and Young⁴³ claimed that a broad range of anionic, cationic and neutral polymers can be intercalated in the C-S-H layers depending on the Ca/Si ratio of the solid. Minet demonstrated that C-S-H can accommodate small sized organic groups in the interlayer space, directly linked to silicate chains.⁴⁴ These results all pointed out the binding forces between gelatin with calcium and silicate. Thus, incorporation of gelatin help to reinforce the composites structures with these chemical bonding.

The siloxane peak at 919 cm^{-1} is one of characteristic peak of enTMOS. The blue shifts of the siloxane peak to 965 cm^{-1} indicated the formation of Si-O-Ca, one of characteristic peak of calcium silicate hydrate. The vibrational bands observed in the range of $850\text{-}1000\text{ cm}^{-1}$ of IR spectra can be attributed to Si-O-Ca bonds. In the same time, the gradually decreasing IR absorption intensities for Si-O stretching vibrations at 1024 cm^{-1} also indicated CS phase formation during the percolation reactions.³⁴ Basically, the cement paste matrix is a porous material composed of calcium hydroxide, aluminates and unhydrated cement embedded into an amorphous nanostructured hydration product, the so called C-S-H

(Calcium Silicate Hydrate) gel. This gel is the most important hydration product of the cement paste matrix, not only because it is the most abundant component (50-70% by volume), but also because of its exceptionally good mechanical properties. It is a known technique for Portland cement to enhance its mechanical stability utilizing the silica to react with Ca(OH)_2 and form the calcium silicate due to the pozzolanic reaction.⁴⁵ The researchers have shown that silica increases the strength of the cement paste about a 30% in cured samples and more than a 100% in the asymptotically leached ones.^{28, 46} Thus, in-situ formation of calcium silicate provides a promising method for scaffold synthesis and reinforcement.

The X-ray diffraction result confirmed with the FTIR results that amorphous calcium silicate turned into dicalcium silicate hydrate after drying process. The occurring peak at 29.5° indicated the formation of crystalline dicalcium silicate hydrate structures. The formation of crystalline structure originated from the pozzolanic reaction between basic Ca(OH)_2 and acidic siloxane. The high surface area and high reactivity of sol-gel derived siloxane promotes the formation the crystalline dicalcium silicate hydrate at low temperature which enhances the mechanical stability of Portland cement and also the present system. The residual Ca(OH)_2 has been detected from X-ray results and it can leach calcium ions to affect *in vitro* osteogenic properties.

The residual Ca(OH)_2 within the composites causes the leaching of calcium ions, which provides two characteristic properties of GEMOSIL-CS composites. First, the degradation rate can be further enhanced due to the leaching of calcium ions. The formation and leaching of calcium hydroxide have been found happened in the Portland cement phases. Although the additives of silica particles will react with calcium hydroxide as mentioned above, the Ca ions could be released due to the abundant amount of calcium hydroxide. The degradation rate of GEMOSIL-CS composites approach 15 wt% at 14 days and 25 wt% at 28 days (data not shown here), which is higher than that of the GEMOSIL only composites. Thus, the leaching of Ca ions can further enhance degradation. Second, the leaching of calcium hydroxide also provides the abundant Ca ions that might affect osteogenic properties as shown in the present *in vitro* studies.

7.4.2 *In vitro* osteogenic properties

To meet the requirements as bone substitutes, the material should be biocompatible and allow population of the both organic and inorganic extracellular matrix. Osteoblast attachment to collagen is mediated through integrins and it transduces kinase signaling pathways supporting osteoblast proliferation and bone growth.⁴⁷ Cells on the GEMOSIL-CS2 showed less proliferative potential than control for 3 days of culture, but eventually will fully confluent in culture dish after 7 days of culture. The delay of cell growth is possibly caused by initial calcium leaching from the substrate surface, which may affect cell attachment. Increased calcium (Ca) level eluted from the coated GEMOSIL-CS2 would affect to the

degree of proliferation since Ca ions was known to play a very important role in osteoblast proliferation from previous studies.⁴⁸ Eklou-Kalonji et al. reported that extracellular calcium level involved in the regulation of proliferation, collagen synthesis, and the expression of osteoblast phenotype markers.⁴⁹

Collagen has the capacity to mineralize during osteogenic differentiation. It is secreted from osteoblasts and serves as biomimetic material for the bone mineralization. In this study, we observed the secretion of collagen on both GEMOSIL-CS2 and GEMOSIL culture in early time point. After one day of differentiation, very few fibrillar collagens were observed, whereas density of fibrillar collagen was increasing on day 4 and more on day 7 on both GEMOSIL-CS2 and GEMOSIL culture system throughout the early time course of this experiment (7 days). Unlikely on day 1 and 4, collagen fibrils seen in Figure 7.8 on day 7 appeared to become thicker and to align nearly orthogonally to each other that also appeared in the SEM results.

Alizarin red is routinely used for staining deposited calcium nodules during osteogenic differentiation. Scanned and light microscopic image was acquired to observe the detailed calcium nodule formation. The nodules in GEMOSIL-CS2 culture appeared darker and larger particles, whereas the shape of nodules seemed to be linearly connected in GEMOSIL culture. The higher degree of nodule formation in GEMOSIL-CS2 culture can possibly be affected by the leaching calcium ions in culture system.

Both SEM and TEM images further confirmed that the MC3T3-E1 cells can secrete mature collagen and form calcified nodules during osteogenic differentiation on GEMOSIL and GEMOSIL-CS2. Collagen matrix secreted by MC3T3-E1 cells after initiating osteogenic differentiation is an essential platform for the mineralization. Small hydroxyapatite particles along with collagen fibril were able to be observed by SEM at high magnification. This collagen and mineral interaction will be implicated to design biomimetic mineralized collagen for the functional bone matrix formation. The TEM results of GEMOSIL-CS2 revealed that there were abundant cytoplasmic secrets, which indicated by many rough endoplasmic reticulum implying accelerated osteogenic differentiation. It confirmed that the dark particles from Alizarin red results associated with collagen fiber to precede mineralization. The mineralization process possibly affected by the calcium ion leached from GEMOSIL-CS2. As we mentioned in earlier part, calcium ion could stimulate both cell proliferation and differentiation directly or indirectly. Therefore, the mechanism of calcium ions from GEMOSIL-CS2 coating needs to be explored on the biological system in the future study.

7.5 Conclusion

The present study demonstrates a new bioactive scaffold made of in-situ hybridization of calcium silicate and hydroxyapatite-gelatin nanocomposites. The inherent interfacial binding between gelatin, calcium silica and aminosilica contributed to the mechanical integrity. The in-situ formation calcium silicate has enhanced the mechanical strength of

nanocomposites. In the same time, MC3T3-E1 cells have been shown to proliferate and differentiate better on the GEMOSIL-CS than on GEMOSIL culture system and calcium ion leached from GEMOSIL-CS culture system might play a key role. Therefore, the new GEMOSIL-CS nanocomposites could provide promising opportunities for tissue engineering applications.

7.6 References

1. Langer, R.; Vacanti, J. P., Tissue Engineering. *Science* 1993, 260, (5110), 920-926.
2. Hutmacher, D. W., Scaffolds in tissue engineering bone and cartilage. *Biomaterials* 2000, 21, (24), 2529-2543.
3. Griffith, L. G.; Naughton, G., Tissue engineering - Current challenges and expanding opportunities. *Science* 2002, 295, (5557), 1009-+.
4. Yang, S. F.; Leong, K. F.; Du, Z. H.; Chua, C. K., The design of scaffolds for use in tissue engineering. Part 1. Traditional factors. *Tissue Engineering* 2001, 7, (6), 679-689.
5. Albrektsson, T.; Johansson, C., Osteoinduction, osteoconduction and osseointegration. *European Spine Journal* 2001, 10, S96-S101.
6. Mistry, A. S.; Mikos, A. G., Tissue engineering strategies for bone regeneration. In *Regenerative Medicine II: Clinical and Preclinical Applications*, Springer: New York, 2005; Vol. 94, pp 1-22.
7. Mano, J. F.; Sousa, R. A.; Boesel, L. F.; Neves, N. M.; Reis, R. L., Bloinert, biodegradable and injectable polymeric matrix composites for hard tissue replacement:

- state of the art and recent developments. *Composites Science and Technology* 2004, 64, (6), 789-817.
8. Drotleff, S.; Lungwitz, U.; Breunig, M.; Dennis, A.; Blunk, T.; Tessmar, J.; Gopferich, A., Biomimetic polymers in pharmaceutical and biomedical sciences. *European Journal of Pharmaceutics and Biopharmaceutics* 2004, 58, (2), 385-407.
 9. Seal, B. L.; Otero, T. C.; Panitch, A., Polymeric biomaterials for tissue and organ regeneration. *Materials Science & Engineering R-Reports* 2001, 34, (4-5), 147-230.
 10. Hubbell, J. A., Synthetic biodegradable polymers for tissue engineering and drug delivery. *Current Opinion in Solid State & Materials Science* 1998, 3, (3), 246-251.
 11. Zioupos, P.; Currey, J. D., Changes in the stiffness, strength, and toughness of human cortical bone with age. *Bone* 1998, 22, (1), 57-66.
 12. Jarcho, M.; Kay, J. F.; Gumaer, K. I.; Doremus, R. H.; Drobeck, H. P., Tissue, Cellular and Subcellular Events at a Bone-Ceramic Hydroxylapatite Interface. *Journal of Bioengineering* 1977, 1, (2), 79-92.
 13. Denissen, H. W.; Degroot, K.; Makkes, P. C.; Vandenhooff, A.; Klopper, P. J., Tissue-Response to Dense Apatite Implants in Rats. *Journal of Biomedical Materials Research* 1980, 14, (6), 713-721.
 14. Ding, S. J.; Wei, C. K.; Lai, M. H., Bio-inspired calcium silicate-gelatin bone grafts for load-bearing applications. *Journal of Materials Chemistry* 21, (34), 12793-12802.
 15. Vallet-Regi, M.; Ragel, C. V.; Salinas, A. J., Glasses with medical applications. *European Journal of Inorganic Chemistry* 2003, (6), 1029-1042.

16. Salinas, A. J.; Roman, J.; Vallet-Regi, M.; Oliveira, J. M.; Correia, R. N.; Fernandes, M. H., In vitro bioactivity of glass and glass-ceramics of the $3\text{CaO} \cdot \text{P}_2\text{O}_5\text{-CaO} \cdot \text{SiO}_2\text{-CaO} \cdot \text{MgO} \cdot 2\text{SiO}_2$ system. *Biomaterials* 2000, 21, (3), 251-257.
17. Catauro, M.; Laudisio, G.; Costantini, A.; Fresa, R.; Branda, F., Low temperature synthesis, structure and bioactivity of $2\text{CaO} \cdot 3\text{SiO}_2$ glass. *Journal of Sol-Gel Science and Technology* 1997, 10, (2), 231-237.
18. Alemany, M. I.; Velasquez, P.; de la Casa-Lillo, M. A.; De Aza, P. N., Effect of materials' processing methods on the 'in vitro' bioactivity of wollastonite glass-ceramic materials. *Journal of Non-Crystalline Solids* 2005, 351, (19-20), 1716-1726.
19. Du, C.; Cui, F. Z.; Zhu, X. D.; de Groot, K., Three-dimensional nano-HAp/collagen matrix loading with osteogenic cells in organ culture. *Journal of Biomedical Materials Research* 1999, 44, (4), 407-415.
20. Itoh, S.; Kikuchi, M.; Takakuda, K.; Nagaoka, K.; Koyama, Y.; Tanaka, J.; Shinomiya, K., Implantation study of a novel hydroxyapatite/collagen (HAp/Col) composite into weight-bearing sites of dogs. *Journal of Biomedical Materials Research* 2002, 63, (5), 507-515.
21. Chang, M. C.; Ko, C. C.; Douglas, W. H., Preparation of hydroxyapatite-gelatin nanocomposite. *Biomaterials* 2003, 24, (17), 2853-2862.

22. Kim, H. W.; Kim, H. E.; Salih, V., Stimulation of osteoblast responses to biomimetic nanocomposites of gelatin-hydroxyapatite for tissue engineering scaffolds. *Biomaterials* 2005, 26, (25), 5221-5230.
23. Kim, H. W.; Song, J. H.; Kim, H. E., Nanoriber generation of gelatin-hydroxyapatite biomimetics for guided tissue regeneration. *Advanced Functional Materials* 2005, 15, (12), 1988-1994.
24. Shie, M. Y.; Chen, D. C. H.; Wang, C. Y.; Chiang, T. Y.; Ding, S. J., Immersion behavior of gelatin-containing calcium phosphate cement. *Acta Biomaterialia* 2008, 4, (3), 646-655.
25. Bigi, A.; Bracci, B.; Panzavolta, S., Effect of added gelatin on the properties of calcium phosphate cement. *Biomaterials* 2004, 25, (14), 2893-2899.
26. Radev, L.; Hristov, V.; Fernandes, M. H. V.; Salvado, I. M. M., Organic/Inorganic bioactive materials Part IV: In vitro assessment of bioactivity of gelatin-calcium phosphate silicate/wollastonite hybrids. *Central European Journal of Chemistry* 8, (2), 278-284.
27. Chiu, C. K., Ferreira, J., Luo, T. Z. M., Geng, H., Lin, F. C., Ko, C. C., Direct scaffolding of biomimetic hydroxyapatite-gelatin nanocomposites using aminosilane cross-linker for bone regeneration. *Journal of Materials Science: Materials in Medicine* 2012, DOI: 10.1007/s10856-012-4691-6.

28. Dolado, J. S.; Campillo, I.; Erkizia, E.; Ibanez, J. A.; Porro, A.; Guerrero, A.; Goni, S., Effect of nanosilica additions on Belite Cement pastes held in sulfate solutions. *Journal of the American Ceramic Society* 2007, 90, (12), 3973-3976.
29. Ye, Q.; Zhang, Z. N.; Kong, D. Y.; Chen, R. S., Influence of nano-SiO₂ addition on properties of hardened cement paste as compared with silica fume. *Construction and Building Materials* 2007, 21, (3), 539-545.
30. Kikuchi, M., Cho, S-B, Tanaka, J, Koyama, Y, Kobayashi, T, Takakuda, K, Akao, M, Preparation and biocompatibility of beta -tricalcium-phosphate /copolymerized-poly-L-lactide composite. *Journal of the Japan Society of Powder and Powder Metallurgy* 1998, 45, 36-40.
31. Ferreira JR, H. M., Zhang L, Park Y, Samulski RJ, Hu WS, Ko CC., Three-dimensional multipotent progenitor cell aggregates for expansion, osteogenic differentiation and 'in vivo' tracing with AAV vector serotype 6. *Gene Ther* 2012, doi: 10.1038/gt.2012.16.
32. Ward, A. G., *The science and technology of gelatin*. Academic Press: London, 1977.
33. Valenti, G. L.; Cioffi, R., Quantitative-Determination of Calcium Hydroxide in the Presence of Calcium Silicate Hydrates - Comparison between Chemical-Extraction and Thermal-Analysis. *Journal of Materials Science Letters* 1985, 4, (4), 475-478.
34. Bjornstrom, J.; Martinelli, A.; Matic, A.; Borjesson, L.; Panas, I., Accelerating effects of colloidal nano-silica for beneficial calcium-silicate-hydrate formation in cement. *Chemical Physics Letters* 2004, 392, (1-3), 242-248.

35. Luo, T. J. M.; Ko, C. C.; Chiu, C. K.; Llyod, J.; Huh, U., Aminosilane as an effective binder for hydroxyapatite-gelatin nanocomposites. *Journal of Sol-Gel Science and Technology* 53, (2), 459-465.
36. Farhat, I. A.; Orset, S.; Moreau, P.; Blanshard, J. M. V., FTIR study of hydration phenomena in protein-sugar systems. *Journal of Colloid and Interface Science* 1998, 207, (2), 200-208.
37. Baciú, D.; Simitzis, J., Synthesis and characterization of a calcium silicate bioactive glass. *Journal of Optoelectronics and Advanced Materials* 2007, 9, (11), 3320-3324.
38. Fujitsu, M.; Hattori, M.; Tamura, T., Effects of hydroxy compounds on gel formation of gelatin. *Colloid and Polymer Science* 1997, 275, (1), 67-72.
39. Retuert, J.; Martinez, Y.; Quijada, R.; Yazdani-Pedram, M., Highly porous silica networks derived from gelatin/siloxane hybrids prepared starting from sodium metasilicate. *Journal of Non-Crystalline Solids* 2004, 347, (1-3), 273-278.
40. Ren, L.; Tsuru, K.; Hayakawa, S.; Osaka, A., Incorporation of Ca²⁺ ions in gelatin-siloxane hybrids through a sol-gel process. *Journal of the Ceramic Society of Japan* 2001, 109, (5), 406-411.
41. A., V., *The macromolecular chemistry of gelatin*. Academic Press: New York, 1964.
42. Fujishiro, Y.; Takahashi, K.; Sato, T., Preparation and compressive strength of alpha-tricalcium phosphate/gelatin gel composite cement. *Journal of Biomedical Materials Research* 2001, 54, (4), 525-530.

43. Matsuyuma, H.; Young, J. F., Synthesis of calcium silicate hydrate/polymer complexes: Part I. Anionic and nonionic polymers. *Journal of Materials Research* 1999, 14, (8), 3379-3388.
44. Minet, J.; Abramson, S.; Bresson, B.; Franceschini, A.; Van Damme, H.; Lequeux, N., Organic calcium silicate hydrate hybrids: a new approach to cement based nanocomposites. *Journal of Materials Chemistry* 2006, 16, (14), 1379-1383.
45. Jo, B. W.; Kim, C. H.; Tae, G. H.; Park, J. B., Characteristics of cement mortar with nano-SiO₂ particles. *Construction and Building Materials* 2007, 21, (6), 1351-1355.
46. Gaitero, J. J.; Campillo, I.; Guerrero, A., Reduction of the calcium leaching rate of cement paste by addition of silica nanoparticles. *Cement and Concrete Research* 2008, 38, (8-9), 1112-1118.
47. Raucci, A.; Bellosta, P.; Grassi, R.; Basilico, C.; Mansukhani, A., Osteoblast proliferation or differentiation is regulated by relative strengths of opposing signaling pathways. *Journal of Cellular Physiology* 2008, 215, (2), 442-451.
48. Maeno, S.; Niki, Y.; Matsumoto, H.; Morioka, H.; Yatabe, T.; Funayama, A.; Toyama, Y.; Taguchi, T.; Tanaka, J., The effect of calcium ion concentration on osteoblast viability, proliferation and differentiation in monolayer and 3D culture. *Biomaterials* 2005, 26, (23), 4847-4855.
49. Eklou-Kalonji, E.; Denis, I.; Lieberherr, M.; Pointillart, A., Effects of extracellular calcium on the proliferation and differentiation of porcine osteoblasts in vitro. *Cell and Tissue Research* 1998, 292, (1), 163-171.

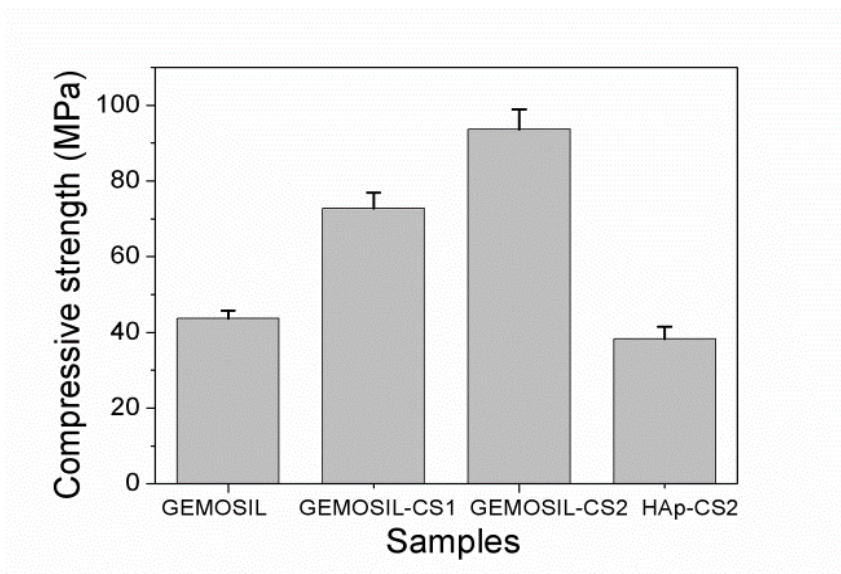


Figure 7.1 Compressive strength of GEMOSIL nanocomposites aging in 37 °C oven for 48 hours after mixing. The strength increases with the amount of calcium hydroxide. ANOVA shows significant difference between the compressive strength of different groups ($p < 0.01$).

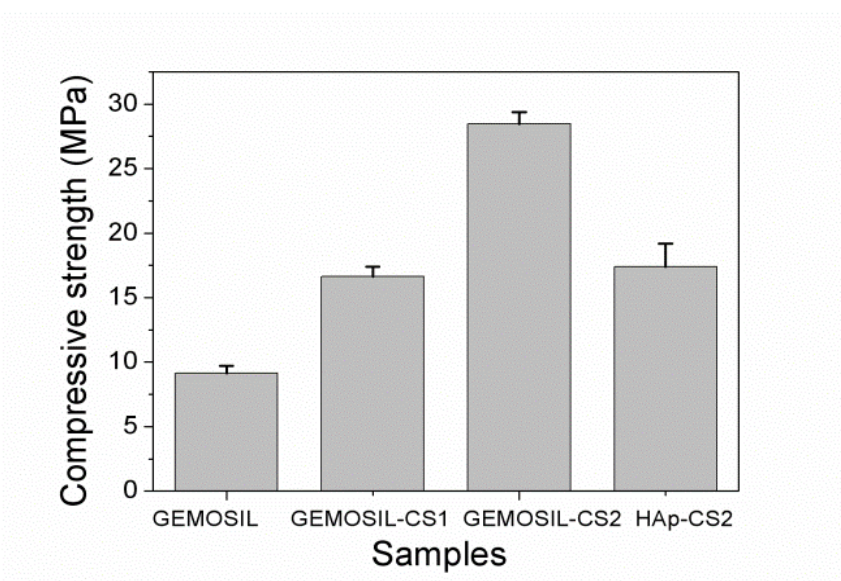


Figure 7.2 Compressive strength of GEMOSIL nanocomposites soaking in 37 °C PBS for 2 hours after mixing. The strength increases with the amount of calcium hydroxide and reaches the maximum of 28.5 MPa for GEMOSIL-CS2 samples.

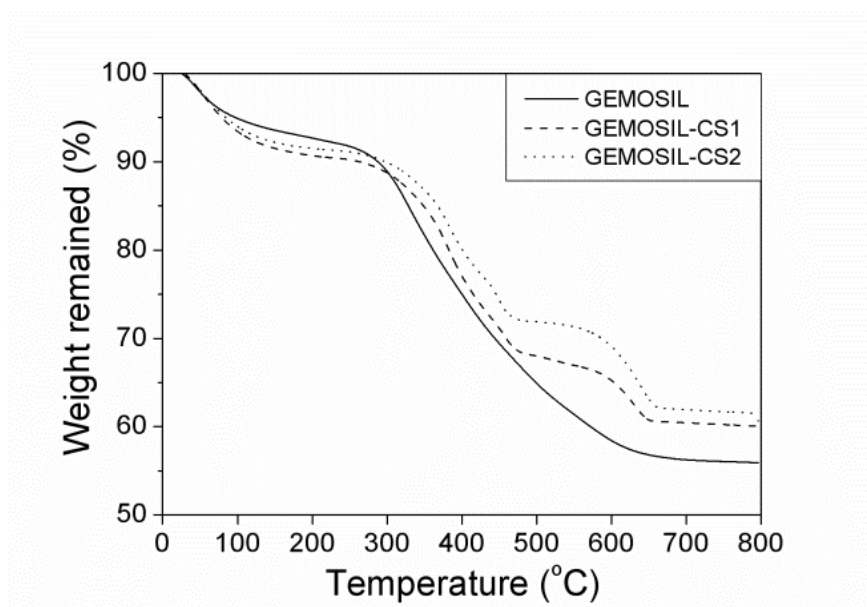


Figure 7.3 TGA results showed the weight loss versus temperature. Distinct weight drop patterns are attributed to the degradation of water, gelatin, alkyl group and calcium hydroxide.

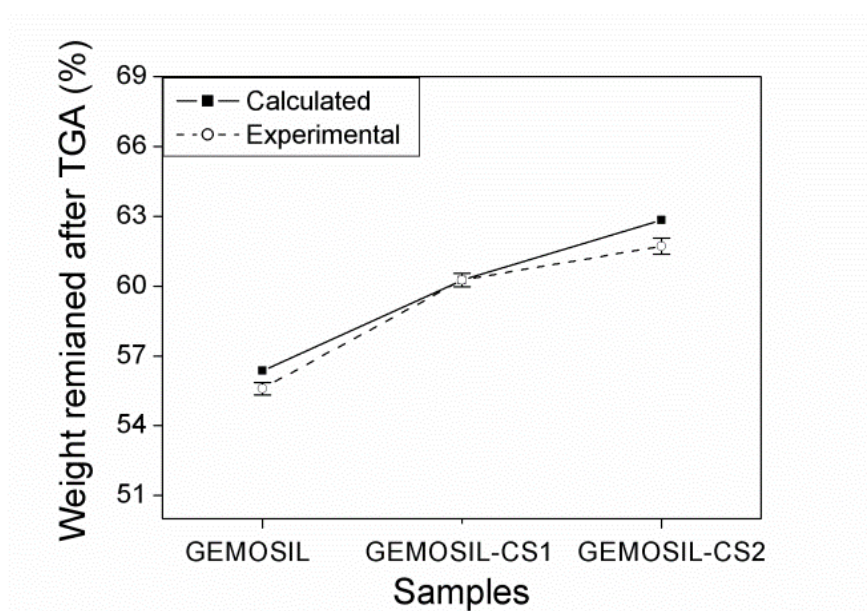


Figure 7.4 Theoretically calculated and experimentally measured weight remained of GEMOSIL samples after TGA 800 °C treatment. Small differences between these two measures suggest the uniform distribution of each phase within nanocomposites.

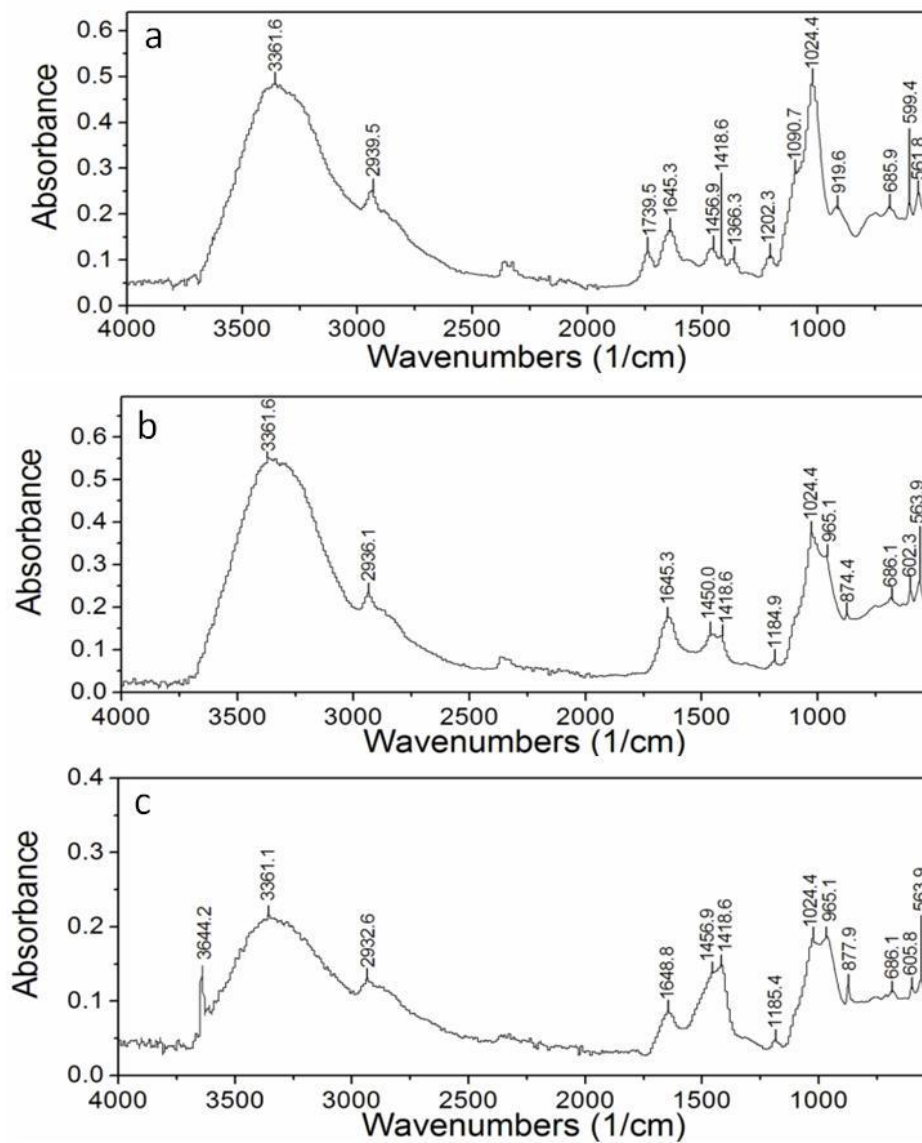


Figure 7.5 FTIR spectrum of GEMOSIL nanocomposites. (a) GEMOSIL (b) GEMOSIL-CS1 (c) GEMOSIL-CS2. The FTIR spectrum containing characteristic peaks resembled both spectrum of HAp-Gel, enTMOS and calcium silicate.

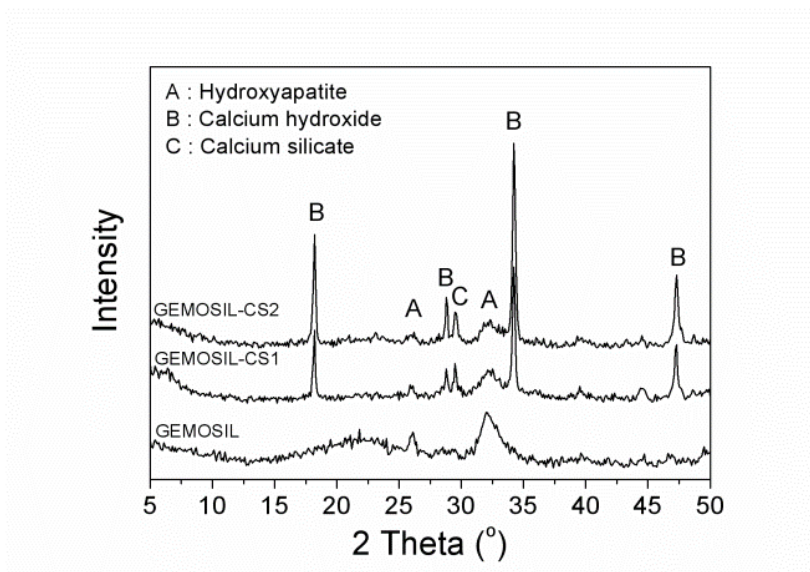


Figure 7.6 XRD measurements of GEMOSIL composites after drying at 37 °C for 48 hours. The peaks indicated the existence different phases including hydroxyapatite, calcium hydroxide and calcium silicate.

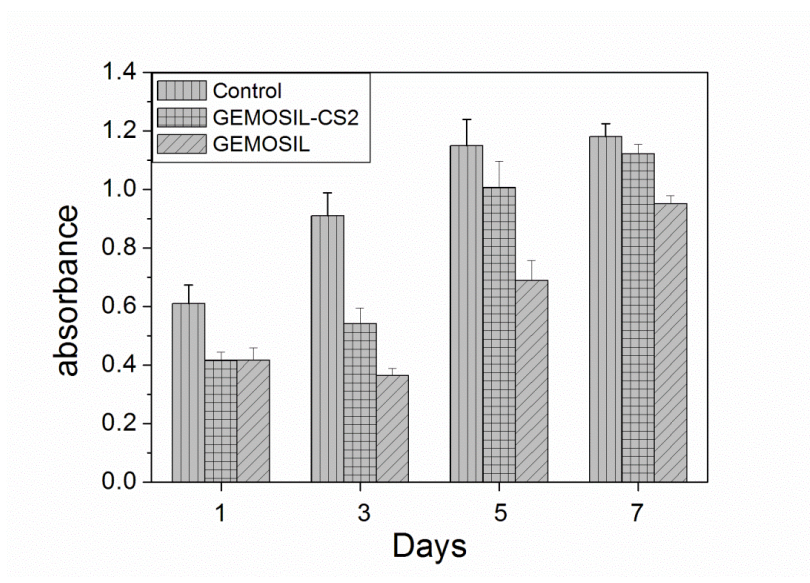


Figure 7.7 Growth characteristics of MC3T3 cells were assessed on both GEMOSIL and GEMOSIL-CS2. Proliferation potential of the cells was assessed by MTS assay on day1, 3, 5, and 7. The cells were cultured with initial number of 5×10^5 cells on all culture dishes (control), culture dishes coated with GEMOSIL, and culture dishes coated with GEMOSIL-CS2.

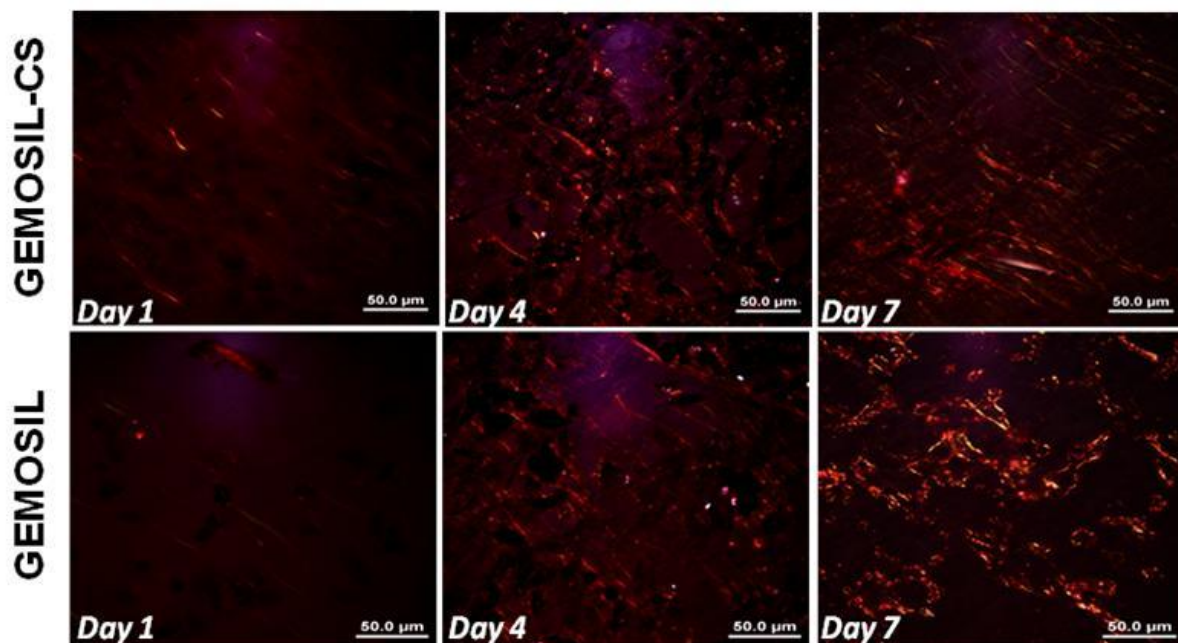


Figure 7.8 Micrographs of Picrosirius stained MC3T3-E1 cells cultured on GEMOSIL and GEMOSIL-CS2 coated glass after 1, 4 and 7 days. With the use of polarized filters, the orange and yellow-reddish fibers represent collagen.

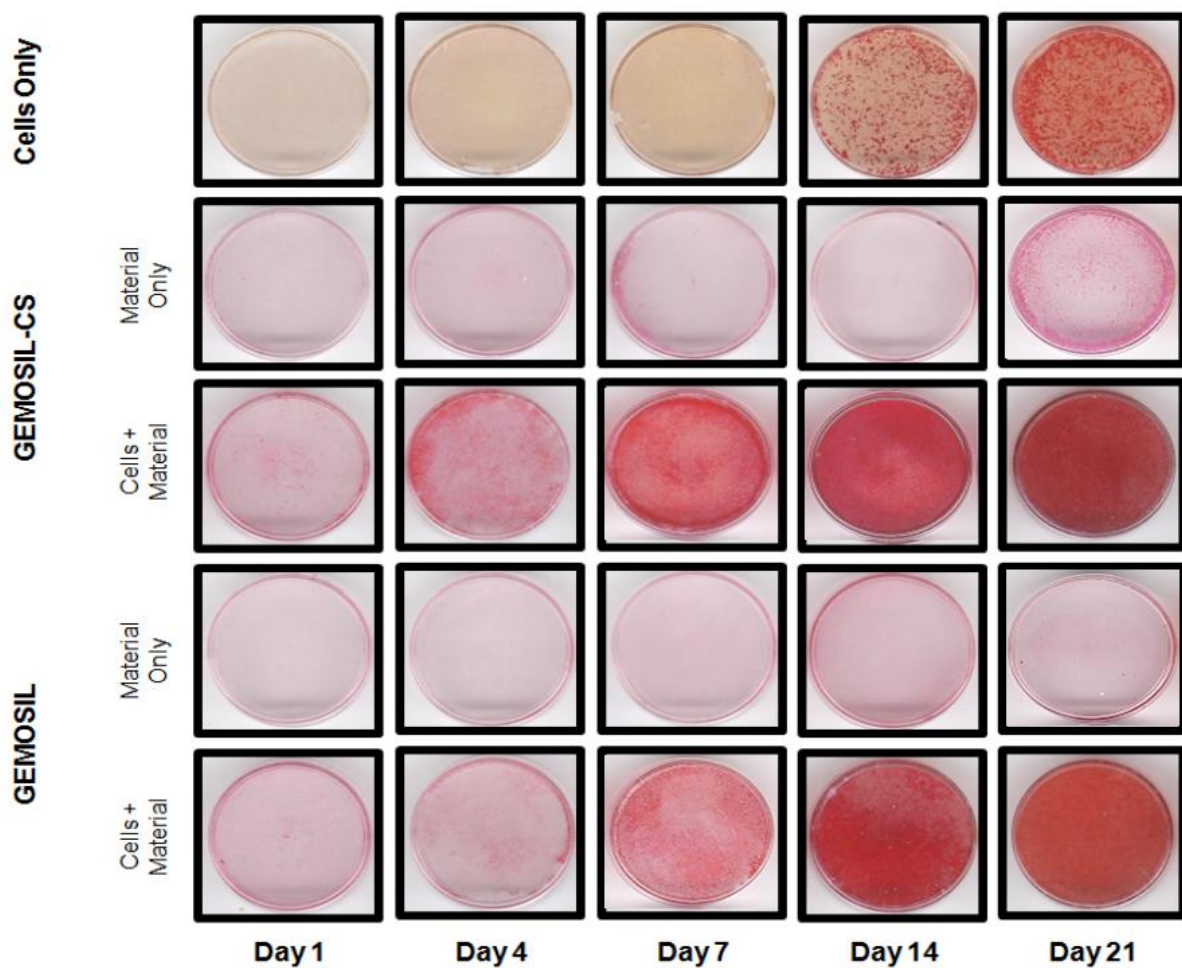


Figure 7.9 Mineralized nodule formation from MC3T3-E1 cells. Calcium deposition from MC3T3 cells cultured on both GEMOSIL and GEMOSIL-CS2 coated dishes were observed by Alizarin Red staining at 1, 4, 7, 14 and 21 days in culture.

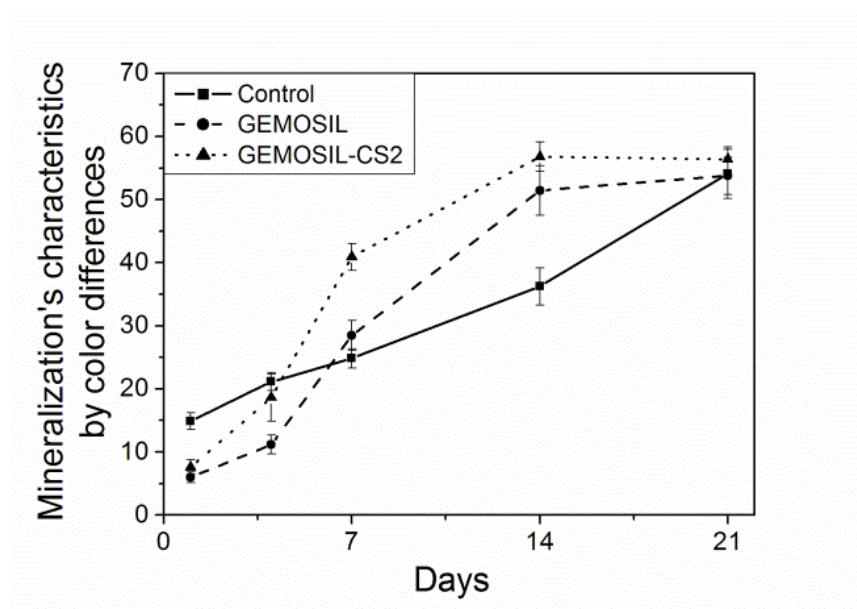


Figure 7.10 Quantification results of mineralization characteristics of control, GEMOSIL and GEMOSIL-CS2 at 1, 4, 7, 14 and 21 days derived from color differences (δ) by CIELAB method.

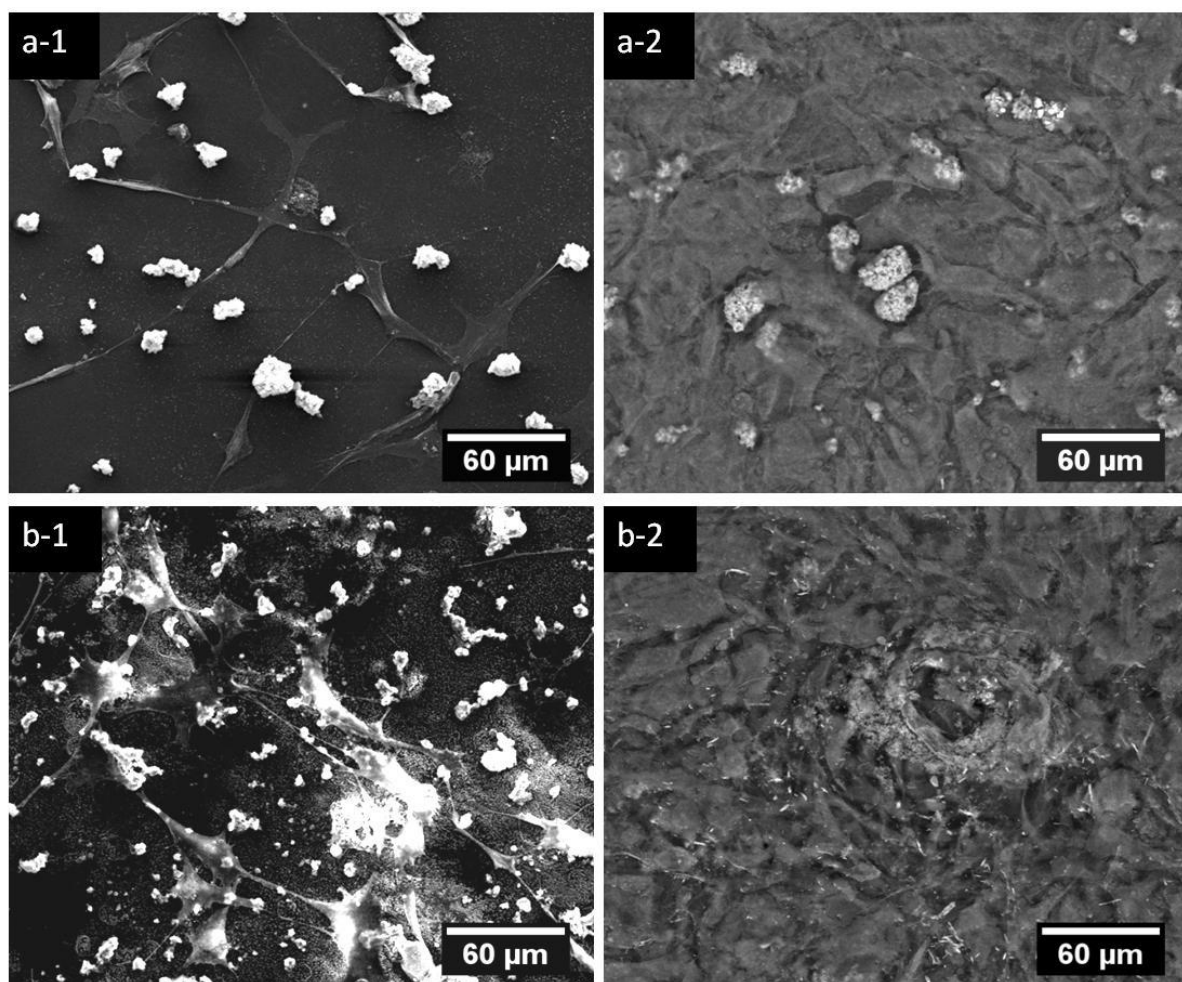


Figure 7.11 SEM micrograph showed the cell proliferation potential on (a) GEMOSIL and (b) GEMOSIL-CS2 after (I) 4 and (II) 7 days in culture. GEMOSIL-CS2 samples showed higher proliferative potential than those on GEMOSIL for both 4 and 7 days.

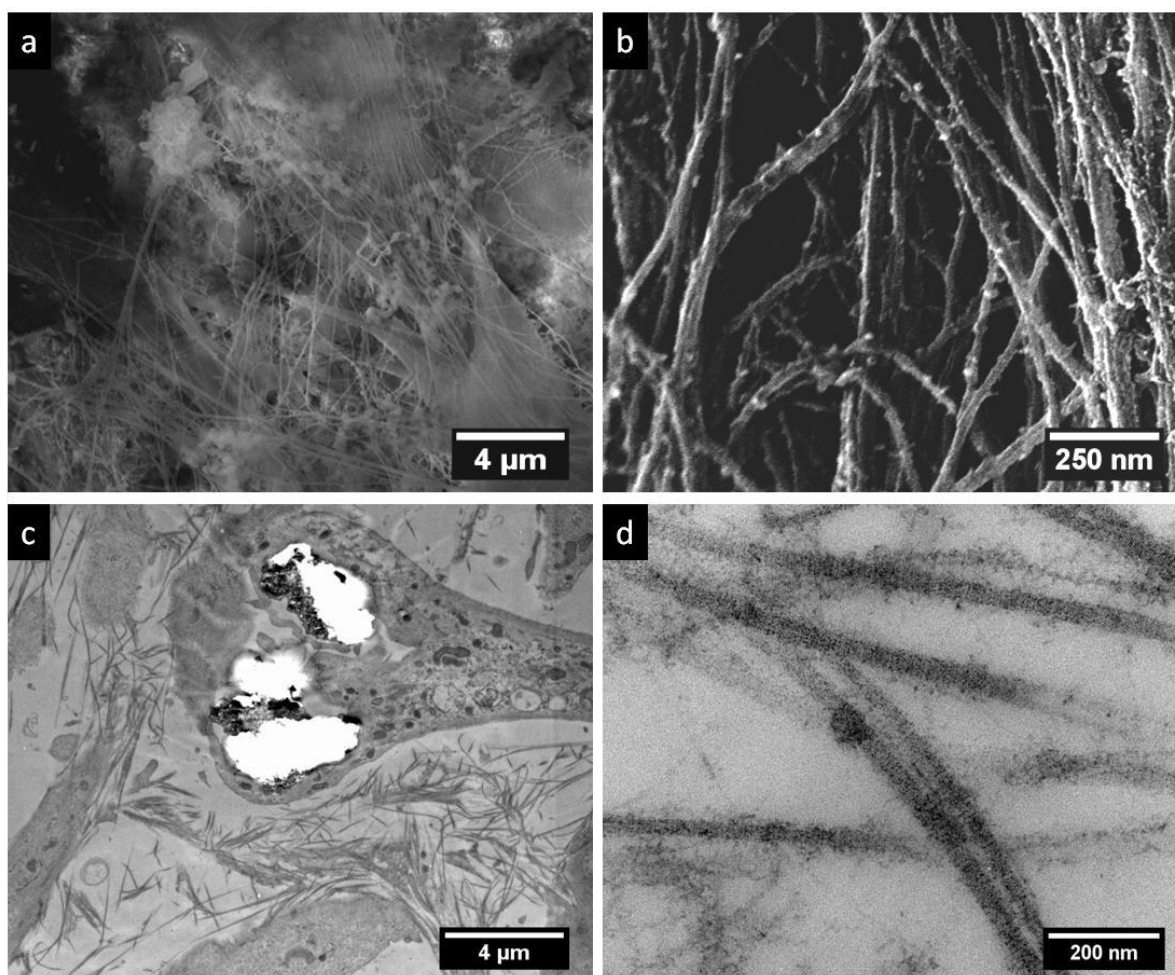


Figure 7.12 SEM and TEM images of GEMOSIL-CS2 samples after 7 days in culture (a) SEM images showed MC3T3-E1 cells have produced extracellular matrix around the cells after 7 days. (b) High magnification SEM images indicated collagen fibrils were partly covered by mineral particles. (c) TEM micrographs showed the formation of collagen fibril around the cells and cells intimately contact with materials. (d) The nodule particles formed on the collagen surfaces also can be observed in TEM images.

Table 7.1 Composition of GEMOSIL, GEMOSIL-CS and HAp-CS nanocomposites

Samples	HAP-Gel (mg)	HAp (mg)	enTMOS (μL)	Ca(OH) ₂ (mg)	CaCl ₂ (1M) (μL)
GEMOSIL	100	0	300	0	48
GEMOSIL-CS1	100	0	300	100	48
GEMOSIL-CS2	100	0	300	200	48
HAp-CS2	0	100	300	200	48

Chapter 8

Conclusions and Future Work

8.1 Conclusions

The present studies examined the properties of versatile polymer-silica nanocomposites and utilized the inherent limitations of sol-gel nanocomposites to produce unique structures that cannot be derived by the conventional methods. Several important steps have been made towards developing polymer-silica nanocomposites as a novel class of efficient nanofabrication systems for multifunctional applications. First, self-assembly of AgCl crystals at the surface of PEG-silica nanocomposite films containing AgCl nanocrystals and PEG as diffusion-controlled media has been successfully demonstrated. The ability of using nanoporous film as an ion source to conduct growth of crystals with controllable orientation, shape, and dimensions may open new ways to pattern and fabricate various nanocrystal systems on solid surfaces. When heat-treating the same nanocomposites, an interconnected silver network with grain boundary-like layers was found spontaneously formed inside the silica matrix. The research determined that the shrinkage-induced stress during the drying process results in microcracks where the crack surfaces serve as a 3-D template for silver to interconnect. In order to increase crack density, the monolith was ground into powders for heat treatment and robust metal foams can be synthesized after etching. Furthermore, by incorporation of thiol groups combining room temperature and high temperature method, patterned silver nanoparticle arrays can be derived. The controlled selectivity and distribution of nanoparticle can be achieved regardless of the existence of residual layer inherent from microcontact imprint. Lastly, Hydroxyapatite-gelatin modified siloxane (GEMOSIL) nanocomposite was developed by coating, kneading and hardening processes to provide

formable scaffold. The interfacial interactions within nanocomposites have been found critical to the biocompatible, osteoconductive, mechanical and degradable properties. The biomimetic nanocomposites have shown high potentials for tissue engineering bone regeneration.

8.2 Future work

For future works, the possibility to extend the same method for synthesizing different metal and alloy foams should be explored. In the same time, the properties of metal foams including surface areas, electrochemistry, catalysis and mechanics should be further analyzed for potential applications such as electrode, catalyst, and mechanical structures. For bone scaffolds, *in vivo* osteogenic properties should be examined for future clinical tissue engineering applications. The pore structures within scaffolds could be incorporated by leaching or prototyping methods for bone in-growth. The incorporation of degradable polymers such as biodegradable polyester or hydrogels could be investigated to manipulate the degradation rate of scaffolds to match the bone healing process.